2022

Hot-carrier dynamics and transport mechanisms in InAs/AlAsSb multiple quantum wells

Herath Pathiranage Janaka Chathuranga Piyathilaka
hjpiyathilaka@mix.wvu.edu

Recommended Citation

Piyathilaka, Herath Pathiranage Janaka Chathuranga, "Hot-carrier dynamics and transport mechanisms in InAs/AlAsSb multiple quantum wells" (2022). *Graduate Theses, Dissertations, and Problem Reports*. 11279.
https://researchrepository.wvu.edu/etd/11279

Hot-carrier dynamics and transport mechanisms in InAs/AlAsSb multiple quantum wells

Herath Pathiranage Janaka Chathuranga Piyathilaka

Dissertation submitted to the
Eberly Collage of Arts and Sciences
at West Virginia University
in partial fulfillment of requirements
for the degree of

Doctor of Philosophy
in
Physics

Alan D. Bristow, Ph.D., Chair
Cheng Cen, Ph.D.
Tudor Stanescu, Ph.D.
Ian R. Sellers, Ph.D.

Department of Physics and Astronomy

Morgantown, West Virginia
2022

Keywords: Ultrafast Spectroscopy, Hot-carriers, Multiple quantum wells, Hot-carrier Solar cells, Terahertz Time-Domain Spectroscopy, AC conductivity, Electronic Transport, Terahertz Time-Resolved Spectroscopy, Metastability, AC photoconductivity

Abstract

Hot-carrier dynamics and transport mechanisms in InAs/AlAsSb multiple quantum wells

Herath Pathiranage Janaka Chathuranga Piyathilaka

Semiconductor photovoltaics convert light into electricity through the extraction of photo-excited charge carriers. Among the most important parameters for a photovoltaic cell are good optical absorption in the desired region of the electromagnetic spectrum, and sufficient excited-state lifetimes and mobilities of the photocarriers to allow for charge separation and extraction before recombination. For solar cell applications there are significant challenges to overcome to improve the efficiency of the light-to-electricity conversion. The cells are most commonly made of silicon, which has a nearly perfect bandgap for absorbing the most solar radiation, an indirect bandgap to give a long photocarrier lifetime and good carrier mobility to allow for extraction of carriers. However, these single p-n junctions suffer from a thermodynamic limit of about 33% (without solar concentration), due to the detailed-balance of photocarriers excited above the bandgap, giving their energy to heating the device. Alternative methods include expensive multijunction devices with several layers absorbing and providing photovoltage at different energies, inefficient nanoparticle configurations and unproven hot-carrier solar cells (HCSCs). The latter were proposed to take advantage of good quality semiconductor materials and find mechanisms to prolong the photocarrier lifetime and allow them to be extracted via energy-selective contacts before recombination can occur. The detailed balance estimate that some HCSC devices may reach a theoretical maximum of 85%.

In this dissertation, InAs/AlAsSb type-II aligned multiple quantum well (MQW) heterostructures are explored for their potential as HCSCs. III-V semiconductor devices are grown by molecular beam epitaxy and are of high quality, possess a band alignment that generally separates electrons and holes leading to a prolonged photocarrier lifetime and also exhibit low thermal conductivity that can play additional roles in preventing carriers from cooling and thus further prolonging the carrier lifetime. These systems are of great interest because of these known properties, but it is unclear whether or not they are viable for HCSC, because mechanisms for hot-carrier lifetimes are poorly understood and photocarrier transport had not been explored when the results for the this project was started. Specifically, this work uses terahertz time-domain spectroscopy, time-resolved terahertz spectroscopy and transient absorption to addresses the observation of ground-state AC conductivity, excited-state AC photoconductivity and the charge carrier dynamics.

Findings show that lattice temperature significantly influences this MQW's ground-state carrier transport due to alloy-intermixing at the well interfaces and weak coupling between long-range optical and acoustic phonons. It is also shown that excited photocarrier undergo dynamics that are also dependent on lattice temperature, dominated almost entirely by the availability of defect states in the wells and by localization/delocalization of hole bands with increasing temperature. Further investigation showed that high photocarrier concentration and low lattice temperature revealed a metastable state at early times after photoexcitation due to an intra-subband relaxation bottleneck mediated by reabsorption of optical phonons

by the carrier and fast Auger scattering of carriers deeper into their respective bands. Hot-carriers also have long lifetimes outside of this regime, which can be exploited for photovoltaic applications because they generally have high carrier mobilities due to the high quality growth. Moreover, the confinement leads to ambipolar diffusion that can withstand a higher number of scattering events at ambient temperatures where such devices might operate.

Acknowledgements

I express my deepest gratitude to my thesis advisor, Dr. Alan D. Bristow, without whom this would not have been possible. His guidance, support, and motivation throughout my graduate studies enabled me to complete this work successfully. Dr. Bristow, I thank you for being my mentor and my teacher.

I would also like to thank my dissertation committee members, Dr. Cheng Cen, Dr. Ian Sellers, and Dr. Tudor Stanescu, for their extraordinary feedback on this manuscript. I am grateful to our research collaborator, Dr Ian Sellers and his research group at Oklahoma university for their contribution through out this project.

A special thanks to Dr. Matthew Johnson for always finding the time out of your extremely busy schedule to give me career advice and words of wisdom. In addition, thank you to the rest of my research group at WVU: Dr. Derek Bas, Dr. Rishmali Sooriyagoda, and fellow office mates and friends, Sunil Gyawali and Jack Powers. Special thanks to my all-time mentor and friend, Dr. Oshadha Ranasinghe, who has been my greatest guidance since the beginning of my graduate studies. Furthermore, I deeply appreciate the support I received from my dear friends, Uthpala and Hasith, for thier comments.

I sincerely thank my wife, Dona Sachini Hewagallage, for being with me and giving me emotional support throughout my graduate life.

Lastly, I my dearest thanks to my parents, Sisira and Chandra Piyathilaka. There are no amount of words that I could write to tell you how much I appreciate everything you have done for me—especially my mother, for all the sacrifices you made to bring me up since my father perished. Without your dedication, guidance, and encouragement, none of this would have been possible. Thank you for everything you have done to model me into the goal-driven, and ambitious man I am today. I will forever be grateful for the infinite amount of love and support you have given to me.

Dedication

To to my family. For their unlimited love.

Table of Contents

Chapter

List of Tables

List of Figures

Figure Page

Figure Page

Chapter 1:
Introduction

1.1 Motivation: Energy harvesting

At the time of writing, only 11% of world energy generation comes from renewable energy sources, out of which 2% comes from solar energy, which is about 700 GW [1].

The sun emits energy in the form of electromagnetic radiation, with $\approx 6.4 \times 10^7$ W/m^2 intensity and ~ 980 W/m^2 reaching the Earth's surface (considering no absorption). Being a renewable and sustainable energy source, harvesting solar energy has gained considerable attention in the scientific community and in the commercial sector. There are two main methods in harvesting solar energy: (i) concentrated solar power and (ii) photovoltaic (PV) solar cells. In the 1^{st} method, electricity is generated by concentrating sunlight onto a receiver, using a series of mirrors and lenses. Then, the light is converted into heat at the receiver to drive a steam turbine that converts heat into electricity. Therefore, this method is primarily used in commercial-scale power plants, and it is more expensive than PV power generation.

By contrast PV solar cells harvest sunlight and convert it to electricity directly through the absorption of light and seperation of charges. At the begining in 1970's, the cost of a solar panel was about \$76 per watt. In addition to increased efficiency, today the cost has dropped down to \$3 per watt [Figure 1.1]. At the time of writing, solar energy is cheaper than other renewable energy technologies [2, 3] and electricity generation by fossil fuels [4–6].

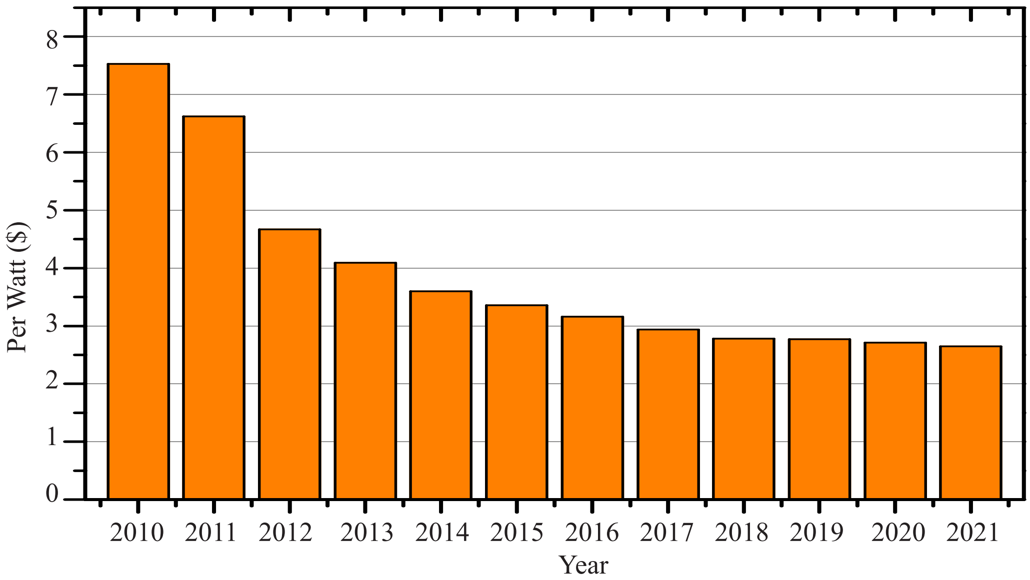

Figure 1.1: Residental PV system cost. Figure adapted from NREL [2].

1.2 Solar cells

The foundation of solar cells are based on the PV effect discovered by Alexandre-Edmund Becquerel in 1839 [7]. In 1870 PV effect was first studied in selenium, which led to the development of the photoconductive cell initially with a conversion efficiency fell below 2% [8]. The journey of commercial solar cells started in the 1950s when Bell Laboratories introduced the practical PV solar cell [7]. With the introduction of solar cells as a power source for the Vanguard 1 satellite in 1958, the solar cell industry was truly born.

Inside a solar cell, a semiconductor material absorbs the incident light exciting electrons across the bandgap and creating electron-hole pairs [inset of Figure 1.2]. These electron-hole pairs must be spatially separated in the PV to generate electricity because direct gap semiconductors have fast recommbination. As shown in Figure 1.2, solar radiation consists of photons with different energies. Therefore, PV solar cells can be developed, to take advantage of those photons.

The efficiency of the energy conversion by the solar cells depends on the absorption of

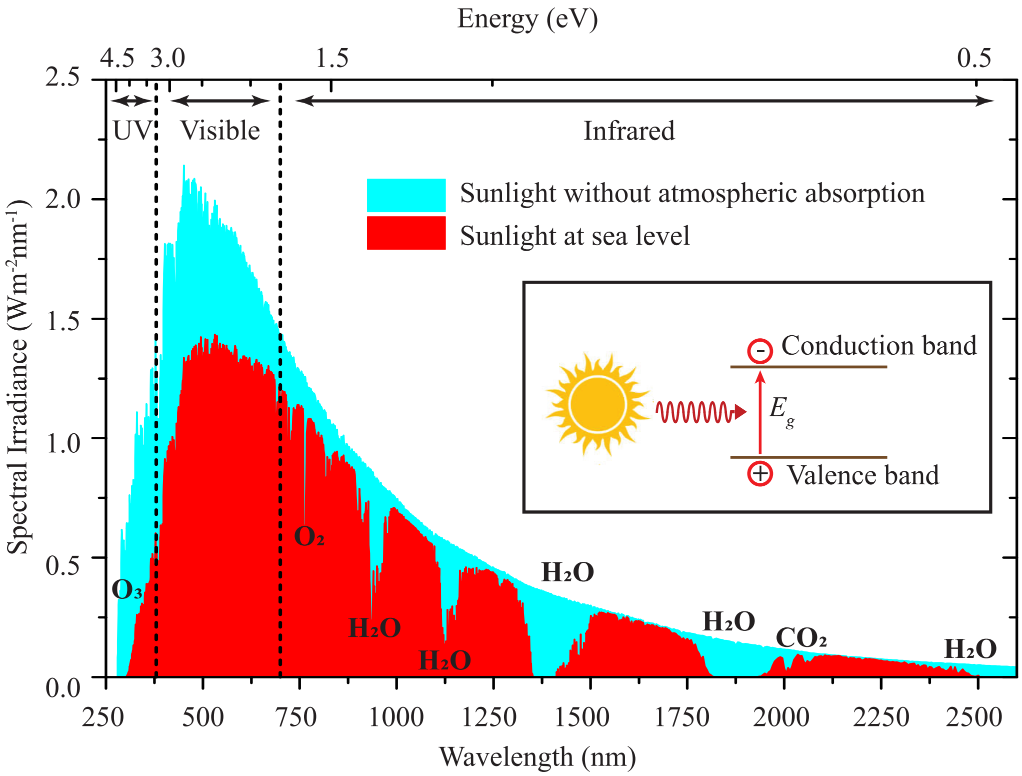

Figure 1.2: Spectrum of solar radiation. Figure adapted from NREL [9]. Inset shows the electron-hole pair creation upon the incident light exceeding the band gap of the semiconductor.

light in the semiconductor material, the lifetime of the excited carriers before they recombine, and the mobility of the photoexcited carriers [10]. Due to these constraints, most solar cells are based on p-n junctions between doped regions of indirect semiconductors. This configuration improves the light absorption due to two band gaps in the system. It enhances the charge separation caused by the built-in potential gradient from the depletion region of the p-n junction. Even with this modification, the maximum efficiency achieved by the single-junction solar cells is limited to ∼ 33%. This limitation is best known as the detailed-balanced limit [11], which is theorized by Shockley and Queisser. These calculations are based on considering the thermodynamics limits, semiconductor's bandgap, and assuming

100% light absorption. Power conversion efficiency can be increased by making thicker and defect-free semiconductors. The alternate method is to use thin-film nanostructures coupled with charge extraction layers [12]. Nevertheless, the maximum power conversion efficiency achieved by single-junction solar cells is still $\sim 33\%$ under 1-sun illumination [13].

1.3 Overcome the fundamental losses in solar cells

The biggest barriers to achieving higher efficiencies are several fundamental loss mechanisms occurring in these systems. Figure 1.3 shows the fundamental losses arising in single-junction solar cells, limiting their power conversion efficiency.

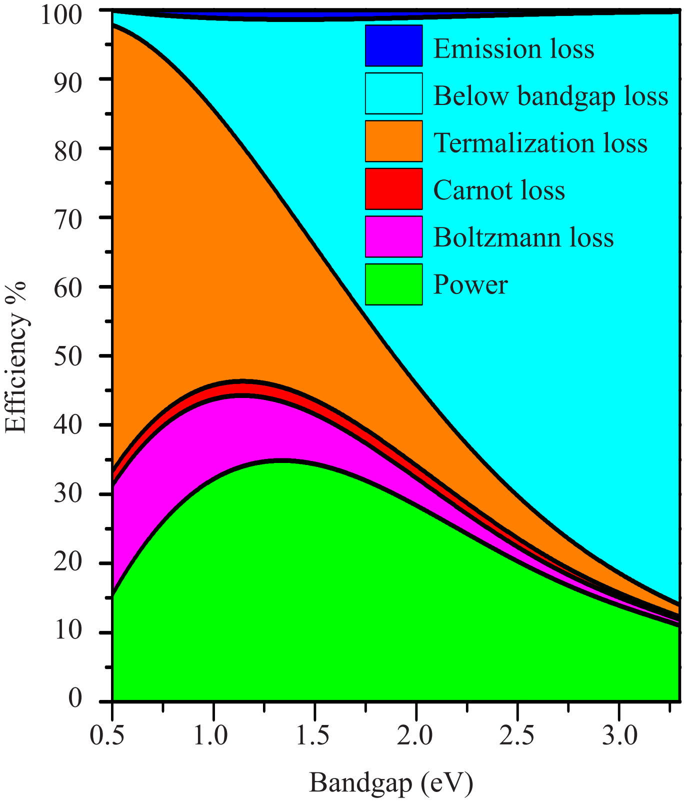

Figure 1.3: Fundamental loss mechanisms in single junction solar cells. Figure modified from Hirst *et al.* [14].

One loss mechanism is below bandgap loss [15], also known as transmission loss. The leading cause for this effect is the lack of absorption of photons that have energy below the bandgap of the semiconductor material. Thermalization loss is the next loss that occurs when the semiconductor material absorbs high-energy photons. These high-energy photons exceed the bandgap energy of the material and results in "hot carriers", that have to cool via emission of lattice phonons. Semiconductor materials have fast carrier thermalization and cooling rates; thus, hot carriers quickly cool to the band edge after absorption [15, 16].

Emission loss [15] is another loss mechanism due to the radiative recombination process on the electron-hole pair. Radiative recombination causes the energy to release as a photon, corresponding to the material's bandgap. Therefore, this limits the efficiency of the solar cells. This can be overcome by using indirect bandgap materials.

Other power loss mechanisms, shown in Figure 1.3 are Carnot and Boltzmann loss mechanisms [15, 16]. Carnot loss is the energy needed to convert thermal radiation into electric work. Solar cells being considered as heat engines, looses energy into the cold reservoir during the conversion of thermal energy (hot reservoir, the Sun) into electric work. This appears as a voltage drop in the solar cells. Boltzmann loss is the energy loss due to the mismatch between absorption and emission angles in entropy generation by the expansion of phonon modes.

The efficiency of solar cells can be improved using materials that have lower bandgaps. However, this increases the thermalization and cooling losses. Wide bandgap semiconductors minimize the thermalization and cooling loss with the reduction of conversion efficiency by increasing below bandgap loss. Therefore, balancing these energy losses, the maximum conversion efficiency that a single-junction solar cell can achieve is $\sim$33% [11] for a $E_g \approx 1.1$ eV, exactly that of Si. At the time of writing, 80% of the solar cell market is based on first-generation PV solar cells (crystalline solar cells), even though they have low power

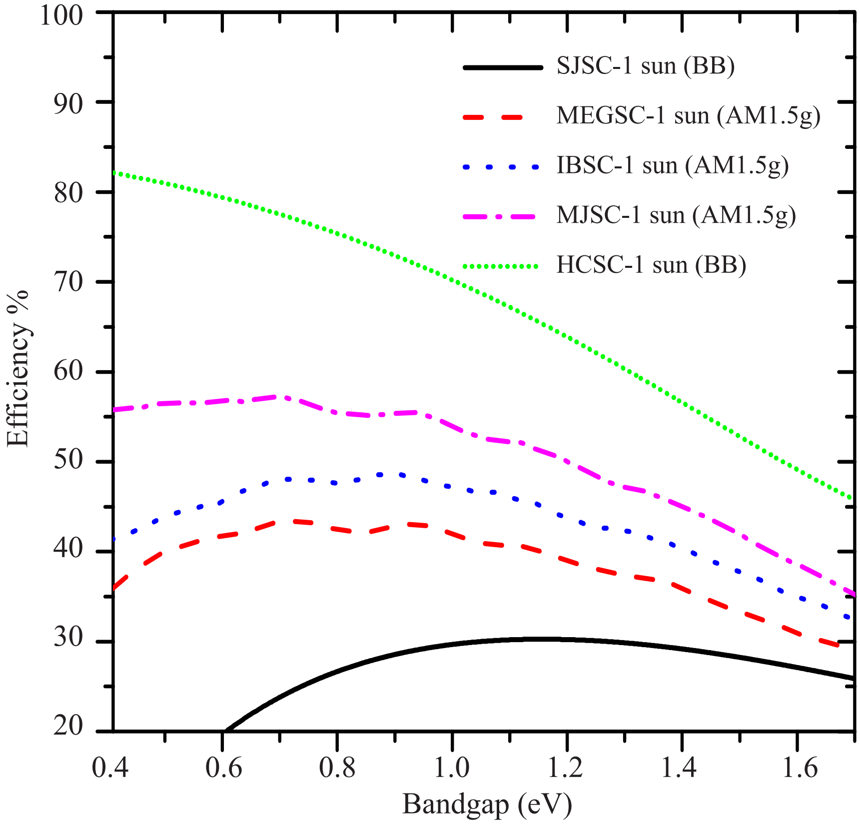

Figure 1.4: Theoretically available power conversion efficiency for several solar cell concepts.[SJSC: single junction solar cell; IBSC: intermediate band solar cell; MEGSC: multiple excitone generation solar cell; MJSC: multijunction solar cell (six junctions); HCSC: hot-carrier solar cell; BB: Blackbody; AM1.5g: 1.5 atmospher thickness correspond to solar zenith angle of $z = 48.2°$]. Figure modified from Micha *et al.* [17].

conversion efficiency.

To improve the efficiency, solar cells are being developed using thin film heterostructures to control the absorption and charge carrier dynamics [18–21] in so-called second generation photo-voltaics. Apart from the increased solar absorption through light-trapping [22, 23], this approach reduces the cost of solar cells compared to crystalline solar cells due to reduced material cost. Yet, this technique fails to exceed the detailed-balance limit. Third generation of solar cell technology proposes solutions to this problem: (i) multi-junction solar cell

(MJSC) [24, 25], (ii) intermediate band solar cell (IBSC) [26], (iii) up/down-conversion solar cell systems [27–29], (iv) multi-exciton generation solar cells (MEGSC) [30], and (v) hot-carrier solar cells [31, 32]. The first three concepts focus on increasing efficiency by adding several solar cell layers together to the absorption of the solar spectrum.

MJSCs, consist of multiple single-junction solar cells stacked on each other. The top has the largest bandgap, and the bottom has the smallest bandgap, minimizing the transmission loss. In this configuration, absorption of the solar spectrum is decomposed into multiple ranges (UV to IR range) [24]. The MJSCs, layers are connected in series, to increase the photocurrent and achieve higher performance. By doing so, these systems achieve a maximum power conversion of 45% [25] [Figure 1.4].

IBSCs is a concept of sandwiching materials between semiconductors [26] such that, the intermediate band material absorb photons with the sub-bandgap energy. This occurs via electron transition from the valence band to the intermediate band and from the intermediate band to the conduction band. So photons with less energy than the semiconductor's bandgap ($hv < E_g$) use the intermediate band as a "stepping stone" to excite the carriers.

In up/down conversion solar cells, the up-conversion, and the down-conversion optical processes are utilized to improve the solar spectrum absorption. The reduction of efficiency due to below bandgap loss is minimized through converting sub-bandgap photons into higher energy photons, that exceeds the bandgap of the solar cell's absorber material [33, 34]. The down-conversion solar cells convert hot carriers into lower-energy photons, which have the energy of the bandgap of the absorber. This technique minimizes the thermalization and cooling loss of hot carriers in solar cell applications [27, 35]. Upconversion material can be placed between the absorber layer of the PV cell and down-conversion material placed on top of the solar cell absorber.

The last two techniques focus on reducing thermalization and cooling loss in order to increase the efficiency. In MEG-SCs, multiple electron-hole pairs are generated after, impact ionization absorbing a single high-energy photon. This process increases the photocurrent and solarcell efficiency. Comparatively HCSCs are predicted to have the highest power generation efficiency [31] [Figure 1.4].

1.4 Hot-carrier solar cells

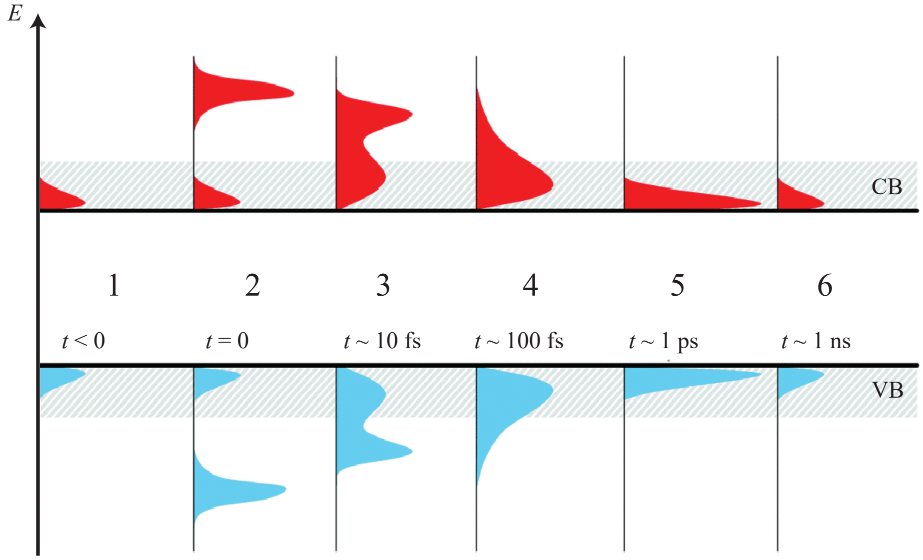

Figure 1.5: Schematic of the time evolution of photoexcited carrier distribution in a semiconductor. Figure modified from Kahmann *et al.* [36].

Hot carriers are created when photocarriers are created much above the semiconductor's bandgap. Figure 1.5 shows the process of carrier dynamics, photoexcitation [(1) → (2)], thermalization [(2) → (3)], cooling [(3) → (4) → (5)], and recombination [(5) → (6)]. Thermalization occurs when carriers redistribute their excess energy via carrier-carrier and optical phonon scattering to produce hot Fermi-Dirac distribution with a quasi-equilibrium carrier temperature exceeding the lattice temperature. Afterward, hot carriers lose their excess kinetic energy by phonon emission and cool intraband to the lattice temperature within picoseconds [(4) → (5)]. Finally, carriers recombine to achieve equilibrium.

The concept of HCSC is to generate higher efficiency by capturing the photogenerated hot carriers before the cooling. Theoretically, it predicts achieving a maximum conversion efficiency of 85% [31] under the maximum concentration [Figure 1.4]. To achieve this performance , one must minimize the thermalization loss and extract hot carriers through energy-selective contacts (ESC).

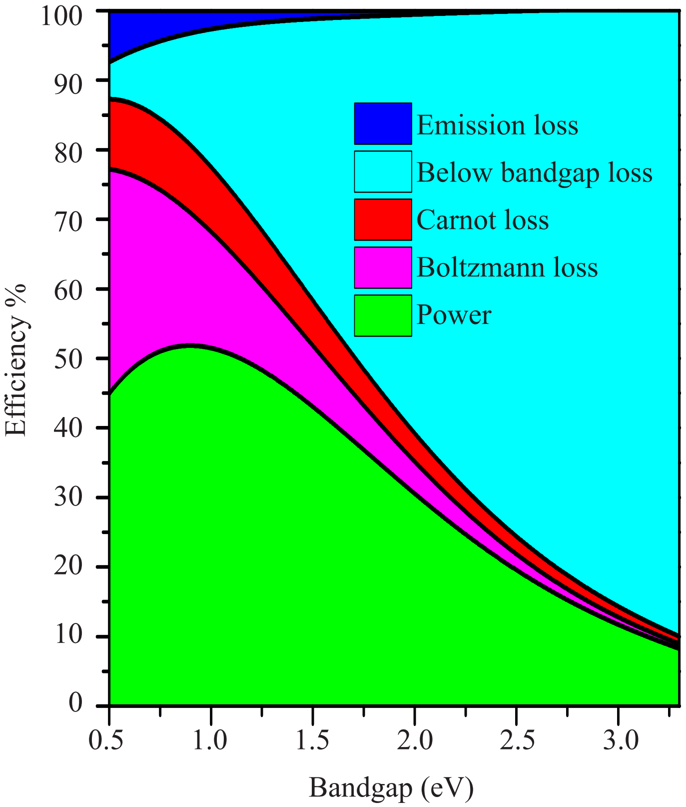

Figure 1.6: Fundamental loss mechanisms in hot carrier solar cells. Figure modified from Hirst *et al.* [14].

Most of the prototype HCSC absorbers are based on III-V semiconductor heterostructures [32, 37–43], which exhibits phonon bottleneck in the system. This phenomenon occurs due to a miss-match between the generation rate of optical phonons and the conversion rate of optical to acoustic phonons [40, 44–47]. Consequently, photoexcited carriers will reabsorb these excess optical phonons and remain "hot" in the system (detailed discussion in Chapter 4). Therefore, cooling can be slowed by using the phonon bottleneck effect [48]. This condition is achieved by increasing the photocarrier density. A steady-state hot carrier distribution can be created when the photoexcitation rate is lower than the scattering rate and higher than the cooling rate. This phononic engineering can reduce the emission of optical phonons by hot carriers [49, 50]. Figure 1.6 shows the calculated power conversion efficiency of HCSC. Cooling loss is eliminated in these calculations [51], leading to the HCSC efficiency exceeding 50% under 1-sun illumination.

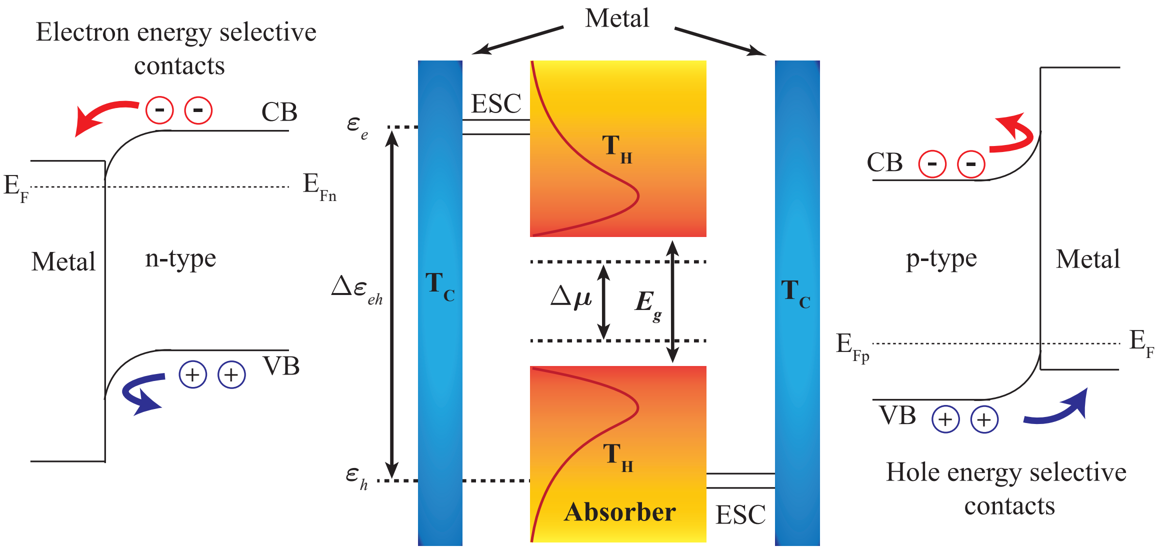

Figure 1.7: Schematic diagram of hot-carrier solar cell with energy-selective contacts (ESC).

Hot carrier extraction has been proposed through energy-selective contacts (ESC). This technique extracts only one type of carrier (electron or hole) through low resistive contacts while maintaining a large barrier for other types. Proposed ESCs are based on multilayer heterostructures with a narrow band of energies [52]. Figure 1.7 shows the conceptual architecture of the HCSC [37, 53, 54]. Narrow energy selectivity maintains minimum entropy exchange while increasing electrical conductivity for optimal carrier extraction, allowing hot carriers (electrons and holes) to be extracted isentropically to metal contacts with minimum loss of excess kinetic energy via cooling.

Hot carriers can maintain a higher temperature (T_H) than the lattice temperature (T_C) for some time. Consequently, the narrow band heterostructure reduces the entropy exchange between hot carriers and the cold reservoir. Heterostructures based on quantum wells and quantum dots are suitable candidates for the ESCs [55, 56].

ESCs have wider band gaps than the semiconductor material and the output voltage (V) of the system can be determined by

$$qV = \left(1 - \frac{T_C}{T_H}\right) \Delta\varepsilon_{eh} + \Delta\mu \frac{T_C}{T_H}, \tag{1.1}$$

where $\Delta\mu$ is the quasi-Fermi level splitting, and q is the charge of the carriers [57].

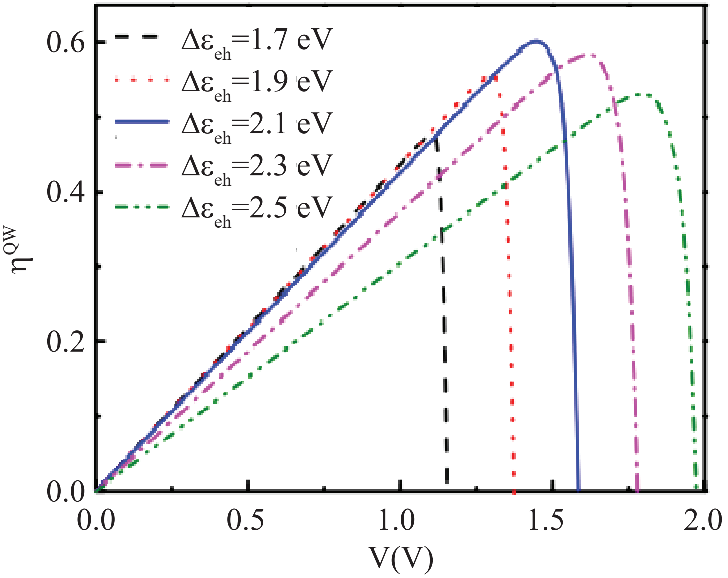

Figure 1.8: Efficiency-voltage characteristic of QW ESC for different $\Delta\epsilon_{eh}$ values. Figure modified from Su *et al.* [58].

Figure 1.8 shows the theoretical calculated efficiency of HCSC for different carrier extraction energies for QW ESCs [58] for the absorber with 0.9 eV bandgap. This is achieved by minimizing energy dispersion from thermalization in the electrodes.

Conibeer *et al.* [59] and Hirst *et al.* [60] explore HCSCs based on quantum well. Nevertheless, bottleneck inhibits carrier cooling and these structures contributes to long lifetimes in hot carriers.

Experimental evidence of HCSC operation is examined by Rodiére *et al.* [41] in InGaAsP MQWs. They used photoluminescence spectroscopy to investigate the carrier temperatures and quasi-Fermi level splitting. Investigations were carried out as a function of excitation power and revealed that hot carriers exhibits high temperatures. These findings show experimental evidence demonstrating, that the detailed-balance limits can be overcome by using multiple quantum well structures as the absorber in HCSCs.

1.5 Outline of the Dissertation

In this dissertation, a comprehensive investigation is carried out on InAs/AlAsSb type-II multiple quantum well structures as a prototype material for the absorber in HCSC applications. The goal is to identify hot-carrier dynamics and transport mechanisms that may contribute to enhancing solar energy conversion in future device architechture. As the stepping stone for this investigation, Chapter 2 provides information on the spectroscopic techniques used in this study and details of the multiple quantum well structure.

Chapter 3 presents the ground-state transport mechanisms in the multiple quantum well structure, investigated by THz time-domain spectroscopy.

Chapters 4 and 5 discuss the details of hot-carrier lifetimes and the relaxation recommbination mechanisms using time-resolved THz evolved with different excitation and sample conditions.

Chapter 6 explores hot-carriers transport using time-resolved THz spectrum in the presence of an optical pump probe. Hence, investigation show the dynamical changes of the carrier transport for various excitations and sample conditions.

The final chapter summarizes the findings and hypotheses and gives an insight into the future development of HCSCs based on type-II MQWs.

Chapter 2:

Experimental techniques and sample details

2.1 Introduction to Terahertz radiation

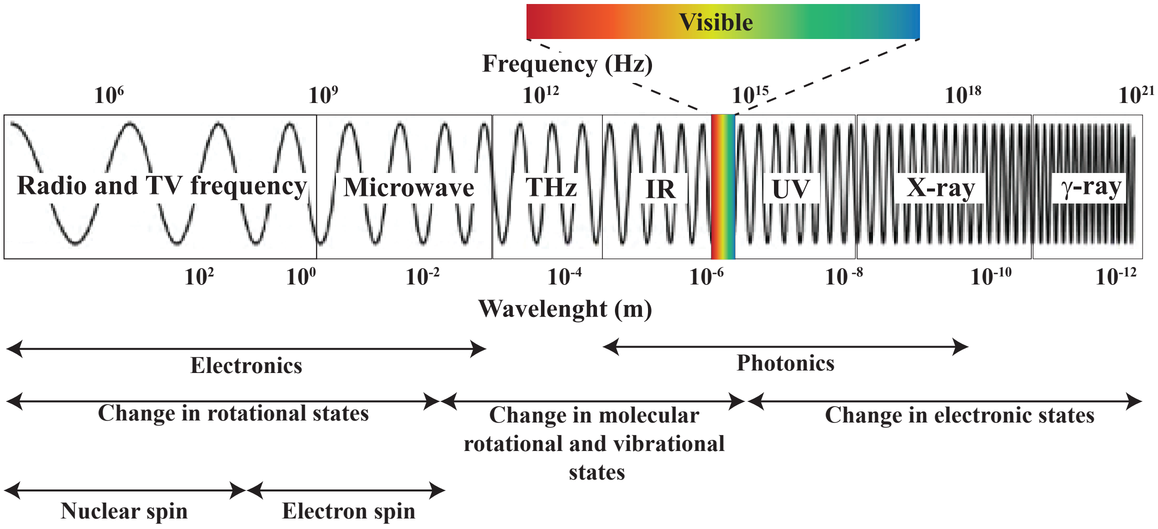

Figure 2.1: The spectrum of electromagnetic radiation with various interactions with matter.

Terahertz frequencies falls between microwaves and infrared frequencies on the electromagnetic spectram. The frequency/ wavelength/ energy range of the THz gap is 0.1 - 10 THz/ 0.03 – 3 mm/ 0.4 – 40 meV. In this range are lattice vibration in solids, the rotational transition of molecules, intra-band transitions in semiconductors, superconductivity gaps, and magnetic properties such as magnetic spins, ferromagnetic and antiferromagnetic modes etc [61–67]. THz is also used in medical fields for imaging [68], wireless communications [69], and quality control processes [70]. THz radiation is an alternative to x-rays because it is non-ionization and organic materials are somewhat transparent.

Due to the low photon energy, THz is a powerful spectroscopy tool for materials characterization, because it interacts with electrons, holes, phonons, excitons, and other quasiparticles [see Figure 2.1]. Consequently, there has been a rapid development in generating high THz electric fields [71–75] and broadband detection [76–79] techniques for the spectroscopic applications. For an example, THz time-domain spectroscopy (THz-TDS) is a highly used spectroscopic technique to determine electronic properties such as mobility, carrier density, and scattering time etc [80, 81]. Also, using time-resolved THz spectroscopy [82–85], one can determine carrier dynamics and photo-conductivity of materials.

In 1990, the available frequency spectrum that could be generated and detected in the time domain was limited to a few THz [86]. Advancements in broadband ultrafast lasers and exploration of new nonlinear optical materials have pushed this limit into mid-infrared (Wu and Zhang, 1997 [79], Huber *et al.* 2001 [87]) and recently into the near-infrared range, reaching frequencies beyond bandwidth from $\approx 30 - 100$ THz ($\lambda = 3 - 10$ μm).

One particular advantage of all-optical generation and detection of THz pulses is the possibility of combining the approach with a time-synchronized femtosecond excitation pulse. This makes the method well suited for the investigation of electronic charge transport under non-equilibrium conditions [e.g., Averitt and Taylor (2002) [88], Beard *et al.* (2002b) [89], and Schmuttenmaer (2004) [90]]. This attribute permits THz spectroscopy to evade many of the constraints of conventional transport measurement techniques such as Hall-effect measurements.

2.2 THz generation and detection

Much progress has been made in the past two decades in understanding the physics of elementary electronic excitation, owing to the development of sources and detectors of coherent THz radiation. Pulsed, time-domain THz spectroscopy is not only capable of characterizing charge carriers under steady-state conditions, but it is also ideally suited for non-equilibrium measurements using time-resolved THz spectroscopy. An optical pulse can be used to create charge carriers, and the subsequent evolution of charge carriers can be monitored on the femtosecond time scale. Due to this, one has direct access to the time scale information and mechanisms of carrier cooling, trapping, and recombination and the dynamics of the formation of quasi-particles such as excitons and polarons [91, 92].

2.2.1 Electromagnetic wave propagation

The propagation of the electromagnetic wave is essential to understand the interactions of THz radiation with matter. These interactions are discussed using the macroscopic Maxwell model.

$$\nabla \cdot \vec{D} = \rho_f, \tag{2.1}$$

$$\nabla \cdot \vec{B} = 0, \tag{2.2}$$

$$\nabla \times \vec{E} = -\tfrac{\partial \vec{B}}{\partial t}, \tag{2.3}$$

$$\nabla \times \vec{H} = \vec{J}_f + \tfrac{\partial \vec{D}}{\partial t}. \tag{2.4}$$

Here ρ_f and $\vec{J}_f$ represent the free charge and current densities, $\vec{E}$ and $\vec{B}$ represent the electric field and the magnetic field. The electric displacement field $\vec{D}$ and the Auxiliary field $\vec{H}$ are related to the $\vec{E}$ and $\vec{B}$ as

$$\vec{D} \equiv \epsilon_0 \vec{E} + \vec{P} = \epsilon \vec{E}, \tag{2.5}$$

$$\vec{H} \equiv \tfrac{1}{\mu_0}\vec{B} - \vec{M} = \tfrac{1}{\mu}\vec{B}, \tag{2.6}$$

where ϵ_0, ϵ, μ_0, μ represents vacuum and material permittivity, and vacuum and matter permeability respectively. The polarization $\vec{P}$ and the magnetization $\vec{M}$ provide are the macroscopic electromagnetic response of the material.

A homogeneous wave equation can be derived by taking the curl of equation 2.3 and using the linear relationship of equation 2.5 and 2.6. The main approximation used is that $\vec{J}_f$ follows Ohme's law ($\vec{J}_f = \sigma \vec{E}$), where σ is electric conductivity. Therefore, in the absence of ρ_f, the wave equation can be represented as

$$\left(\nabla^2 - \frac{1}{c^2}\frac{\partial^2}{\partial t^2}\right)\vec{E} = \mu_0\left(\frac{\partial \vec{J}}{\partial t} - \frac{\partial^2 \vec{P}}{\partial t^2}\right), \tag{2.7}$$

where c is the vaccume speed of light ($c = 1/\sqrt{\epsilon_0\mu_0}$). From this equation, it is evident that electromagnetic radiation can be generated from a dynamic charge current ($\dot{\vec{J}}$) as well as a dynamic material polarization ($\ddot{\vec{P}}$). $\dot{\vec{J}}$ implies that THz radiation can be generated from accelerating charges which can occur in photo-conductivity switches [93] or air-plasma [94] technique. $\ddot{\vec{P}}$ describes the THz generation change of bound charges, which can occur in nonlinear optical processes such as different frequency generation and optical rectification (OR) [94, 95]. Since THz generation in this thesis arises from OR, terms containing $\vec{J}$ are neglected.

For dielectric materials, the wave equation can be further simplified as

$$v^2\nabla^2\vec{E} = \frac{\partial^2\vec{E}}{\partial t^2}. \tag{2.8}$$

Propagation of electromagnetic wave in homogeneous media with speed at $v = c/n$ represents by the above equation. Here $n = \sqrt{\epsilon/\epsilon_0}$ represents the refractive index of the medium. Therefore, the general solution for equation 2.8 is a linear polarized monochromatic plane wave in z direction

$$\tilde{E}(z,t) = \vec{E}_0 e^{i(kz-\omega t)} + c.c., \tag{2.9}$$

where $\vec{k}(=\omega n/c)$ and ω are the wave vector and angular frequency respectively. Therefore, the complex refractive index of the medium can be expressed as

$$\tilde{n}(\omega) = n(\omega) + i\kappa(\omega), \tag{2.10}$$

where $\kappa(\omega)$ is the extinction coefficient and which is related to the absorption coefficient, $\alpha = 2\omega\kappa/c$. Therefore, equation 2.9 can be rewritten as

$$\tilde{E}(z,t) = \vec{E}_0 e^{i\omega(nz/c-t)} e^{-\alpha z/c}. \tag{2.11}$$

2.2.2 THz generation by optical rectification

When EM radiation interacts with materials, polarization occurs because of displacement of charges from their equilibrium positions driven by the external electric field ($\tilde{E}(t)$). When the applied electric field is weak, the charges in the medium exist in a parabolic potential and experience a linear restoring force. Therefore, the induced polarization of the material can be described as

$$\tilde{P}(t) = \varepsilon_o \chi^{(1)} \tilde{E}(t), \tag{2.12}$$

where $\chi^{(1)}$ is the linear susceptibility tensor.

For strong applied electric fields, the polarization can result from charges experiencing a non-parabolic potential, resulting in nonlinear response to the electric field. So, the nonlinear polarization can be expressed as a Taylor series expansion, such that

$$\tilde{P}(t) = \varepsilon_o \sum_{n=1}^{\infty} \chi^{(n)} \tilde{E}^n(t), \tag{2.13}$$

where $\chi^{(n)}$ is the n$^{\text{th}}$-order susceptibility tensor. In high electric fields, all materials experience a third-order nonlinear response due to the inherent odd symmetry, but only non-centrosymmetric materials experience second-order nonlinear effects. Optical rectification (OR) is such a second-order nonlinear phenomenon.

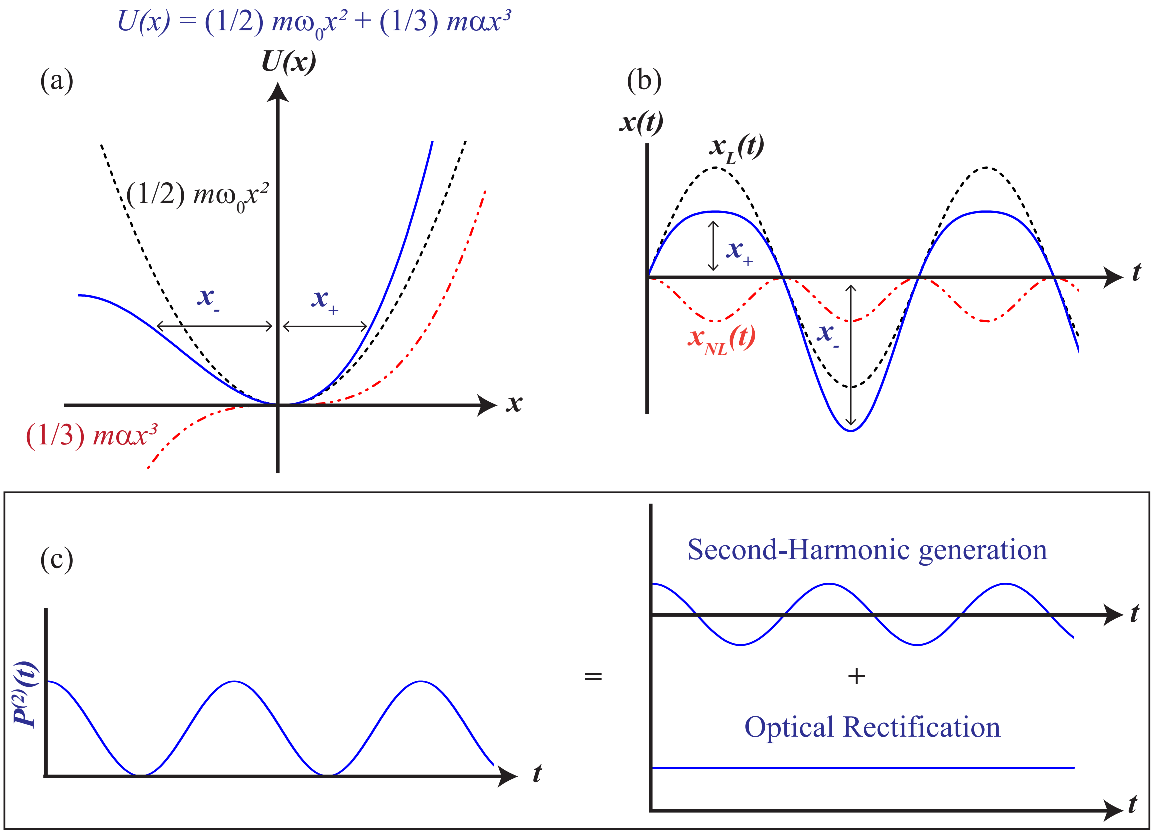

Figure 2.2: (a) Electric potential energy. (b) Electron motion in non-centrosymmetric system. (c) Second-order nonlinear optical process. The figures are redeveloped considering the ref [96].

Figure 2.2(a) shows the asymmetric potential energy for charges in noncentrosymmetric crystals, which is described by the quadratic term of the Taylor expansion. The solid line represents the total potential energy which results in a nonlinear response to the motion of electrons. This nonlinear motion is illustrated in Figure 2.2(b), where $x_L(t)$ and $x_{NL}(t)$ represent the linear and nonlinear components of the displacement of electrons. In terms of frequency mixing, the nonlinear response can occur either by the sum or difference frequency

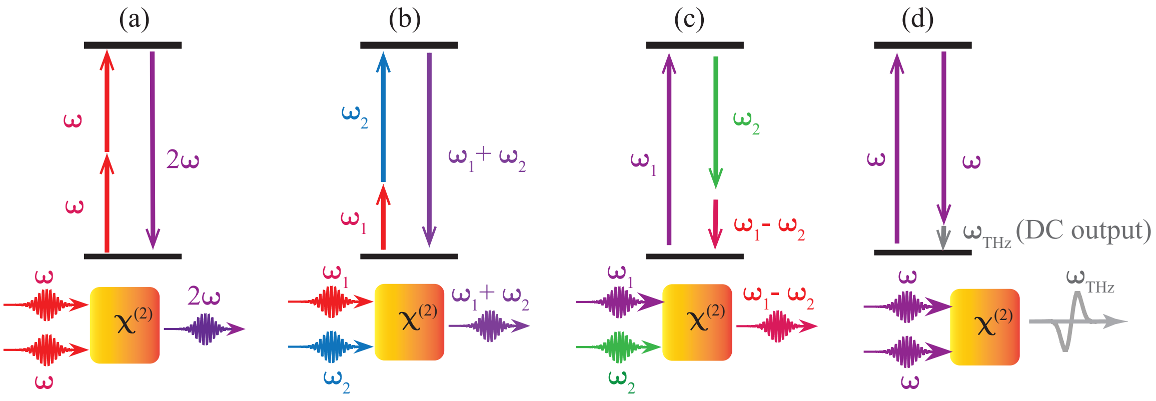

Figure 2.3: Illustration of second order nonlinear process. (a) Second-harmonic generation, (b) sum of frequency generation, (c) different-frequency generation, and (d) optical rectification.

mixing [96]. These mixing processes can be generalized for two distinct driving electric fields.

Returning to the wave equation,

$$\nabla^2 \tilde{E}(t) - \frac{1}{c^2}\frac{\partial^2 \tilde{E}(t)}{\partial t^2} = \frac{1}{\epsilon_o c^2}\frac{\partial^2 \tilde{P}(t)}{\partial t^2}, \tag{2.14}$$

the $\tilde{P}(t)$ represents the time-varying polarization which acts as the source of the electromagnetic radiation. $\tilde{P}(t)$ consists of different second-order components.

$$\begin{aligned}\tilde{P}^{(2)}(t) = \epsilon_o \chi^{(2)}[E_1^2 e^{-2i\omega_1 t} + E_2^2 e^{-2i\omega_2 t} + 2E_1E_2 e^{-i(\omega_1+\omega_2)t} + 2E_1E_2^* e^{-i(\omega_1-\omega_2)t} \\ + 2\left(E_1E_1^* + E_2E_2^*\right) + c.c.]\end{aligned} \tag{2.15}$$

Equation 2.15 shows the various components of second-order polarization, such as second harmonic generation (SHG) (1^{st} and 2^{nd} terms), sum of frequency generation (SFG) (3^{rd} term), difference frequency generation (DFG) (4^{th} term), and OR (5^{th} term) which is illustrated in Figure 2.3.

A more generally nonlinear polarization expression for OR is

$$P_i^{(2)}(0) = \sum_{j,k} \epsilon_0 \chi_{ijk}^{(2)}(0, \omega, -\omega) E_j(\omega) E_k^*(\omega), \tag{2.16}$$

where indices i, j, and k represents the Cartesian components of the fields, and $\chi^{(2)}_{ijk}$ is the susceptibility tensor corresponding to the OR process. To generate non-DC components, it is apparent that a range of electric field components are needed to create a time-dependent polarization from these nonlinear crystals. To achieve this condition, pulsed lasers are used as the time-dependent source. These lasers typically have 10-100 fs of pulse duration. According to the Fourier theorem, the spectral bandwidth of the radiation is the inverse of the optical pulse duration, OR can generate broadband THz pulses in a nonlinear medium.

The THz generation efficiency through OR depends on the second order susceptibility tensor of the nonlinear crystal. In cartesian cordinates, this tensor can be represented as a contracted notation considering, $xx = 1,\ yy = 2,\ zz = 3,\ yz = zy = 4,\ xz = zx = 5,\ xy = yx = 6$ with $d_{im} = \chi^{(2)}_{ijk}/2$. Using this notation, nonlinear polarization matrix can be represented as

$$\begin{pmatrix} P_x \\ P_y \\ P_z \end{pmatrix} = 2\epsilon_0 \begin{pmatrix} d_{11} & d_{12} & d_{13} & d_{14} & d_{15} & d_{16} \\ d_{21} & d_{22} & d_{23} & d_{24} & d_{25} & d_{26} \\ d_{31} & d_{32} & d_{33} & d_{34} & d_{35} & d_{36} \end{pmatrix} \begin{pmatrix} E_x^2 \\ E_y^2 \\ E_z^2 \\ 2E_yE_z \\ 2E_zE_x \\ 2E_xE_y \end{pmatrix}. \tag{2.17}$$

Many of these elements vanish for highly symmetrical crystal systems, such as zincblende crystals (commonly used to generate THz by OR). Zincblende crystals belong to $\overline{4}3m$ crystal class, therefore $d_{14} = d_{25} = d_3$ are the only nonzero matrix elements.

Assuming the electric field of the laser is

$$\mathbf{E}_0 = E_0 \begin{pmatrix} \sin\theta\cos\phi \\ \sin\theta\sin\phi \\ \cos\theta \end{pmatrix}, \tag{2.18}$$

the nonlinear polarization matrix can be expressed as

$$\begin{aligned}\begin{pmatrix} P_x \\ P_y \\ P_z \end{pmatrix} &= 2\epsilon_0 d_{14} E_0^2 \begin{pmatrix} 0 & 0 & 0 & 1 & 0 & 0 \\ 0 & 0 & 0 & 0 & 1 & 0 \\ 0 & 0 & 0 & 0 & 0 & 1 \end{pmatrix} \begin{pmatrix} \sin^2\theta\cos^2\phi \\ \sin^2\theta\sin^2\phi \\ \cos^2\theta \\ 2\sin\theta\cos\theta\sin\phi \\ 2\sin\theta\cos\theta\cos\phi \\ 2\sin^2\theta\sin\phi\cos\phi \end{pmatrix}, \\ &= 4\epsilon_0 d_{14} E_0^2 \sin\theta \begin{pmatrix} \cos\theta\sin\phi \\ \cos\theta\cos\phi \\ \sin\theta\sin\phi\cos\phi \end{pmatrix}.\end{aligned} \tag{2.19}$$

Here, ϕ and θ represent the azimuthal and polar angles. Hence, the generated THz field is parallel to the polarization, and the field intensity becomes angular dependent

$$I_{THz}(\theta,\phi) \propto |\mathbf{P}|^2 = 4\epsilon_0^2 d_{14}^2 E_0^4 \sin^2\theta \left(4\cos^2\theta + \sin^2\theta\sin^2 2\phi\right). \tag{2.20}$$

The maximum field intensity is achieved when, $\phi = \pi/4, 3\pi/4$ such that $\sin^2 2\phi = 1$, where the polarization is in the $\{110\}$ plane of the zincblend crystal.

Beyond the polar and azimuthal angles, the THz field intensity depends on the nonlinear material's electro-optic (EO) coefficient. The relationship between second-order nonlinear susceptibility tensor and the EO coefficient (r_{ijk}) can be represented as $\chi_{ijk} = -\left(n^4/2\right) r_{ijk}$, where n is the refractive index of the material. Therefore, materials with a high EO coefficient can achieve strong THz fields, assuming appropriate crystal orientation.

Additionally, the material thickness will govern the THz signal strength, because the thickness of the crystal depends on the velocity matching. Due to the frequency dependency of the refractive index $n(\omega)$, the group ($v_{gr}(\omega) = \partial\omega/\partial k$, where $k(\omega) = n(\omega)\omega/c$) and phase ($v_{ph}(\omega) = \omega/k$) velocities differ. Therefore, the velocity matching condition can be achieved when the v_{gr} of the driving $\tilde{E}(t)$ is as same as the v_{ph} of the central frequency of the broadband THz spectrum. The velocity matching condition of the nonlinear materials depends on the material dispersion, which can be characterized by the coherent length.

$$l_c = \frac{c}{2\nu_{THz}|n_{gr} - n_{THz}|}, \tag{2.21}$$

$$n_{gr} = n_0(\lambda) - \lambda\frac{\partial n_0}{\partial\lambda}, \tag{2.22}$$

where v_{THz} and n_{THz} are the THz phase frequency and refractive index, respectively. n_{gr} represents the optical group refractive index, where λ is the optical wavelength, and n_0 is the respective refractive index corresponding to the λ.

2.2.3 Electro-optic sampling for THz detection

The electro-optic and photoconductive sampling methods are the most common methods used to record complex THz spectrum in the time domain. These methods measure amplitude and the phase of the spectrum with higher precision. The working principle behind the EO sampling is the Pockels effect in EO crystals, which can be represented as

$$P_i^{(2)}(\omega) = 2\sum_{j,k}\epsilon_0\chi_{ijk}^{(2)}(\omega,\omega,0)E_j(\omega)E_k(0). \tag{2.23}$$

Assuming the medium to be lossless, where $\chi_{ijk}^{(2)}(0,\omega,-\omega) = \chi_{ijk}^{(2)}(\omega,\omega,0)$, the equation 2.23 can be rewritten as

$$P_i^{(2)}(\omega) = 2\sum_{j,k}\epsilon_0\chi_{ijk}^{(2)}(0,\omega,-\omega)E_j(\omega)E_k(0). \tag{2.24}$$

By comparing equation 2.24 and equation 2.16, it is apparent that both the processes consist of the same second-order nonlinear susceptibility tensor. According to equation 2.24, the applied electric field is proportional to the field-induced birefringence in the nonlinear optical material. Therefore, the applied THz electric field, can be measured by considering

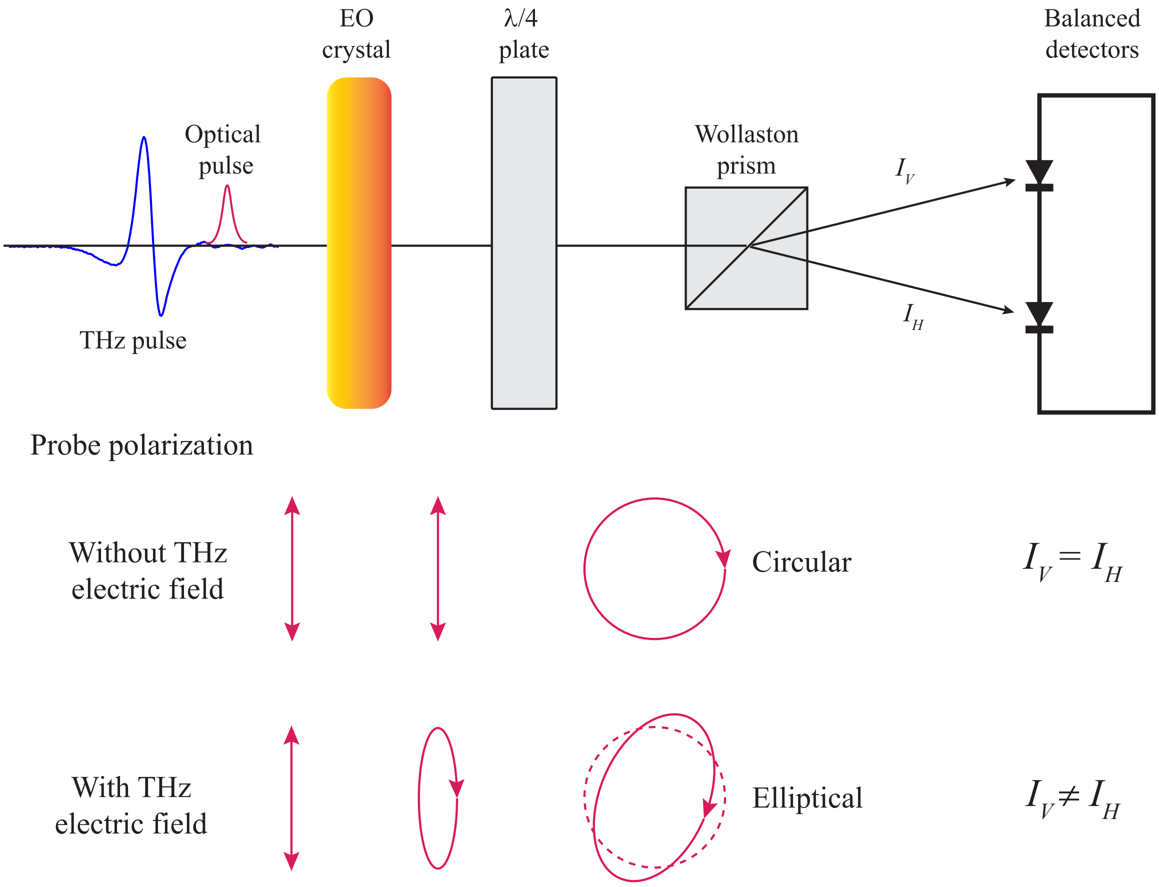

Figure 2.4: Diagram of EO sampling. Polarization of probe pulse with and without THz electric field

the field-induced birefringence.

Figure 2.4 shows the standard setup of EO sampling to detect THz signal. If the THz field is not present in the system, the optical pulse does not experience any birefringence. So the linear polarized optical pulse changes into a circularly polarized pulse when passing through the $\lambda/4$-wave plate then into equal orthogonal linear components in the Wollaston prism. Balance photo-detectors measure equal intensity of the EO gate pulse. In the presence of the THz field, when the optical group velocity matches with the THz phase velocity in the EO crystal, the optical pulse experiences birefringence. Therefore, the optical pulse produces an elliptically polarized pulse after passing through $\lambda/4$-wave plate and unequal orthogonal contribution in the balanced detectors. in the Wollaston prism and the balanced detectors. The detectors measure the intensity difference between these orthogonal components. The detected intensity imbalance is proportional to the applied THz electric field to the EO crystal.

ZnTe is a good candidate for the EO detection crystal because it exhibits good phase matching for THz frequencies for 800 nm optical(probe) pulse. Also it has a desirable EO coefficient ($r_{41} = 4$ pm/V), which helps to achieve efficient detection of THz electric field. It is found that the efficient THz detection can be achieved when the THz field and probe polarization are parallel to the $[1\bar{1}0]$ axis of a $\langle 110 \rangle$ crystal orientation.

Due to the Pockels effect in the EO crystal, the probe beam experiences differential phase retardation

$$\Delta\phi = (n_y - n_x)\frac{\omega L}{c} = \frac{\omega L}{c} n_0^3 r_{41} E_{THz}, \tag{2.25}$$

where ω is the probe center frequency, L is the thickness of the detection crystal, and n_0 is the refractive index at the probe frequency. The imbalanced intensity detected by the photo detectors can be described as

$$I_x = \tfrac{I_0}{2}(1 - \sin\Delta\phi) \approx \tfrac{I_0}{2}(1 - \Delta\phi), \tag{2.26}$$

$$I_y = \tfrac{I_0}{2}(1 + \sin\Delta\phi) \approx \tfrac{I_0}{2}(1 + \Delta\phi), \tag{2.27}$$

$$I_s(\Delta t) = I_y - I_x = I_0\Delta\phi = \tfrac{I_0 \omega L}{c} n_0^3 r_{41} E_{THz}(\Delta t), \tag{2.28}$$

where I_0 is the incident probe intensity. Therefore, time-domain THz fields can be mapped out by varying the delay time of the probe pulse.

2.2.4 Chalcopyrite crystals for THz generation

Solid-state nonlinear optical frequency conversion is central to photonics, allowing for the development of new sources for spectroscopy [61, 97] and other optical devices [98]. In OR, the relevant nonlinear tensor is $\chi^{(2)}(0;\omega,-\omega))$, so that short optical pulses are converted into pulses with THz center frequencies and THz bandwidths that are proportional to the source bandwidth.

THz pulses are routinely generated by OR in (110)-cut zincblende crystals, such as GaAs [99–101], GaP [75, 102, 103] and ZnTe [104–106], in tilted pulse front $\mathrm{LiNbO_3}$ [107–109] and tilted GaSe [110]. Only in 2012, Rowley *et al.* demonstrated that the chalcopyrite crystal $\mathrm{ZnGeP_2}$ (ZGP) also produces THz pulses by OR [72], determined the optimum phase-matching conditions considering the uniaxial birefringence [95] and that the it is suited to pulsed optical excitation at 1200 nm [72, 95, 111].

ZGP and other chalcopyrite crystals have $\overline{4}2\mathrm{m}$ symmetry [72], have strong uniaxial birefringence [95] and non-zero $\chi^{(2)}$ tensor elements $d_{14} = d_{25} \neq d_{36}$, although d_{36} is approximately equal in strength to the other tensor elements. Hence, ZGP is known for optical parametric generation to down convert near-infrared optical pulse into mid-infrared pulses [112, 113]. Moreover, chalcopyrite crystals have been explored for photovoltaic [18, 114, 115] and spintronic [116] applications. Recently, chalcopyrite $\mathrm{CdSiP_2}$ (CSP) has also been shown to be as a source of THz in the low-power regime [117]. This section complements the previous work by showing the first demonstration of OR in $\mathrm{CdGeP_2}$ (CGP), comparing it to the THz emission from ZGP and CSP. Measurements from the three crystals are presented over a broad excitation tuning range and into the high-power regime.

Single crystal ingots of chalcopyrite ZGP, CGP, and CSP are grown using a horizontal-gradient freeze method [118, 119]. From these high-quality (110)-cut crystals, double-side polished chips with an area of $\sim$1 cm^2 are thickness L = 0.5 mm for nonlinear optical applications [120–122]. Details of the growth process can be found in [118], Zawilski *et al.* Characterization of the quality is performed using an ellipsometry technique that exploits the strong birefringence of the material [123].

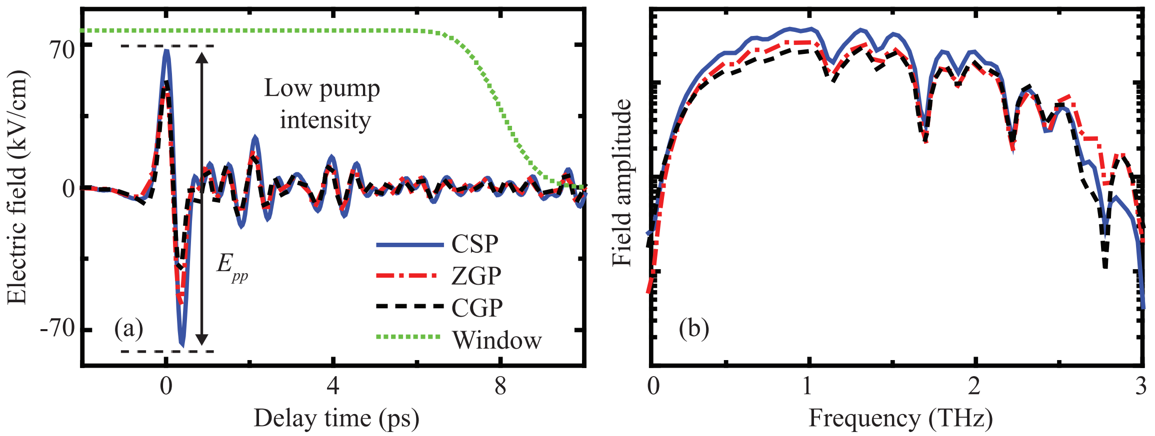

Figure 2.5: (a) Transient emission from $CdGeP_2$ (CGP), $ZnGeP_2$ (ZGP) and $CdSiP_2$ (CSP) at low intensity pump at 1300 nm. Also shown is the window function (not to scale). (b) Fourier transform of the transients to determine the emission amplitude spectra. Figure modified from Piyathilaka *et al.* [71].

Figure 2.5(a) shows typical THz transients for CGP, ZGP and CSP, measured with pump intensity $I_p = 5$ GW/cm^2 and photon energy $\varepsilon_{\mathrm{p}} = 0.95$ eV (1300 nm). The THz electric field is determined by

$$E_{\mathrm{THz}}(t) = \frac{\lambda_g i_{\mathrm{s}}(t)}{\left(2\pi L I_g n_0^3 r_{41} \rho_{\mathrm{det}}\right)}, \tag{2.29}$$

where i_s is the measure photocurrent in the lock-in amplifier, $\rho_{\mathrm{det}} = i_{det}/\mathrm{P}_{\mathrm{gate}}$ (i_{det} and $\mathrm{P}_{\mathrm{gate}}$ are detector current and gate pulse power) responsivity of the detector, the ZnTe refractive index is $n_0 = 2.85$ [124], the emitted THz the electro-optic coefficient is $r_{41} =$ 4 pm/V [96] and $\rho_{\mathrm{det}} = 0.009$ A/W at these power levels. The emission from the three crystals comprise of a fast, strong response with a duration of ∼1 ps, which is followed by weaker oscillations arising from interaction in the crystal and systematic ambient absorption in the THz path [72]. The three transients look very similar, with slight difference in the magnitude at the first shallow trough, the first tall maximum and the second deeper trough.

This result essentially illustrates different phases of the emitted radiation due to linear and nonlinear dispersions at both the optical excitation photon energy and the THz emission frequency [111].

Figure 2.5(b) shows the amplitude of the numerical Fourier transform of the experimental transients, which has been treated with an arctan window function (dashed green line) to remove the reflection of the gate pulse in the EO crystal at ∼12 ps and zero-padded before the transform. All three THz amplitude spectra are similar, peaking near ∼1 THz with bandwidths of ∼2.5 THz and ambient absorption, seen as dips at 1.2 THz, 1.4 THz, and 1.7 THz [72]. For the current excitation conditions, the strongest peak and integrated signal is from the CSP crystal. Emission from the CGP and ZGP is weaker, with only slightly different spectral signatures. The details are expected to depend on the crystal and the excitation conditions [123].

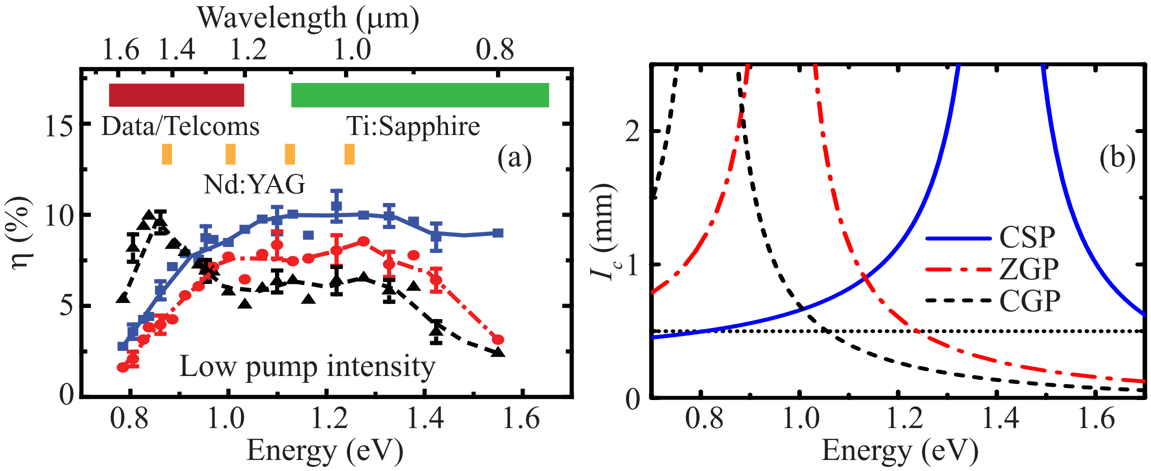

Figure 2.6: (a) Pump photon energy dependence of the emitted THz for $CdGeP_2$ (CGP), $ZnGeP_2$ (ZGP) and $CdSiP_2$ (CSP). (b) Calculation of the coherence length of the three crystals. Figure modified from Piyathilaka *et al.* [71].

Figure 2.6(a) shows the THz conversion efficiency, $\eta = I_{\mathrm{THz}}/I_{\mathrm{p}}$ as a function of excitation photon-energy from 0.8 eV to 1.55 eV. The pump intensity is fixed at $I_{\mathrm{p}} \approx 5$ GW/cm^2 and the THz intensity is $I_{\mathrm{THz}} = \xi \left|E_{\mathrm{pp}}\right|^2$, where E_{pp} is the peak-to-peak value of the emitted THz [illustrated on Figure 2.5(a)] and $\xi \approx 9.7$ is a scaling factor to account for the 2.5 THz bandwidth and the finite-lens correction for the off-axis parabolic mirrors [125]. Guides to the eye, based on a 15-point spline average, reveal that the CGP, ZGP, and CSP signal peaks at approximately 0.8 eV, 1.2 eV, and 1.4 eV respectively. This spectral range covers the data/telecoms range accessible by fiber lasers, the photon energy of Nd:YAG (and similar) lasers, as well as the range of Ti:sapphire lasers, illustrating the usefulness of these crystals as THz sources are applicable to broad excitation operation.

Table 2.1: Typical values for determining the coherence length. Table modified from Piyathilaka *et al.* [71].

	n_{THz} (@ 1THz)	n_g (0.65 - 1.78 eV)	n (0.65 - 1.78 eV)
CGP	3.43 [126]	3.34 – 5.63	3.24 – 3.74 [127]
ZGP	3.41 [128]	3.25 – 4.38	3.19 – 3.47 [127]
CSP	3.34 [129]	3.13 – 3.59	3.09 – 3.22 [130]

The spectral dependence of the optical rectification is governed by linear and nonlinear dispersion of the crystal at optical and THz frequencies, the nonlinear generation parameters determined from $\chi^{(2)}$ and the various absorption processes of the excitation and emission. Low-intensity investigations, such as shown in Figure 2.6(a), are only weakly dependent on nonlinear or free-carrier absorption processes and can be determined from linear and nonlinear refractive indices. The dispersion of the real part of $\chi^{(2)}$ is small and even unknown for some chalcopyrites. Hence, the initial comparison η (or E_{pp}) is only to the coherence length, which is described using equation 2.21. Figure 2.6(b) shows the calculation of l_c plotted as a function of photon energy for comparison to the above data. Values used to calculate the l_c curves are shown in Table 2.1.

A horizontal line is drawn at 0.5 mm in Figure 2.6(b) to indicate the measured thickness of the crystals. If the l_c estimates fall below this line, then in those regions, the emitted signals are expected to be reduced. The CGP and CSP follow the trend of the coherence length calculation, peaking close to the position of optimum l_c in each case. In comparison, ZGP has a much weaker dependence on the excitation photon energy. Overall, these results indicate that CGP is better suited to excitation with fiber lasers, ZGP is better suited to excitation with fiber and Nd:YAG lasers and CSP are better suited to excitation with Nd:YAG and Ti:sapphire lasers.

The scalable performance of the three THz sources is measured through the excitation-intensity dependence at several pump excitation photon energies. Figure 2.7 shows the strength of the THz emission E_{pp} over a range of excitation densities up to Figure 2.7(a) 15 GW/cm^2 at 0.805 eV, (b) 30 GW/cm^2 at 0.953 eV and (c) 120 GW/cm^2 at 1.55 eV. All three results are plotted over the same range, and the extended range excited at 1.55 eV is shown in the inset of Figure 2.7(c). For 0.805 eV excitation, the CGP emission remains strongest throughout the excitation intensity range, whereas for the other excitation photon energies, CSP emits the most.

In each measurement, the intensity dependence of E_{TH} grows linearly because $\partial E_{\mathrm{THz}}/\partial z \propto d_{36}I(z)$, where d_{36} is the nonlinear optical tensor for optical rectification and z is the direction of propagation through the THz source. Here, d_{36} and the effective tensor element d_{eff} are interchangeable because the crystals have identical orientation, and birefringence is not considered because the excitation field is purely o-wave. At higher excitation intensities, the signals saturate primarily due to nonlinear absorption, which follows a generalized form of Beer's law

$$\frac{\partial I(z)}{\partial z} = -\left(\alpha I(z) + \beta I^2(z) + \gamma I^3(z) + \ldots\right), \qquad (2.30)$$

where α is the linear absorption, β and γ are the two- (2PA) and three-photon absorption (3PA) coefficients.

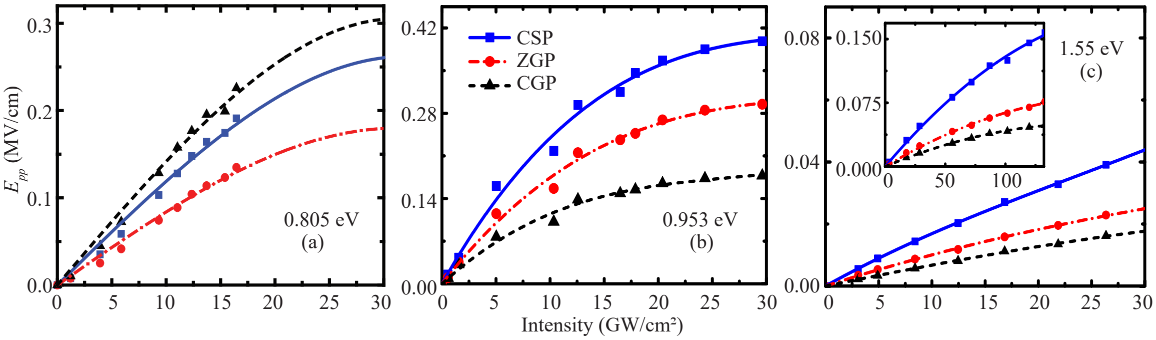

Figure 2.7: Excitation-intensity dependence of CGP, ZGP and CSP, excited at (a) 0.805 eV, (b) 0.953 eV and (c) 1.55 eV. The inset of (c) shows an extended range. Figure modified from Piyathilaka *et al.* [71].

Table 2.2 shows the values used to fit the curves for the three crystals and excitation photon energies. Following the scaling rules for 2PA and 3PA [131], β and γ are set to zero when the excitation is below the half ($E_g/2$) and one-third ($E_g/3$) band gap of the crystal being excited respectively. Moreover, values for d_{eff} are fixed based on literature values [132, 133], along with literature values of d_{eff} for ZnTe and LiNbO_3 for comparison.

For 0.805 eV excitation, the linear dependence of the THz amplitude rolls over, saturating due to 3PA. The fit values for the 3PA process scale with the strength of d_{eff}, indicating a fairly consistent nonlinear figure of merit far below bandgap. At 0.953 eV, direct comparison of the nonlinear absorption parameters is less straightforward because CGP exhibits 2PA. At 1.55 eV, all three crystals exhibit 2PA, although its effect is weak compared to that for CGP at 0.953 eV excitation. This occurs because 2PA is reduced closer to the direct bandgap and absorption preferentially transfers to the single-photon contribution. Hence, all fit values extracted at the respective excitation photon energies are consistent with the expectations for the linear and nonlinear response for these crystals.

Table 2.2: Fit values for absorption of integrated THz emission and nonlinear coefficients. Table modified from Piyathilaka *et al.* [71].

	d_{eff} (pm/V)	α (cm^{-1})	β (cm/GW)	γ (cm^3/GW^2)
		@(0.805 eV)		
CGP	109	14.52	-	0.0004
ZGP	75	15.87	-	0.0001
CSP	84.5	11.73	-	0.0002
		@(0.953 eV)		
CGP	109	15.8	0.2047	-
ZGP	75	17.01	-	0.0045
CSP	84.5	12.33	-	0.0091
		@(1.55 eV)		
CGP	109	31.18	0.0015	-
ZGP	75	17.88	0.0019	-
CSP	84.5	16.96	0.0034	-

Finally, even in the extended range of excitation density [shown in the inset of Figure 2.7], the weakly focused laser is below the laser damage threshold, which has been previously measured for anti-reflection-coated ZGP [134] and CSP [135] to be >2 Jcm^{-2} at 2 μm excitation and somewhat lower at 1 μm. Such values have not been explicitly measured for CGP, but they are expected to be of the same order.

In conclusion, chalcopyrite crystals have promising applications in nonlinear optics based on their large nonlinear coefficients, birefringence, and the availability of large-area growth. Moreover, larger emission strengths could be achieved by using (012)- or (114)-cut crystals [95] and larger excitation areas [106], possibly making these sources suitable for nonlinear THz spectroscopy.

2.3 Spectroscopy techniques

Figure 2.1 shows the EM spectrum in increasing frequency (or increasing energy) and decreasing wavelength. Different spectroscopy techniques can be employed with photon energies to match the interactions of intersest - also labeled. Absorption, reflection and emmision all produce valuable infromation.

Absorption spectroscopy can explore a semiconductor properties, including bandgap, density of states, and onset of other bands. Photoluminescence (PL) spectroscopy can also explore bandgap, optical transition levels, and radiative recombination mechanisms. As a semiconductor material is photoexcited, the excited carriers (electrons and holes) recombine radiatively or non-radiatively. In radiative recombination, the energy is emitted as photons, which provide the PL spectrum. This spectrum is used to gather comprehensive information about the behavior of the photogenerated carriers in the system.

To explore the structural properties, the spectroscopy techniques such as elastic scattering and reflection spectroscopy which employ high energy EM radiation such as x-ray, can be used. These techniques explore how incident EM radiation is reflected, transmitted, or scattered by the material; hence atoms' atomic compositions and arrangement can be examined.

2.3.1 Terahertz Time-Domain Spectroscopy

THz radiation is sensitive to light-matter interactions with free electrons, lattice vibrations, and rotational transitions due to the photon energies of THz stretching out in the meV range. Therefore, THz-TDS can be employed to discover the dynamics of these relatively unexplored interactions.

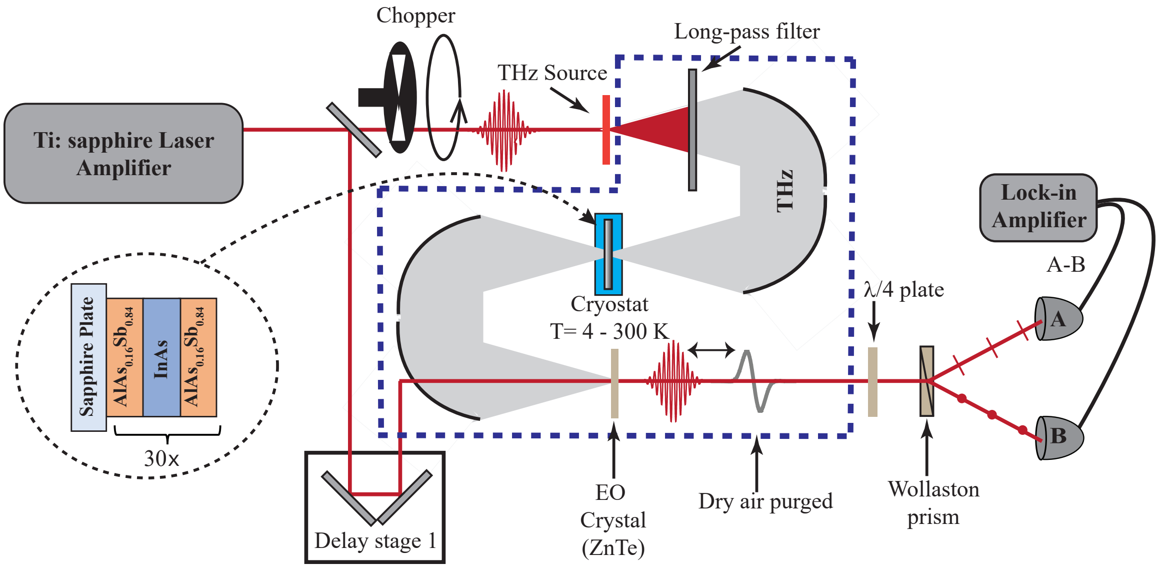

Figure 2.8: Schematic of the typical setup for THz time-domain spectroscopy (THz-TDS).

Generally, the investigation of electrical transport properties is carried out using contact-based Hall-effect measurements. One of the main drawbacks of this method is that the resistance of the contacts influences the electrical transport properties of the material. Therefore, THz-TDS has a significant advantage in these types of experiments due to its contactless and non-invasive nature. This technique measures the high frequency carrier transport on the picoseconds to the nanosecond time scale [136, 137]. The Fourier transform of the measured THz electric field gives the complex response spectrum in the frequency domain. Because of this, material characteristics such as conductivity, refractive index, dielectric constant, and extinction coefficient can be analyzed without performing Kramers-Kronig analysis [136, 138]. Analysis of this complex spectrum is discussed in the Chapter 3.

Figure 2.8 shows a schematic of a typical THz-TDS setup. The experimental setup consists of a 1-kHz regenerate laser amplifier producing $\sim$ 100-fs pulse with an 800 nm

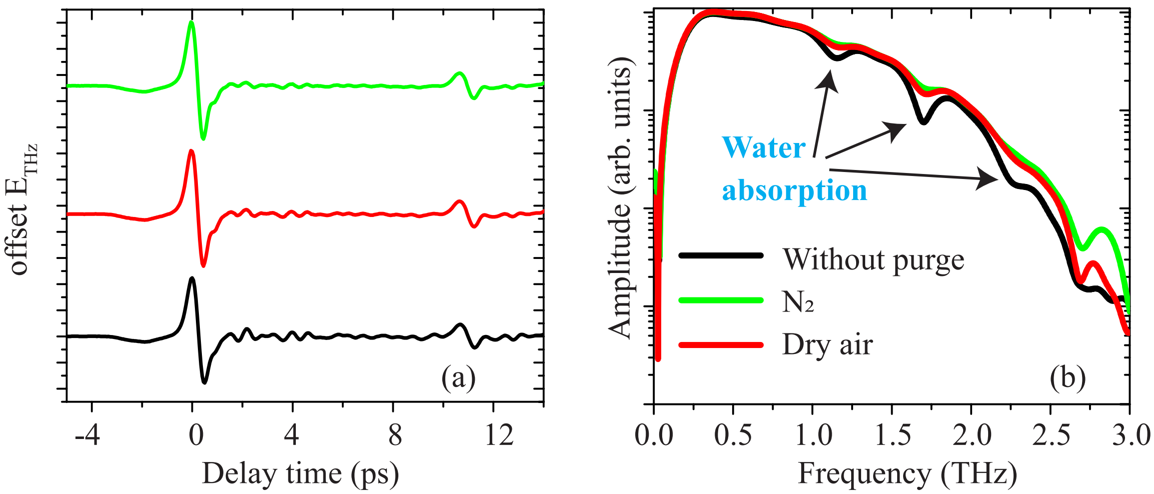

Figure 2.9: Evidence for reduction in water absorption. (a) THz transient with and without purging. (b) FFT of THz time domain transient.

center wavelength. The output of the amplifier was split into two beams for generation and detection THz. The THz pulses were generated using OR by weakly focusing the 800 nm pulse into a 0.5 mm thick (110)-CSP crystal [71] at the normal incident, with linear polarization oriented along (110) to generate maximum THz intensity. The THz emmision was filtered using a high-density polyethylene low-pass filter and forced into the sample through a pair of off-axis parabolic mirrors (OAPMs). The sample was placed in an optical cryostat, which controls the lattice temperature from 4 K to 300 K. THz transmitted through the sample was then collected and refocused into a 0.3 mm ZnTe EO crystal by another pair of OAPMs. The THz signal was detected by the EO sampling method. The gate pulse (pulse through delay stage 1) maps the THz-induced EO signal as a function of delay time (t), which is resolved by a Soliel-Babinet compensator, Wollaston prism, and a pair of balanced photodiodes connected to a lock-in amplifier. All-optical components from the THz source to the EO detection were purged with dry air or N_2 gas to reduce water absorption [see Figure 2.9].

2.3.2 Time-Resolved Terahertz Spectroscopy

The pump-probe technique can be employed to investigate the dynamics of non equilibrium charge carriers. In time-resolved Terahertz spectroscopy (TRTS), the THz is used as the probe pulse. Unlike other optical pump-probe techniques, which are sensitive to the sum or product of the electron and hole density, TRTS is sensitive to the conductivity generated by the non-equilibrium carriers. Therefore, TRTS is ideal for probing the electrical conduction properties of bulk and nanoscale materials [136, 139–141].

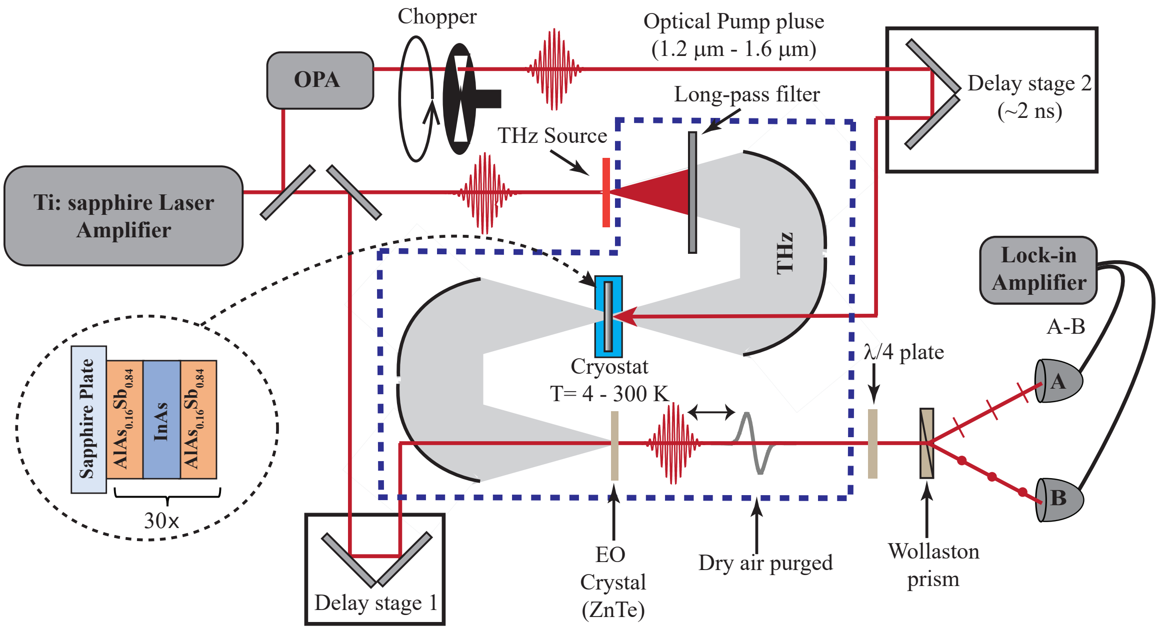

Figure 2.10: Schematic of the typical setup for time-resolve THz spectroscopy (TRTS).

Figure 2.10 shows the schematic of the TRTS setup. Here, the THz-TDS setup was modified by adding an optical beam to be used as a tunable optical pump. The tunable optical pulse is generated through an optical parametric amplifier (OPA), which has a tunable range from 1.2 μm (1.03 eV) to 1.6 μm (0.775 eV). The pump pulse was directed through a mechanical delay stage (Delay stage 2) to map out the photoexcited carrier dynamics in the time domain.

The AC photoconductivity measurements were carried out by capturing the change in transmission when the THz pulse is fixed at the peak value. This was achieved by fixing the delay stage 1 at the peak of THz and varying the pump delay stage (Delay stage 2). In this way, carrier dynamics such as lifetimes and recombination mechanisms of photoexcited carriers can be investigated [50, 142, 143]. By fixing delay stage 2 and varying delay stage 1, the complex THz AC photoconductivity spectrum can be obtained. By analyzing this THz spectrum, the photoexcited transport properties of the material can be investigated [83, 138, 144–147].

2.4 InAs/AlAs$_{0.16}$Sb$_{0.84}$ Multiple-quantum wells sample

This dissertation makes use of the previously discussed spectroscopic techniques to investigate the dynamics of a MQW structure. The binary compounds, InAs, and AlSb are approximately lattice-matched with lattice constant ≈ 6.1 Å, and with bandgaps of 0.36 eV (InAs) and 1.615 eV (AlSb) [148, 149]. In this particular III-V system, Sb atoms in AlSb were replaced by As atoms to create AlAsSb [see figure 2.11(b)] and lower its bandgap.

These compounds is a zincblende crystal with $\mathrm{T_d^2} - \mathrm{F\bar{4}3m}$ group symmetry. Figure 2.11(a) shows the crystal structure, based on diamond lattice with a diatomic and binary basis. In this case, atoms are in groups III and V, and each atom is bonded with sp^3 bonds to the nearest neighboring opposite type atoms.

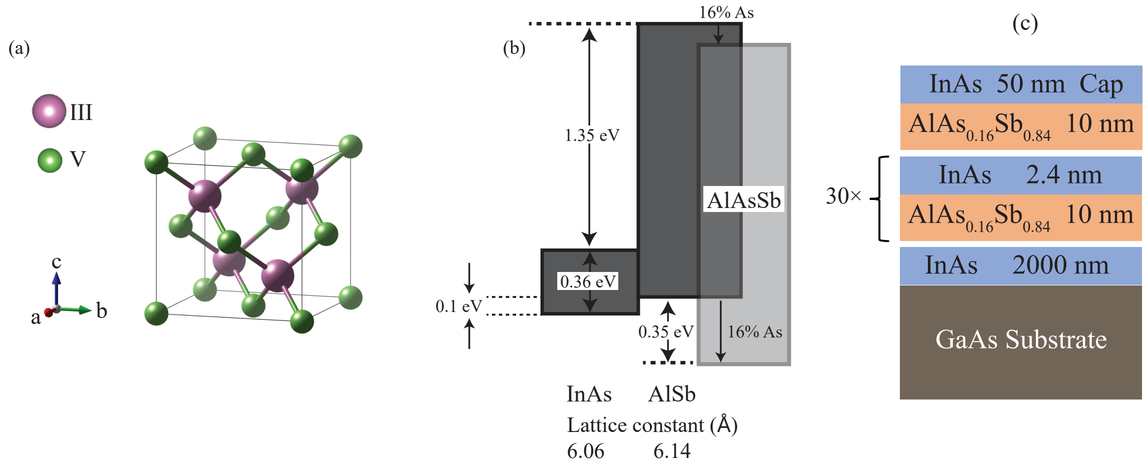

Figure 2.11: (a) Zincblende crystal structure. (b) Band lineup of InAs, AlSb, and AlAsSb. The shaded area represents the energy gaps. Figure modified from Kroemer [148]. (c) Schemetic of the InAs/AlAs$_{0.16}$Sb$_{0.84}$ MQW sample. Figure modified from Esmaielpour *et al.* [49].

2.4.1 MBE growth and process of superlattice

A type-II InAs/AlAs$_{0.16}$Sb$_{0.84}$ MQW structure is grown using the molecular beam epitaxy, consisting of 30 periods of 2.4 nm InAs quantum wells and 10 nm of AlAs$_{0.14}$Sb$_{0.86}$ barriers. The AlAs$_{0.14}$Sb$_{0.86}$ barrier material was grown on a semi-insulating GaAs (001) substrate [Figure 2.11(c)]. At first, the temperature of the substrate was increased up to 580 ^{0}C to remove the oxide. Then at 465 ^{0}C temperature, a 2 μm thick InAs buffer layer was grown on the substrate to relax the strain in order to produce a strain-relaxed heterostructure. Then the MQW system was deposited at 475 ^{0}C. As the final step, a 50 nm InAs cap layer was deposited at 465 ^{0}C temperature to isolate the Al-containing barrier.

To facilitate transmission for the THz-TDS measurements, the InAs buffer between the GaAs substrate and heterostructure region was removed with a combination of mechanical

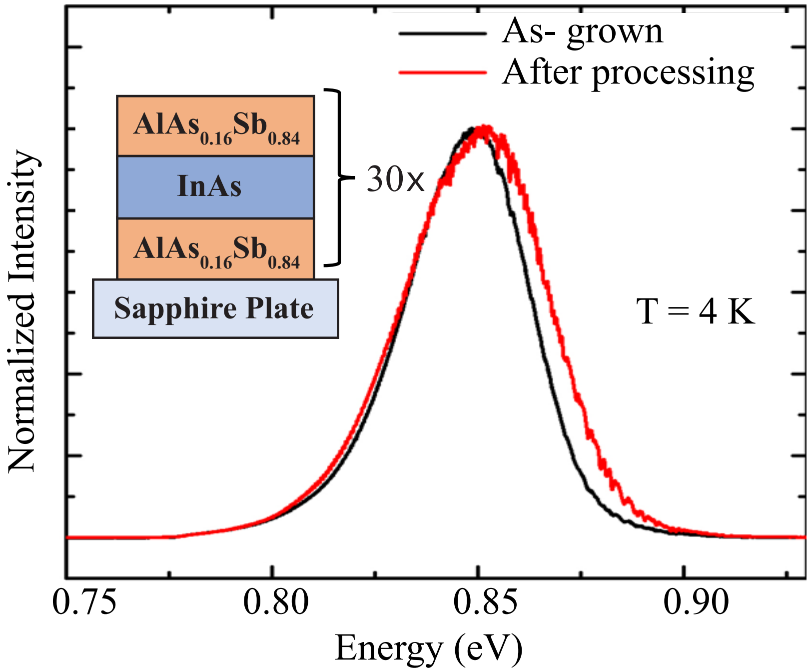

Figure 2.12: Photoluminescence spectra before (black) and after (red) processing for THz measurements. Inset shows the schematic of processed MQW structure mounted on sapphire. Figure modified from Esmaielpour *et al.* [50].

polishing and a dilute selective wet etching. First, the sample was immersed into concentrated citric acid ($C_6H_8O_7$) (1 g $C_6H_8O_7$ powder:1 ml distilled water (H_2O)) and hydrogen peroxide (H_2O_2) with (5:1) concentration for 60 seconds to remove 50 nm of InAs cap layer. After groth, the sample was mounted on 1 cm^2 sapphire substrate using Norland Optical Adhesive (NOA88) and cured with UV light. The GaAs substrate was removed by mechanical polishing and etched with NH_4OH:H_2O_2:H_2O solution in ratio of 1:3:16. Finally, to remove the InAs buffer layer, the sample was immersed in the same solution for 40 minutes. A schematic of the processed sample is represented in the inset of Figure 2.12. There is a slight blue shift in the PL signal of the MQW structure after the process [see Figure 2.12]. This is due to the strain relaxation of the structure [50] after the removal of GaAs substrate. By comparing the PL spectra before and after processing, it is clear that the integrity of the MQW structure remained unaffected.

2.4.2 InAs/AlAs$_{0.16}$Sb$_{0.84}$ superlattice

The type-II MQW structure has large confinement for electrons in the quantum well and low confinement in holes at valence band [Figure 2.13(a)]. Figure 2.13(b) shows a Tauc plot recorded by the Fourier transform infrared (FTIR) spectroscopy, performed under ambient temperature. Using the Tauc plot, the sample absorption coefficient (α) can be calculated by, $\alpha hv = A\left(hv - E_g\right)^{1/n}$, where E_g is the bandgap, hv represents the energy of the photon, and $A = -\log\left(I/I_o\right)$, where I_o and I represents transmission through the background and the sample respectively. The value for n can be determined by considering the nature of the electron transition from conduction to valance band. For direct transitions $n = 1/2$, and for indirect transitions $n = 2$. In this system, the Tauc plot is best fitted with $n = 0.9$, saying that the MQW structure demonstrates the properties of infinite quantum well [142] [refer to Figure 2.13] due to the confinement of the quantum wells in the system.

According to Figure 2.13(b), the bandgap of the superlattice lies around 0.83 eV at room temperature. This is in agreement with the PL peak data presented in Figure 2.13(d). Additionally, the Tauc plot indicates the split-off band energy (Δ_0), which resembles the Δ_0 of InAs [149]. The spectral all lie on top of the strong Fabry-Pérot fringes due to the thin film nature of the sample.

Figure 2.13(c) and (d) show selected temperature-dependent PL spectra and the peak energies of PL spectra from 77 K to 300 K. With the increment of lattice temperature, PL peak shifts towards lower energy for temperatures less than 75 K [refer inset of Figure 2.13(d)]. Then, the peak shifts towards higher energy till the lattice temperature reaches $\sim$ 125 K (known as "*s-shape*" behavior). When the lattice temperature is above 125 K,

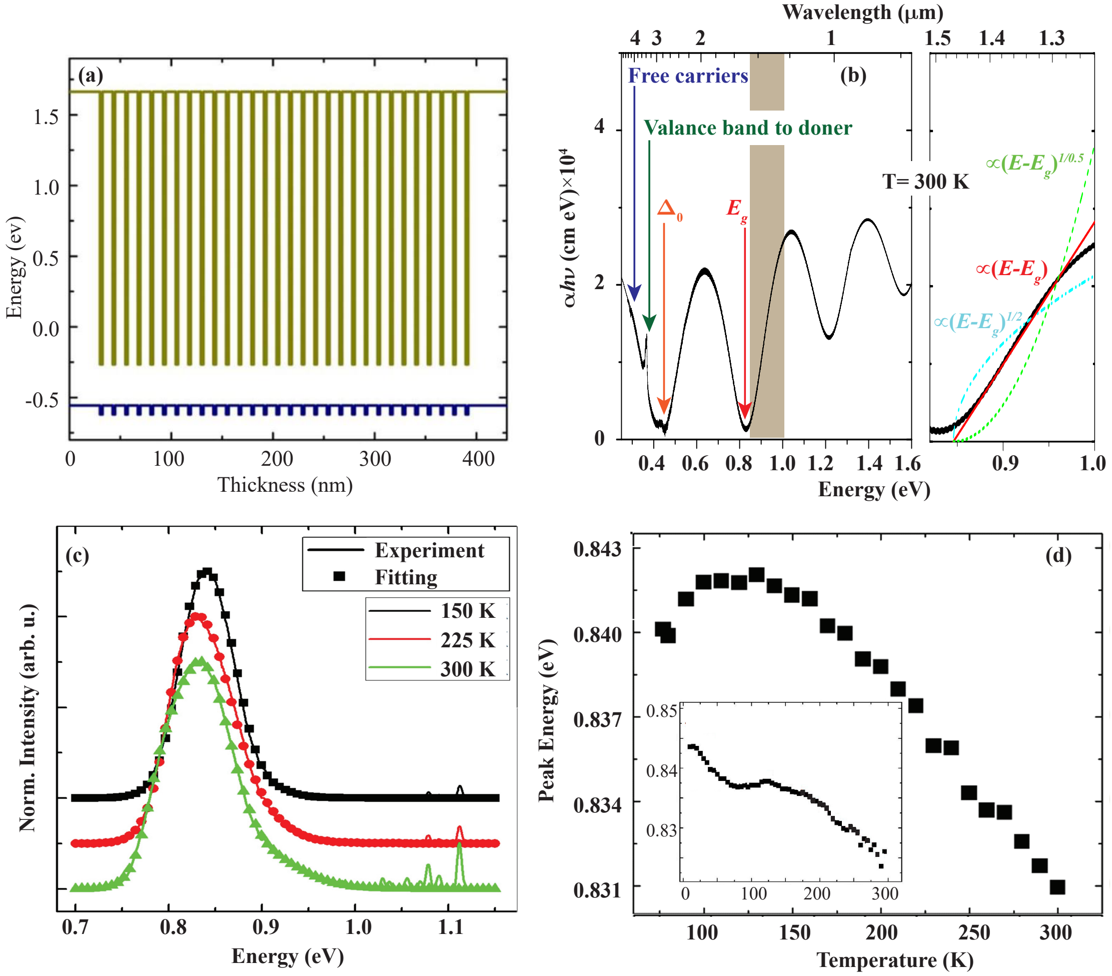

Figure 2.13: (a) Simulated energy profile of the InAs/AlAs$_{0.16}$Sb$_{0.84}$ MQW sample. Figure modified from Esmaielpour *et al.* [49] (b) Tauc plot of InAs/AlAs$_{0.16}$Sb$_{0.84}$ superlattice at room temperature.(Enlargement of shaded area represent the fittings for different n values)(c) Normalized temperature-dependent photoluminescence for 150 K, 225K, and 300 K. (d) The peak energy as a function of temperature. Figure (c) and (d) modified from Esmaielpour *et al.* [50] and Tang *et al.* [150].

the PL peak shift towards the lower energy. The behavior of the PL peak energy with the temperature is due to carrier localization [150] in the superlattice heterostructure. The *s-shape* behavior of PL peak energy ($T < 125$ K) is due to the trapping and de-trapping of the photogenerated carriers at localized states at the quantum well interface created due to alloy fluctuations. At elevated temperatures ($T > 125$ K), hole levels at the quantum well interface gain sufficient thermal energy to delocalize in the MQW superlattice. This causes the PL peak shift to lower energy.

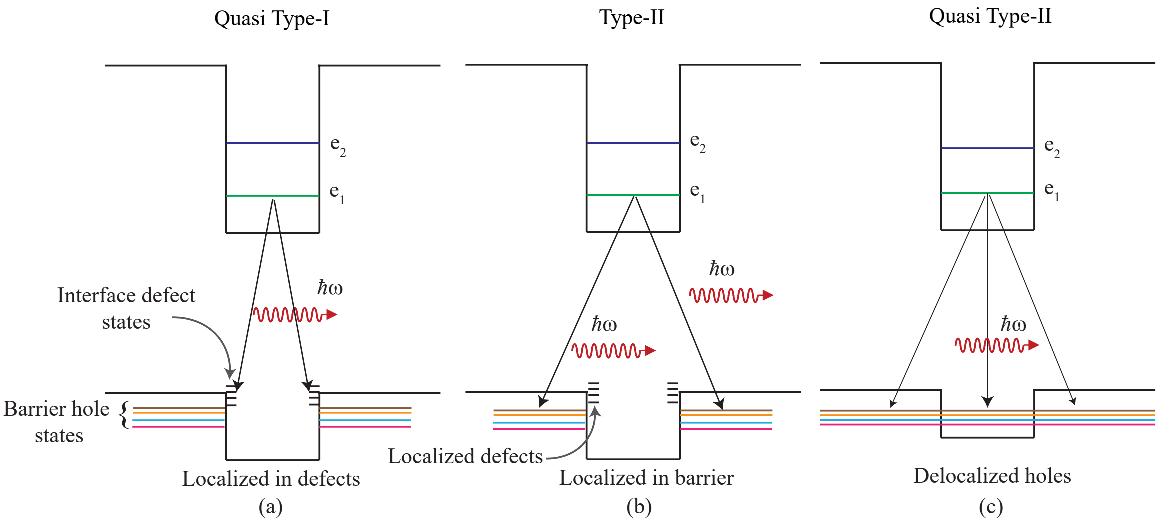

Figure 2.14: (a) Quasi-type-I recombination at $T < 100$ K dominated by quasi direct transitions between holes localized in alloy fluctuations and electrons in the QW. (b) Pure Type-II transitions between electron in QW and holes in the barrier, and (c) the quasi-II situation in which the holes states are degenerate and delocalized at high temperatures. Figure modified from Esmaielpour *et al.* [50].

This type-II MQW superlattice system demonstrates different recombination pathways of photogenerated carriers in the QW and barrier regions structure at different temperature. Figure 2.14 shows these effective transitions of the structure.

For $T < 100$ K, photoexcited electrons recombine into photogenerated holes at the valance band, where they are trapped as localized levels at QW interface states created by alloy fluctuations [refer to Figure 2.14(a)]. Therefore, in this temperature range, the band configuration of the structure is called quasi type-I. Due to this, the photogenerated electrons relax into localized states at the interface.

For the temperature range 100 K $< T <$ 225 K, localized holes at the interface get thermally excited, becoming unavailable for transitions and they relax into the nearest available hole states in the QW barrier, creating type-II band alignment in the system [Figure 2.14(b)]. Electrons in the conduction band have to recombine with holes at the AlAsSb barrier. The wave functions of the electron and hole are spatially separated which prolongs the lifetimes of hot carriers.

At elevated temperatures (225 K $< T$), due to shallow valance band offset (63 meV) [151], hole states wavefunctions are delocalized throughout the superlattice. This results in a stronger overlap of the electron-hole wave function. This regime is labeled quasi type-II band alignment [Figure 2.14(c)].

2.4.3 Type-II MQW band structure

The InAs/$AlAs_{0.16}Sb_{0.84}$ MQW structure consists of 30 periods of type-II multiple quantum wells. A schematic of type-II structure is showed in Figure 2.15(a). The structure consists of one light hole and three heavy hole levels in the valence band and two confined electron levels in the conduction band. Apart from that, the structure contains L and X (not shown in the schematic) valleys at 1.26 eV and 1.86 eV from the Γ point.

Figure 2.15(b) shows the calculated band structure for the $AlAs_{0.16}Sb_{0.84}$/InAs/$AlAs_{0.16}Sb_{0.84}$ superlattice based on an 8-band k.p model including temperature and strain dependent band parameters. This band structure was calculated using the Naval Research Laboratory's (NRL) MultiBands software tool [152] and reported in more detail by Whiteside *et al.* [151]. $AlAs_{0.16}Sb_{0.84}$/InAs/$AlAs_{0.16}Sb_{0.84}$ form quantum wells with type-II band

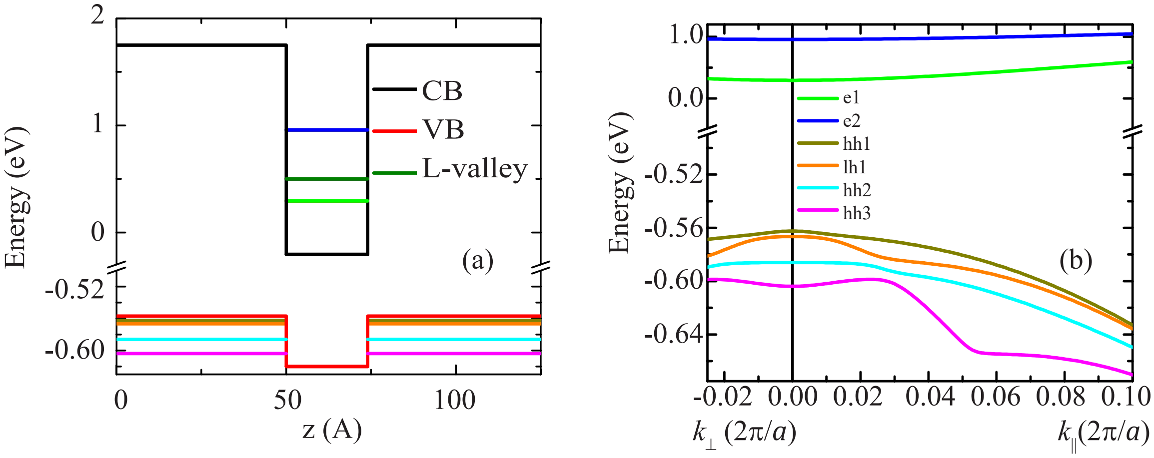

Figure 2.15: (a) Schematic diagram of the type-II quantum well stucture. (b) Band structure [151] of the InAs MQW superlattice. The inset shows the band minima and maxima of a single QW with confined energy levels at $k = 0$ cm^{-1}. Figure modified from Piyathilaka *et al.* [142].

alignment. Electrons in (e1 and e2) conduction sub-band states are confined in the InAs well, and heavy (hh1, hh2, hh3) and light holes (lh1) valence sub-band states are confined in the AlAs$_{0.16}$Sb$_{0.84}$ barriers. Figure 2.16 shows the calculated absorption. The bandgap is $E_g(T = 4\text{ K}) = 0.857$ eV arising from the e1-hh1 transition (denoted P$_1$). Transition from hole bands to e1 contributes to increased absorption above E_g, culminating in a peak absorption (P$_2$) at the e1-hh3 transition energy near 0.89 eV. The simulated optical absorption is determined from the band structure and the optical matrix elements. Not shown in Figure 2.15(b) are the L-valley and X-valley local minima of the e1 conduction band [153] which may also play a role in the scattering of the electron once photoexcited to sufficiently high excess energy.

Temperature contraction of the P$_1$ and P$_2$ transition energies are taken into consideration when determining excess-photon energy ($\Delta(T) = E_{pump} - E_g(T)$). Hole state occupancy (due to alloy intermixing defects in the well) and wavefunction localization/delocaliza-

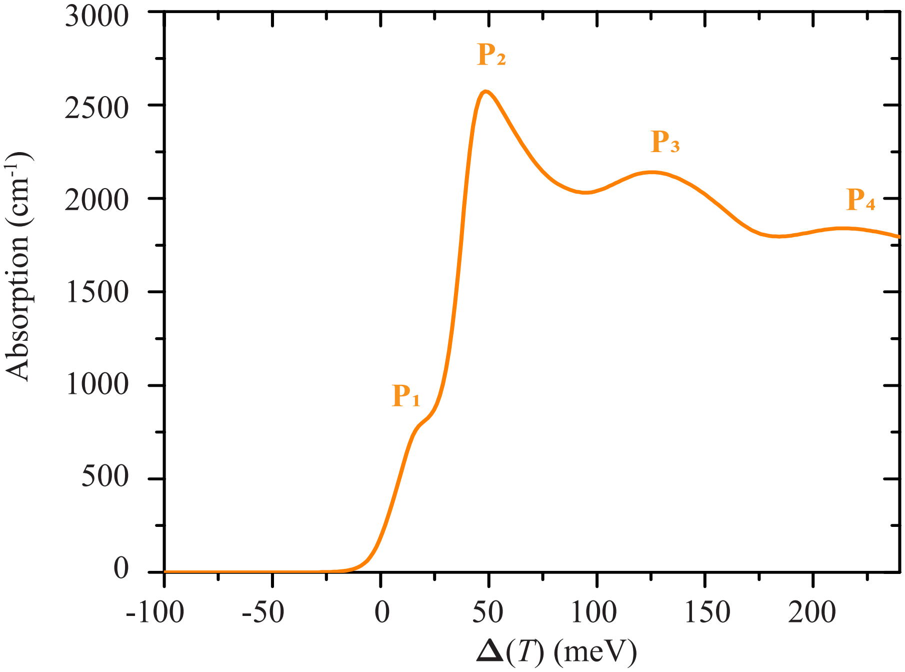

Figure 2.16: Simulated optical absorption of InAs/AlAsSb MQW structure. Figure modified from Piyathilaka *et al.* [142].

tion are also factored into account as the system transition from being quasi-type-I at 4 K to type-II at $\sim$ 150 K and quasi-type-II above that temperature [50].

Chapter 3:

Ground-state charge carrier transport

3.1 Introduction

Carrier transport is a crutial part of the puzzle for efficient photovoltaic devices. In this chapter we explore the AC conductivity because it will be a referance for the excited-state conductivity explored in Chapter 5.

Hall-effect measurement is the most commonly used technique for investigating the transport mechanisms in semiconductor materials. However, this technique uses contacts and measurements that become dominated by contact effects and the junction parameters such as resistivity. This can be overcome in noncontact all-optical measurements such as THz AC-photoconductivity [138, 154], where transport properties are measured using THz-TDS as the probe [71, 72]. Apart from that, THz-TDS facilitates the extraction of the material's complex optical properties without using the Kramers-Kronig relations [155].

In this chapter, THz AC-conductivity measurements are performed on InAs/AlAs$_{0.16}$ Sb$_{0.84}$ MQW structures for a range of lattice temperatures. THz AC-conductivity determines the unexcited carrier transport, in which the carrier concentration versus temperature is related to an average defect concentration, and the mobility is related to microscopic scattering mechanisms.

3.2 Ground-state conductivity

As discussed in section 2.3, THz-TDS is a reliable method to characterize AC conduc-

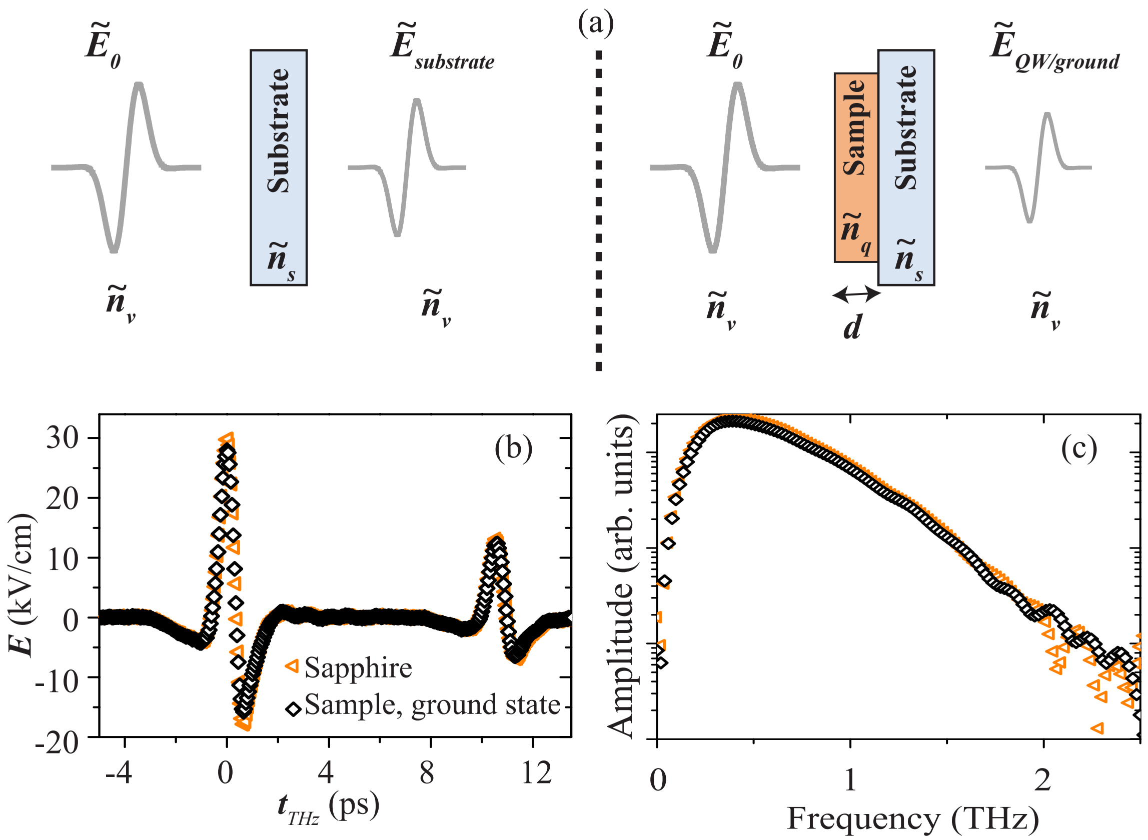

Figure 3.1: (a) Diagram of THz transmission through the MQW sample. (b) Transient of THz transmission through the sapphire substrate and InAs/AlAs$_{0.16}$Sb$_{0.84}$ MQW sample without photoexcitation. (c) Associated amplitude spectra resulting from a numerical Fourier transform.

tivity of materials. As shown in Figure 3.1, the complex transmission of THz is calculated by

$$\tilde{T}(\omega) = \frac{\tilde{E}_{\text{QW/ground}}(\omega)}{\tilde{E}_{\text{substrate}}(\omega)}, \tag{3.1}$$

where $\tilde{E}_{\text{QW/ground}}(\omega)$, and $\tilde{E}_{\text{substrate}}(\omega)$ are fast Fourier transform (FFT) of time-domain THz electric field transmission through sample and substrate [138].

The transmission of THz signal through the thin sample can be related to a propagation factor $\exp(i\tilde{n}\omega d/c)$, the Fresnel transmission t_{ij}, reflection r_{ij} and Fabry-Perot term

F_{ijk} [154]

$$\tilde{T}(\omega) = \frac{2\tilde{n}_q\left(\tilde{n}_v + \tilde{n}_s\right)}{\left(\tilde{n}_v + \tilde{n}_q\right)\left(\tilde{n}_q + \tilde{n}_s\right)} \exp\left(\frac{i\omega d}{c}\left(\tilde{n}_q - \tilde{n}_v\right)\right) \frac{FP_{vqs}FP_{qsv}}{FP_{vsv}}, \tag{3.2}$$

where subscript q,s and v indicate the QW sample, substrate and the vacuum respectively, d is the sample thikness and c is the vacuum speed of light. At normal incident

$$F_{ijk}(\omega) = \textstyle\sum_{p=0}^{P}\left[r_{ji}r_{jk}\exp\left(i\frac{2\tilde{n}\omega d_j}{c}\right)\right]^p, \tag{3.3}$$

$$r_{ij} = \tfrac{(\tilde{n}_i - \tilde{n}_j)}{(\tilde{n}_i + \tilde{n}_j)}, \tag{3.4}$$

where $\tilde{n}$ is the complex refractive index. In the Fabry-Perot term, p is determined by the number of internal reflections recorded in the time domain data. At the limits $p \to 0$ thick samples ($d > \lambda$) and $p \to \infty$ for thin films ($d \ll \lambda$). Here the thin-film limit is taken for the QW sample and the thick sample limit is taken for the substrate, where $\mid \tilde{n}_q\omega d/c \mid \ll 1$,

$$F_{vqs}(\omega) = \sum_{p=0}^{\infty}\left[r_{qs}r_{qv}\exp\left(i\frac{2\tilde{n}_q\omega d}{c}\right)\right]^p = \frac{1}{1 - r_{qs}r_{qv}e^{2i\tilde{n}_q\omega d/c}}. \tag{3.5}$$

Using Euler's formula and considering $\tilde{n}_v = 1$, transmission can be expressed as

$$\tilde{T}(\omega) = \frac{(1 + \tilde{n}_s)}{(1 + \tilde{n}_s) - i\left(\tilde{n}_q^2 + \tilde{n}_s\right)\omega d/c}. \tag{3.6}$$

This simplification is carried out considering the limits, $FP_{vsv} = FP_{qsv} = 1$ for thick sample, and $n_q\omega d/c \ll 1$, $\kappa_q\omega d/c \ll 1$, where κ_q is the extinction coefficient. Then taking a Taylor series expansion, it can be approximated $\cos(\tilde{n}_q\omega d/c) \sim 1$, $\sin(\tilde{n}_q\omega d/c) \sim \tilde{n}_q\omega d/c$, and $e^{-i\omega d/c} = 1$. The dielectric function becomes

$$\epsilon(\omega) = \epsilon_L(\omega) + \tfrac{i\sigma(\omega)}{\omega\epsilon_0}, \tag{3.7}$$

$$\epsilon_L(\omega) = \epsilon_\infty + \left(\epsilon_{dc} - \epsilon_\infty\right)\tfrac{\omega_{TO}^2}{\omega_{TO}^2 - \omega^2 - i\omega\gamma_{TO}}, \tag{3.8}$$

where ϵ_0, ϵ_L, and σ are permittivity of free space, lattice dielectric constant, and conductivity, respectively. ϵ_∞, ϵ_{dc}, ω_{TO}, and γ_{TO} are the high-frequency dielectric constant, static dielectric constant, transverse optical (TO) phonon frequency and phonon-damping constant. Here ϵ_L can be approximated to be ϵ_{dc} because phonon frequencies are typically above the bandwidth of the experimental range. Moreover, the refractive index of the material can be related to the dielectric constant, such that $\epsilon = \tilde{n}^2$. Therefore, using equation 3.6, the dielectric function of the QW sample (ϵ_q) becomes

$$\epsilon_q = \frac{ic\,(1+\tilde{n}_s)}{\omega d}\left(\frac{1}{\tilde{T}(\omega)} - 1\right) - \tilde{n}_s. \tag{3.9}$$

Comparing the equations 3.7 ans 3.9 and considering the sample to be highly conductive, the complex conductivity can be expressed as

$$\tilde{\sigma}_q(\omega) = \frac{(1+\tilde{n}_s)}{Z_0 d}\left(\frac{1}{\tilde{T}(\omega)} - 1\right), \tag{3.10}$$

where Z_0 is the free-space impedance represented as $Z_0 = \sqrt{\mu_0/\epsilon_0}$.

3.2.1 Conductivity models: AC-conductivity

THz is sensitive to all the free carriers in the system because the electric field drives this motion. The AC conductivity of the sample can be determined as a function of frequency through the numerical transform and the shape of the complex spectrum can be fit to different conductivity models, each with significant constraints on the carrier transport. Therefore, by fitting the complex conductivity [$\tilde{\sigma}_q(\omega)$] to the proper conductivity model, the DC conductivity, carrier density, scattering rate, and mobility of the sample can be determined.

3.2.1.1 Drude-Lorentz conductivity model

There are several conductivity models used to analyze frequency-dependent conductivity.

The most commonly used model is the Drude-Lorentz model, where the electron-hole plasma is considered to be a noninteractive gas. Moreover, collisions between carriers randomize their momentum with a characteristic scattering rate. Carriers undergo forced damped harmonic oscillationin response to the electric field, and the displacement (x) of carriers from its equilibrium point is given as

$$\frac{d^2x}{dt^2} + \gamma \frac{dx}{dt} = \frac{q}{m^*} E_{THz}, \tag{3.11}$$

where E_{THz} is the THz electric field, q is the charge, m^* is the effective mass, and $\gamma = 1/\tau$ is the scattering rate. Considering a plane THz electric field of the form of $E_{THz} = Ee^{-i\omega t}$, where ω is the angular frequency, the displacement takes the form $x = x_0 e^{-i\omega t}$. Substituting these in to equation 3.11 and using the polarization $P = \chi\epsilon_0 E = Nqx$, and dielectric function becomes equation 3.7. The conductivity can be derived as

$$\tilde{\sigma}_D(\omega) = \frac{Nq^2}{m^*}\frac{\tau}{1 - i\omega\tau}, \tag{3.12}$$

where N is the carrier density.

3.2.1.2 Drude-Smith conductivity model

However, for nanostructures [156], the Drude-Lorentz model does not describe the conductivity to interations with boundaries that lead to the backscattering of carriers. Therefore, an extension for this model was proposed by Smith [157], by allowing carriers to preserve part of their velocity after the first scattering event. The Drude-Smith conductivity model is given by

$$\tilde{\sigma}_{DS}(\omega) = \frac{Nq^2}{m^*}\frac{\tau}{1 - i\omega\tau}\left[1 + \frac{c_b}{1 - i\omega\tau}\right], \tag{3.13}$$

where c_b is the backscattering coefficient. This parameter is the expectation value of the scattering angle ($\langle\cos\theta\rangle$), such that $c_b = -1$ is complete backscattering and $c_b = 0$ recovers the Drude-like response without backscattering.

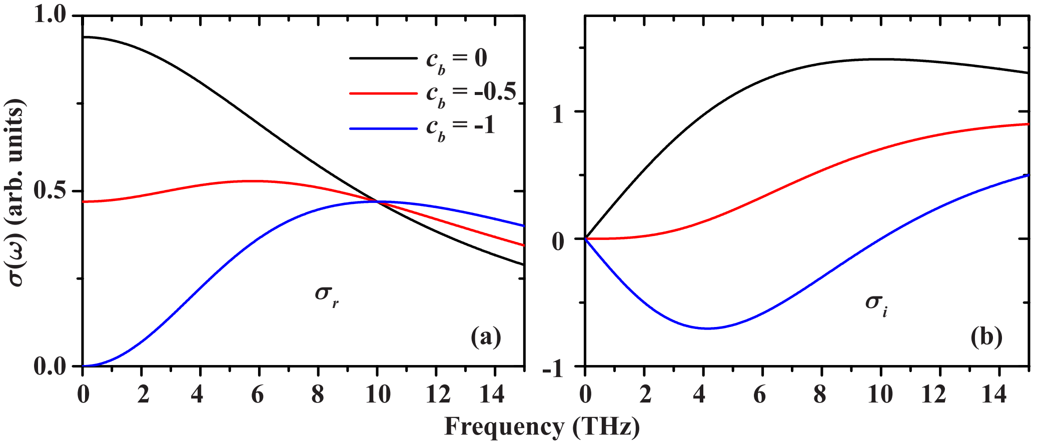

Figure 3.2: Simulated (a) real and (b) imaginary parts of conductivity using Drude-Smith model for different back-scattering values, c_b.

3.3 AC conductivity in InAs/AlAsSb MQW

The temperature-dependent AC conductivity was performed using the THz-TDS technique described in section 2.3.1. Figure 3.1(b) shows typical THz transients for transmission through the substrate (orange left triangle) and sample without (black diamond) photoexcitation. The region of the THz transient that is of interest is near time zero. This can be isolated by using a window function to remove the reflection of the THz near 10 ps, prior to performing a numerical transform to acquire the THz spectrum. In these transients, only slight difference in transmission is observed between substrate and sample indicating that the ground-state interactions are weak and suggesting low ground-state carrier density. Nevertheless, evaluation of THz AC conductivity is very sensitive to free carriers. For all temperatures, the spectral range of complex conductivity is chosen to be from 0.2 THz to

1.5 THz due to limitations in transmission through cryostat windows.

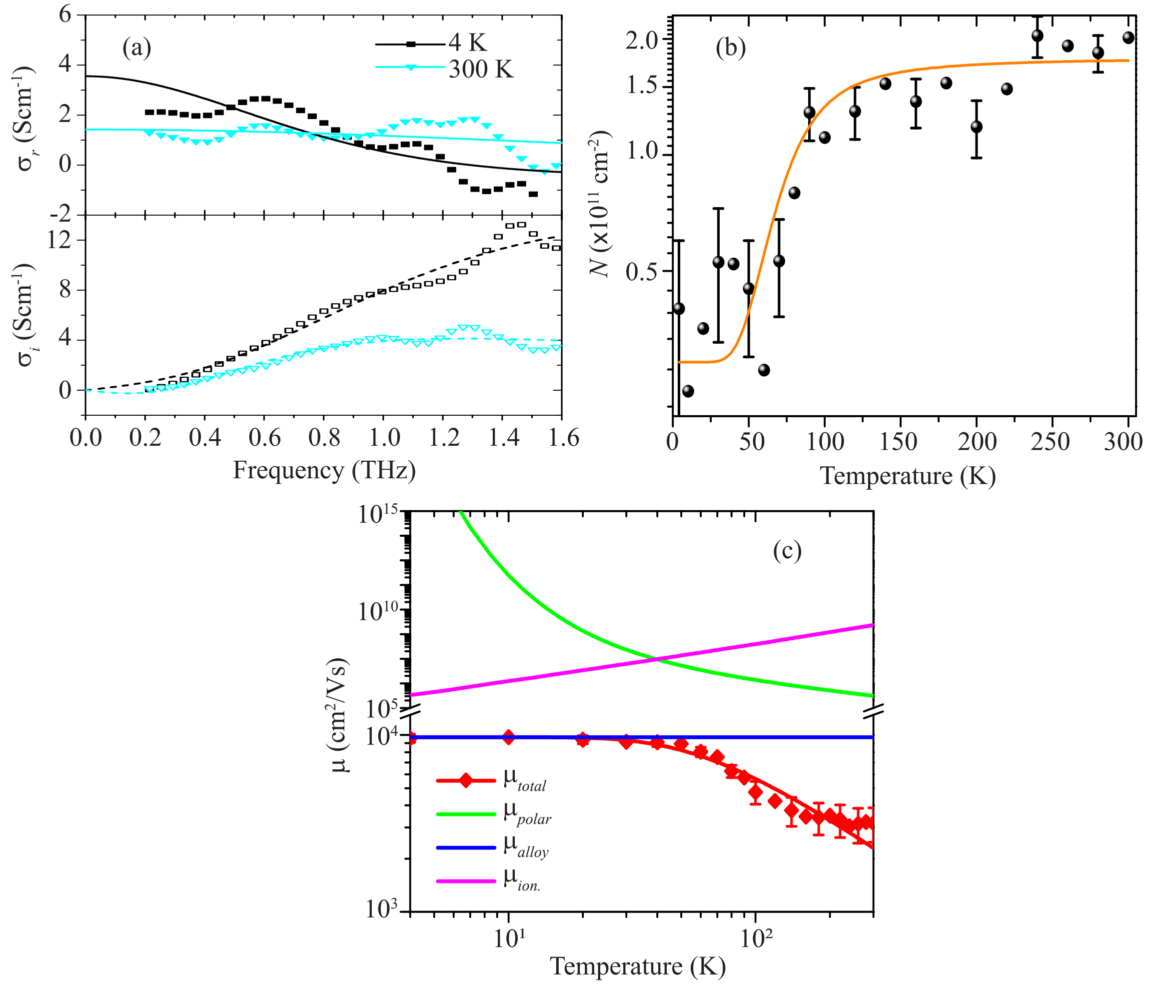

Figure 3.3: (a) Real and imaginary parts of ground-state conductivity for 4 K (black square) and 300 K (cyan down triangle); (b) temperature dependence of extracted carrier density fitted with Fermi-Dirac model; (c) Temperature dependent mobility fitted with a multicomponent scattering model.

The conductivity data were fitted using the DS model discussed in the previous section. Figure 3.3(a) shows the real and imaginary parts of the ground-state conductivity for 4 K and 300 K. For this system, the DS model was fitted with $c_b \approx -0.5$ for all temperature ranges, confirming the moderate back scattering at boundaries, as expected for the carrier dynamics in semiconductor nanostructures [138, 158].

Figure 3.3(b) shows the extracted ground-state carrier density from the DS fitting of the conductivity data as a function of temperature. The ground-state carrier density increases with the temperature due to Fermi smearing and increased occupancy in the conduction band. The temperature-dependent is fit to a Fermi-Dirac model [155] in order to determine the aggregate defect density and binding energy in the system. The occupancy is

$$N(T) = \frac{2N_D}{1 + \sqrt{1 + 4\hat{g}\frac{N_D}{N_c}\exp\left(\frac{E_D^b}{k_B T}\right)}}, \tag{3.14}$$

where N_D represents the net dopant density, and E_D^b gives the average dopant binding energy, $\hat{g} = g_1/g_0$, g_1 - the ratio of dopant / initial dopant degeneracy, T is the lattice temperature, and k_B is the Boltzmann constant. Here $N_c = 2\left[m_e k_B T/2\pi\hbar^2\right]^{3/2}$, m_e, represents mass of an electron and $\hbar$ is reduced Planck constant.

$N(T)$ is constant up to ≈ 60 K, above which it increases and saturates at approximately $120 - 150$ K. The onset of the low-temperature change in $N(T)$ corresponds to the quasi-type-I to type-II transition [50] (detailed discussion in section 2.4.2). The Fermi-Dirac fit suggests $N_D = 1.45 \times 10^{11}$ cm^{-2}, which agrees with the estimate of unintentional doping concentration ($\sim 10^{11}$ cm^{-2}), and with an aggregate binding energy $E_D^b = 13.36$ meV [142, 159–161].

Several temperature-dependent scattering mechanisms govern carrier transport in semiconductors. These scattering mechanisms include carrier-carrier, impurities, defects, and interactions with phonons in the system [138, 146, 147, 162]. The mobility can be defined using the scattering time (τ), the charge of the carrier (e), and the effective mass (m^*) of the carrier.

$$\mu = \frac{e\tau}{m^*}, \tag{3.15}$$

and combined with the Matthiessen's rule

$$\tfrac{1}{\mu} = \sum \tfrac{1}{\mu_i}. \tag{3.16}$$

Figure 3.3(a) shows the individual contributions and the combined mobility. The most relevant scattering mechanisms are chosen based on the geometry and characteristics of the MQW structure [138, 146].

Temperature-dependence of carrier transport is strongly influenced by the occupancy (or ionization) of impurities (or defects) states [155, 162], which is described as

$$\mu_{\text{ion}} = \frac{2^{7/2}\left(4\pi\epsilon_0\epsilon_s\right)^2 k_B T^{3/2}}{\pi^{3/2} Z^2 e^3 \sqrt{m^*}\ \ln\left[1 + \left(\frac{3\epsilon_0\epsilon_s k_B T}{2Ze^2 N_{ion}^{1/3}}\right)^2\right]}, \tag{3.17}$$

where N_{ion} is the ionization impurity density, ϵ_s is the low-frequency dielectric constant, ϵ_0 is the dielectric permittivity of free space, Z is the charge of ions, and e and m^* are physical quantities described above. Since the hetro-structure has quasi 3D wavefunction [40, 142], ionization impurity scattering of a 3D model is used.

Scattering is also expected from polar optical phonons, primarily because the phonon bottleneck results in optical phonon emission and reabsorption by the carriers. Polar optical phonon scattering is described as

$$\mu_{\text{polar}} = \frac{4\pi\epsilon_p\hbar^3}{\epsilon\theta_{pol} m^{*2} k_B d_0}\left(\exp\frac{\theta_{pol}}{T} - 1\right), \tag{3.18}$$

where $1/\epsilon_p = (1/\epsilon_\infty) - (1/\epsilon_s)$, with ϵ_∞ being high-frequency dielectric constant [163], θ_{pol} temperature of the phonon, and d_0 is the width of the quantum well.

Additionally, the MQW has many interfaces where alloy fluctuations are known to occur and hence affect the carrier transport. Alloy fluctuation scattering is given by [159]

$$\mu_{\text{alloy}} = \tfrac{16}{3b}\tfrac{e\hbar^3}{x(1-x)^2 m_{xy}^{*2}\Omega_0\Delta V_{al}^2}, \tag{3.19}$$

$$b = \left(\tfrac{33 m_z e^2 N(T)}{8\epsilon\hbar^2}\right)^{1/3}, \tag{3.20}$$

where ΔV_{al} is the alloy potential, x is the alloy mole fraction, m_{xy} is the interpolation of the transverse effective masses of AlAs and AlSb at the Γ point, Ω_0 is the volume occupied by one atom, N is carrier density, and m_z is effective mass in the growth direction [149].

It is evident that alloy scattering makes the mobility constant at lower temperatures, and polar optical scattering dominates at higher lattice temperatures. This behavior is consistent with the significance of the phonon bottleneck on excited-state carrier cooling and now also on ground-state transport. The extracted value of ΔV_{al} in alloy scattering is 8.1 meV, which is in the range of the potential of alloy fluctuations in the system ($8 - 9$ meV) [150]. Also, N_{ion} per well is 2.17×10^{15} cm^{-3}, which is in reasonable agreement with the N_D in Fermi-Dirac model which is 3.76×10^{15} cm^{-3}. Therefore, the temperature dependence of the ground-state mobility in the system suggests that mainly polar, alloy, and ionization impurity scattering mechanisms dominate the system.

3.4 Chapter Summary

The temperature dependent THz-TDS technique was employed to characterize the ground-state transport characteristics of the InAs/AlAsSb MQW structure. The ground-state carrier density follows Fermi-Dirac distribution with the carrier dopant density of 1.45×10^{11} cm^{-2}.

The ground-state mobility consists of ionization impurity, polar optical phonons, and alloy scattering. Alloy scattering contributes to ground-state mobility at low temperatures, while optical phonon scattering dominates at higher temperatures. The Ionization impurity scattering is negligible throughout the temperature range but not neglected because the system is unintentionally dopant.

Chapter 4:

Effect of phonon-phonon interactions in enhancing hot-carrier lifetimes

4.1 Introduction

Controlling the heat losses in the materials opens up potential pathways to enhance the performance of electronic devices such as near-infrared photodetectors [164], plasmonic devices [165], solar cells [55, 166], and specifically reducing the thermalization and cooling losses of hot carriers to develop HCSC [32, 39, 42, 167, 168].

In this chapter, the TRTS technique is employed to investigate the characteristics of hot carriers in the InAs/AlAsSb MWQ structure as a function of temperature for fixed pump excitation energy above the bandgap and fixed pump fluence. Temperature-dependent hot-carrier lifetime and carrier-relaxation mechanisms are extracted.

4.2 Hot-carrier cooling in InAs/AlAsSb MQW structure

Typically, hot carriers loose their energy due to thermalization and cooling via the emission of longitudinal optical (LO) phonons [Figure 4.1]. In III-V semiconductors, the coupling between carriers and phonons happens via Fröhlich interactions. In phonon-phonon interactions, LO phonons convert into two transverse acoustic (TA) phonons by the Klemens process [169]. These LO phonons can also dissipate into a combination of a TO phonon and a longitudinal acoustic (LA) phonon through the Ridley mechanism [Figure 4.2] [170]. This is possible for the acoustic modes with a larger wavevector to satisfy the energy convention.

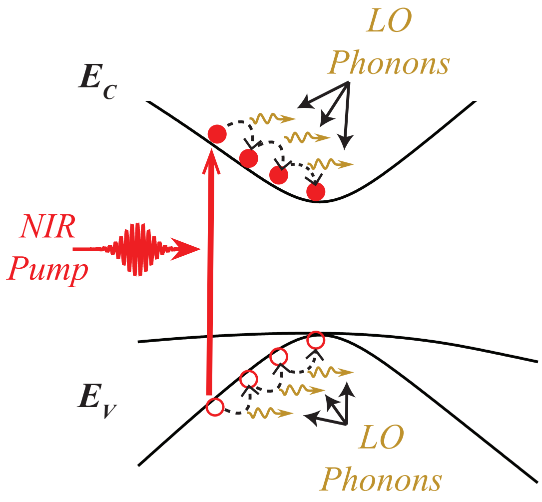

Figure 4.1: Schematic diagram of hot-carrier cooling in semiconductors.

In HCSC applications, the power conversion efficiency is improved by reducing the thermalization losses. Therefore, the absorber material in HCSC should have a low thermalization coefficient. Recent studies found that AlSb [171], InN [172], and BSb [173] materials show low carrier thermalization, which is suitable to be used as the absorber for HCSC applications. This phenomenon is mainly due to the sizeable phononic band gap in these materials. Due to this characteristic, Klemens process [169] usually dominates the phonon-phonon interactions.

Nevertheless, nonstructural materials, such as GaAs/AlGaAs MQW [174], also demonstrate slower carrier cooling rates than bulk materials. This is prominently due to the confinement of carriers in the low-dimensional structure. This causes a phonon bottleneck [48], and reduced cooling rates.

Figure 4.2(a) illustrates the carrier cooling process in the QW system. Upon creating hot carriers, carriers are cooled by the emission of LO phonons. These LO phonons are anharmonically coupled with LA phonons. In the InAs/AlAsSb MQW structure, due to the smaller effective electron mass in InAs QW, the conduction band's energy distribution is higher than the holes in the valance band. Therefore, electrons have better thermal distribution than the holes in the valence band. With increasing excitation density, the LO phonon density of the system increases, creating an imbalance in the phonon population. This is because LO phonon generation occurs faster than the Ridley and Klemens interactions. This phenomenon creates non-equilibrium LO phonons, which creates the phonon bottleneck [48] in this MQW system. Due to this bottleneck, the efficiency of cooling of hot carriers gets reduced. Therefore the carriers remain "hot" in the structure. Effectively this contributes to the longer lifetime of hot carriers.

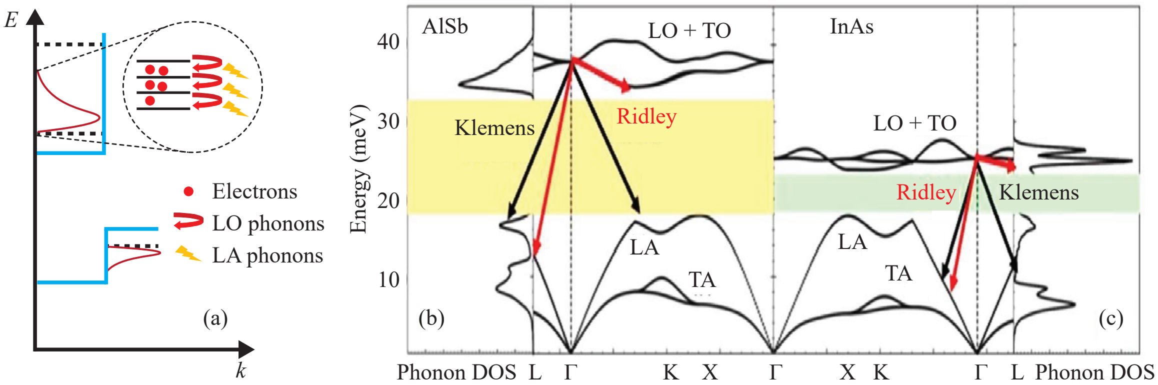

Figure 4.2: (a) Illustration of the relaxation of carriers through LO phonon emission and the subsequent generation of LA phonons in QW. Phonon density of states and dispersion calculated using density function theory analysis for (b) AlSb, and (c) InAs. The shaded regions indicate the difference the phonon band gap. Arrows represents the relaxation channels.(Black: Klemens and Red: Ridley). Figure modified from Esmaielpour *et al.* [50].

Figures 4.2(b) and (c) show the density functional theory calculations for phonon energy dispersion for AlSb and InAs. In modeling, the AlSb is used instead of AlAsSb, because As- contribution (16%) can be neglected from the calculations. Klemens's process becomes weak in polar semiconductors if LO phonon energy is twice the LA phonon energy. The energy ratio for LO and LA phonons in InAs is closer to 1, resulting in the Klemens process becoming strong. But, in AlSb $\hbar\omega_{LO}/\hbar\omega_{LA} \sim 1.9$ indicates a week Klemens process. This is due to the large phononic bandgap in the AlSb and the poor thermal conductivity [175].

On the inspection of phonon dispersion, the mismatch LO phonon energies in InAs and AlSb inhibit heat propagation between InAs QW and AlSb barrier [54]. Moreover, since thermal transport is low, it can be estimated that the acoustic phonon density of state is low. In semiconductor systems, heat propagation is mainly governed by the acoustic phonons. In this MQW system, acoustic phonon density is comparatively smaller than the optical phonon density due to the slow conversion rate of LO phonons to LA and TA phonons, creating high optical phonon density. The lower density of state provides a bottleneck in the phonon distribution and a reduction in the rate of optical-to-acoustic phonon transition. The higher occupancy of LO phonon modes during an excited carriers lifetime can then lead to reabsorption of the phonon by the carriers, stabilizing the hot carriers.

4.3 Hot-carrier lifetimes

Quantitative carrier lifetimes of photoexcited carriers are determined by TRTS, which measures the AC photoconductivity as a function of the delay time between a near-infrared pump pulse (at 1.03 eV) and a THz probe pulse for a series of lattice temperatures.

An optical pump pulse results in a photoexcited carrier density of $\approx 10^{14}$ cm^{-2} per well, based on the absorbance at 1 eV, the number of wells, and the average power of the laser beam on the sample and the pulse duration and repetition rate (or pulse energy). For pump-probe measurement, t_{THz} is set to the maximum of the THz transient, maximize the free-carrier absorption from optical pumping. Then the delay time ($\Delta\tau$) between the THz probe and the optical pump can be varied over a range of 2 ns, with $\approx$ 1 ps time resolution. The optical pump is mechanically chopped at a sub-harmonic frequency of the laser amplifier. The resulting differential transmission is detected in a lock-in amplifier, referenced to the pump modulation frequency.

The measurements presented in Figure 4.3(a) are recorded at the maximum THz field and only respond to the change in THz absorption $\Delta E(t)/E$ as a function of the pump-probe delay time (t), due to free carriers created by pumping above the band edge of the QWs. These free carriers cause additional absorption, which reduces the peak of the THz electric field. Transients are recorded for a range of temperatures from 4 K to 300 K that resolve both faster and slower decay dynamics. The fast decay dominates at low temperatures and is followed by a slower decay that dominates at higher temperatures. The transient decays are best fitted by a three-component model, which accounts for recombination through at least two sets of states. This is given by

$$\frac{\Delta E(t)}{E} = \sum_{i=1}^{3} A_i \exp\left[\frac{-(t-t_0)}{\tau_i}\right], \tag{4.1}$$

where A_i and $1/\tau_i$ are each component's amplitude and decay rates. This neglects the fast rise time recorded in the measurements, which is on the order of the cross-correlation of the excitation and THz pulses. Consequently, Figure 4.3 focuses on the decay processes and plots the temperature dependence of the amplitudes (b) – (d) and decay times (e) – (g).

Visual inspection of the three decay contributions reveals the fast component [$i = 1$, Figure 4.3(b, e)] to be significantly different mechanism from the intermediate [$i = 2$, Figure 4.3(c, f)] and slow [$i = 3$, Figure 4.3(d, g)] components. First, the amplitude of the fast decay [Figure 4.3(b)] decreases with temperature and has a slight monotonic increase of lifetime [Figure 4.3(e)] with temperature. The fast component is attributed to direct recombination within the QW due to recombination from the e_1 to localized hole states arising from alloy fluctuations, as illustrated schematically in Figure 2.14(a) [49, 150].

In contrast, the slower components grow in amplitude [Figures 4.3(c,d)] with tempera-

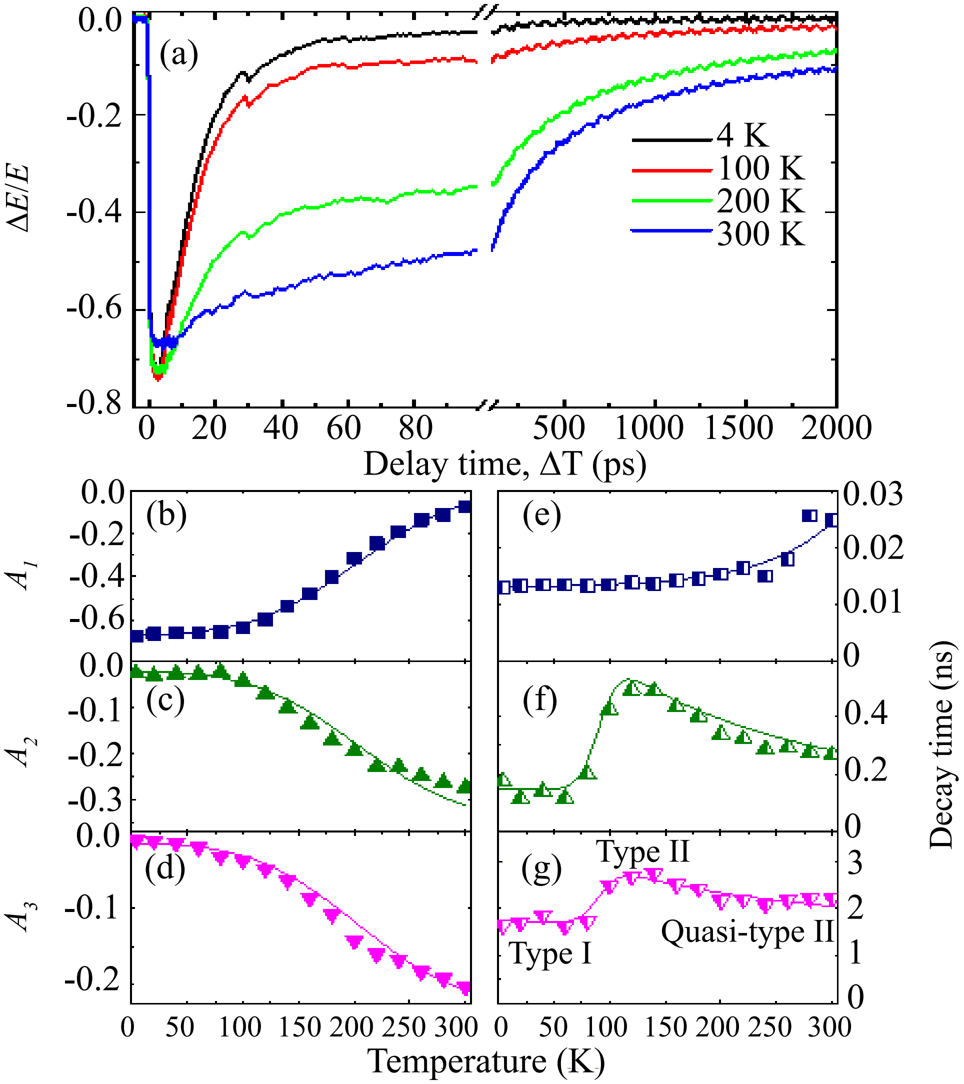

Figure 4.3: Carrier dynamics of MQW system: (a) Normalized differential terahertz (THz) transmission for a range of lattice temperatures. The inset shows the collinear experimental geometry of the THz probe and near-infrared (NIR) pump. (b) – (e) and (f) – (g) are the amplitude and decay times of the fast, intermediate, and slow carrier dynamics extracted from fitting the transients. In (g) the regions of type I, II, and quasi-type II are labeled. Figure modified from Esmaielpour *et al.* [50].

ture and have distinct non-monotonic lifetimes [Figures 4.3(f,g)]. This increasing lifetime with temperature directly probes the type-II [Figure 2.141(b)] transition and the thermally activated carrier escape above 100 K. Moreover, the temperature dependencies of the two slower components are highly correlated, most likely indicating that they can be attributed to a two-step decay process between the same sets of initial and final states. These competing transients are attributed to the redistribution of photogenerated holes and the degeneracy of the valence band at elevated temperatures; which leads to competition and the convolution of PL from multiple confined hole states and the ground-state electrons.

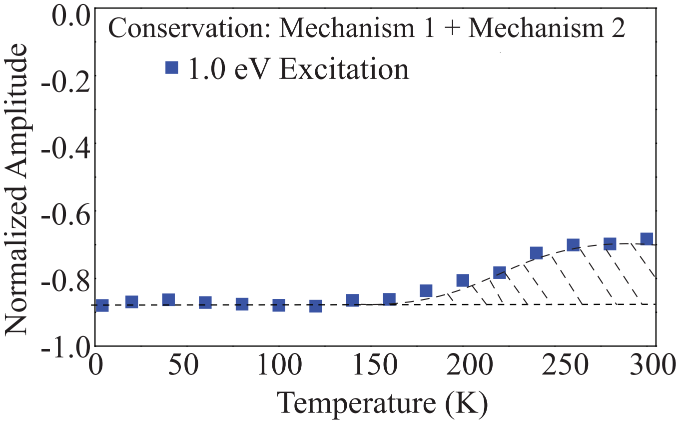

Figure 4.4: Temperature dependence of the sum of the amplitudes extracted from the transient absorption at each temperature. Mechanism 1 corresponds to A_1, mechanism 2 corresponds to $A_2 + A_3$. Figure modified from Esmaielpour *et al.* [50].

Figure 4.4 shows that summing the three transient amplitudes reveals a near-complete transfer from the fast to the slower components with increasing temperature. At temperatures below 200 K, there is a total amplitude of the signal of -0.8%, determined by A_1. At higher temperature A_2 ans A_3 dominates but the sum stays closer to -0.8%. This only starts to decay at higher temperatures indicating a weaker process emerges that reduces the absorption of pump light into a free-carrier absorption signal that modifies the transmitted

THz radiation. If $|A_1| \rightarrow |A_2$ & $A_3|$ then all processes are linked to the initial absorption and by the states that absorb. This means that the transfer in amplitudes is also dominated by the availability of a certain set of states involved in the recombination. Since it is known that hole states arising from alloy fluctuations become available at low temperatures, it is their availability, with holes as the minority carriers, likely dominate the temperature dependence of all the allowed transitions.

To fit the temperature dependence, an emperical model is used to link the availability of the alloy fluctuation states with the amplitudes of the decay mechanisms. In addition, the lifetimes of those states are associated with faster or slower dynamics. First, it is assumed that fast recombination can occur at low temperatures through the direct recombination between electron states and alloy fluctuation states within the well (quasi-type I system). The amplitude is determined as

$$A_1(T) = \frac{A_1(0)}{2} \operatorname{erfc}\left[\frac{T - \Delta E_{dh}/k_B}{w_{dh}/k_B}\right], \tag{4.2}$$

where $A_1(0)$ is the initial amplitude at low temperature, T is the temperature, $\Delta E_{dh}/k_B$ is the temperature where alloy fluctuation states become unavailable and w_{dh}/k_B is the range of temperature from completely available to unavailable; hence, ΔE_{dh} and w_{dh} are the corresponding energies of those last two variables.

Figure 4.4 shows that a complete conversion between the fast direct and the slower indirect decay mechanisms is nearly valid. Hence, the higher temperature reduction of the fast amplitude results in the growth of the slower indirect recombination mechanisms. This occurs between electrons in the well and holes in the barrier. Since both intermediate and slow recombination has nearly identical temperature dependencies, the inverse expression to equation 4.2 describes their behavior

$$A_{2,3}(T) = A_{2,3}(0) + C_{2,3}\frac{A_1(0)}{2}\left(1 + \operatorname{erf}\left[\frac{T - \Delta E_{dh}/k_B}{w_{dh}/k_B}\right]\right), \tag{4.3}$$

where $A_{2,3}(0)$ is the low-temperature decay rate for the intermediate (2) and slow (3) decay contributions, which are not forbidden only less likely, and $C_{2,3}$ are the branching ratios for the two decay contributions as they become more likely at higher temperatures.

Overall, in equations 4.2 and 4.3, the only relevant parameters for understanding the energy scales involved in the recombination amplitudes are ΔE_{dh} and w_{dh}. Their values are agree well with the peak energy shift and broadening of the PL data [50]. All the other parameters are fitting parameters associated with the total available densities of states of this specific sample.

Modeling these states as an allowed direct transition reveals a 17.5 meV energy difference from the hole states in the barrier with a 9.5 meV spread, which with the activation energy form localized to free carrier regime (quasi-type-I to type-II) determined previously [150].

Fitting the decay times for the fast (1), intermediate (2), and slow (3) contributions requires different behavior for the fast component in comparison to the two slower components. There also appears to be an interplay between the three. At low temperatures, the fast component dominates and suppresses the decay time of the slower components. At intermediate temperature, the sample transitions from quasi-type-I to type-II, increasing the time constants of the slower components. Finally, at the higher temperature, the delocalization of the hole states throughout the entire quasi-type-II system reduces the slower time constants while increasing the faster one.

The fast decay time is modelled as a low temperature component, $\tau_1(0) = 13$ ps, with an increasing temperature dependent contribution, $\tau_{1T} = 0.08$, such that

$$\tau_1(T) = \tau_1(0)\left[1 + \tau_{1T}\exp\left(\frac{k_BT}{\Delta}\right)\right], \tag{4.4}$$

where $\Delta = 5.5$ meV is the increase factor with temperature.

The intermediate and slower decay contributions are given by

$$\tau_{2,3}(T) = \tau_{2,3}(0)\left[1 + \tau_{2,3T}\left(1 + \operatorname{erf}\left[\frac{T - T_T}{T_W}\right]\right)\exp\left(-\frac{k_BT}{\Delta_{HT}}\right)\right], \tag{4.5}$$

where $\tau_2(0) = 150$ ps and $\tau_3(0) = 1700$ ps are fitting parameters for the suppressed low temperature time constants respectively, $\tau_{2T} = 2.6$ and $\tau_{3T} = 0.6$ are the rates of increase when the system becomes type-II. In both cases, the intermediate behavior is dominated by the second-order transition with temperature ($T_T = 95$ k) and transition width ($T_w = 20$ K) and finally by the reduction of these indirect transition times by $\Delta_{HT} = 14.6$ meV.

Modeling the fast lifetimes reveals a near temperature-independent lifetime of about 13 ps [Figure 4.3(e)], with a slight increase at the higher temperature that can be attributed to increased uncertainty as to the significantly longer-lived decay contributions become dominant. At low temperatures, the quasi-type-I (direct) recombination suppresses [Figure 2.14(a)] the time decay of the slower contributions. However, as the temperature is increased, the quasi-type-I components are switched off, and the true type-II (indirect) structure dominates the decay times [Figure 2.14(b)]. At very high temperatures, the hole states become more delocalized throughout the entire structure, such that the system is considered to be quasi-type-II [partly type-I – Figure 2.14(c)], which lowers the decay times of the slower carrier dynamics.

4.4 Chapter Summary

In this chapter, the TRTS experiment revealed enhanced hot-carrier lifetimes in type-II InAs/AlAsSb MQW heterostructure. As the lattice temperature of the system increases the hot carrier lifetimes get increased. This is attributed to the system's temperature-dependent band alignment (quasi-type-I, type-II, and quasi-type-II) with the temperature.

Chapter 5:

Metastability in excited hot-carrier population

5.1 Introduction

Bandgap engineering of monolithic structures to include quantum-confinement enhance optical absorption [176], type-II band-aligned quantum wells spatially separate electrons and holes to increase the excited-state carrier lifetime [50, 177] and structures with highly contrasting media can reduce the cooling through phonons [44, 178]. All of these properties occur in InAs/AlAs$_{0.16}$Sb$_{0.84}$ MQWs, where a hot-carrier distribution is shown along with extended carrier lifetime as a result of inhibited phonon-phonon interactions [50]. In steady-state PL, these MQWs have shown evidence of hot carriers [150], non-monotonic emission energy as a function of lattice temperature due to the complicated valence band structure [151], and even inter-valley scattering of electrons to the long-lived L-valley states [153]. Transient absorption directly shows long-lived carriers, complementing the evidence of hot carriers and the non-monotonic temperature dependence [50]. Phonon band structure calculation supports the suppression of Klemens' process that successfully converts optical phonons into acoustic phonons [169] in favor of the Ridley mechanism, which is less effective [170]. Moreover, poor thermal conductivity due to the phonon impedance mismatch between the MQW layers results in a hot acoustic bath. Overall, the entire electron-to-thermal cooling pathway is slowed, and the optical phonons can be reabsorbed by hot carriers, stabilizing them in non-thermalized states [50, 179].

This chapter, nonequilibrium carrier relaxation mechanisms are further investigated using the TRTS. These investigations are carried out as a function of temperature, pump energy, and pump intensity. The transient absorption data is converted into the rate equation to capture the carrier relaxation rates. This analysis gives insight into the carrier-density-dependent relaxation mechanisms.

5.2 Main recombination mechanisms in semiconductors

Before investigating the hot carrier dynamics of the MQW structure, understanding the carrier relaxation and recombination mechanisms in semiconductors is essential. In semiconductors, nonequilibrium carriers can be generated by electron beam injection via contacts or through the absorption of light that has photon energy exceeding the semiconductor's bandgap. With the initial excitation of carriers, the carriers thermalize and cool, typically occurring within 10-100 fs after excitation. Afterward, the carriers are relaxed into low-energy states in the band structure. Figure 5.1 illustrates the main recombination mechanisms in semiconductor materials.

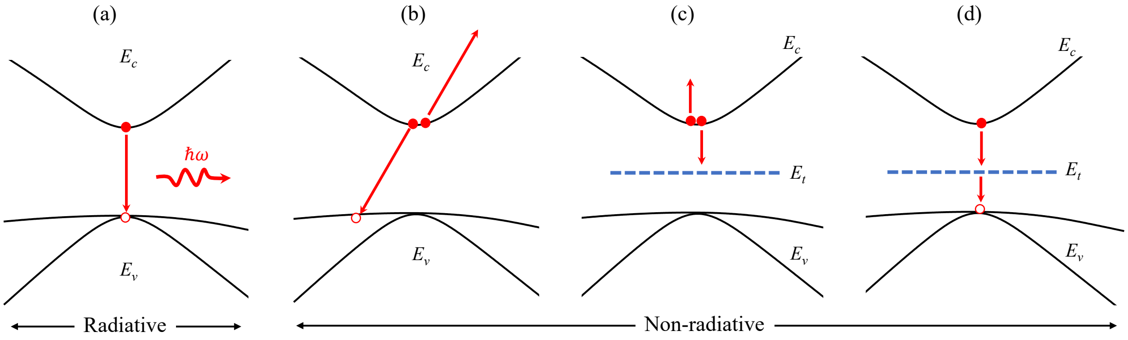

Figure 5.1: Diagram of recombination mechanisms in semiconductors. (a) Radiative recombination ($\sim np$), (b) Auger recombination ($\sim n^2p, np^2$), (c) Trap-assisted Auger recombination ($\sim n^2, p^2$), and (d) Shockley-Read-Hall (SRH) recombination ($\sim n, p$).

These mechanisms can be separated as radiative and non-radiative recombination processes. This classification is made because in the radiative process, the energy is released by the emission of photons, and for the non-radiative process, the energy is converted into heat by phonon emission, or electronic (holic) excitation.

Radiative recombination is the relaxation of excited electrons from the bottom of the conduction band to holes at the top of the valence band. This mechanism is also known as bi-molecular recombination and band-to-band recombination. This process is more prominent in direct bandgap semiconductors. During this process, when the recombination occurs, energy is emitted as photons with the energy of the semiconductor's bandgap. In indirect semiconductors, this process is less probable because it requires the assistance of phonons to undergo radiative recombination. Recombination in MQW superlattices are yet more complicated and the band structure needs to be calculated (see section 2.4).

The radiative recombination involves both electrons and holes [see Figure 5.1(a)]. Therefore, the rate of radiative recombination can be represented as

$$R_{RAD} = \beta \left(np - n_0 p_0 \right), \tag{5.1}$$

where n_0, and p_0 are equilibrium electron-hole concentration and n, and p total electron and hole density in the system. Here β is the radiative recombination coefficient, and the radiative lifetime can be expressed as

$$\tau_{RAD} = \frac{1}{\beta \left(n_o + p_o + n_{exc} \right)}, \tag{5.2}$$

where n_{exc} is excess electron density which equal to p_{exc}.

The prominent recombination process in a low-carrier injection regime is band-impurity recombination. This process is well known as Shockley-Read-Hall (SRH) recombination [Figure 5.1(d)], which was describes in 1952 [11]. This process is slow and considered non-radiative because no photon is emitted through this process. For SRH, the recombination rate can be represented as

$$R_{SRH} = \frac{\sigma_n \sigma_p v_{th} N_t \left(np - n_0 p_0\right)}{\sigma_n \left(n + n_t\right) + \sigma_p \left(p + p_t\right)}, \tag{5.3}$$

where N_t is the trap density and v_{th} is the thermal velocity which is in the range of 10^7 cm/s. σ_n and σ_p considered to be capture cross section for electrons and holes.

Considering these factors n_t and p_t can be represented by

$$n_t = \sqrt{n_0 p_0} \exp\left(\tfrac{E_t - E_F}{k_B T}\right), \tag{5.4}$$

$$p_t = \sqrt{n_0 p_0} \exp\left(-\tfrac{E_t - E_F}{k_B T}\right), \tag{5.5}$$

where k_B being the Boltzmann constant, E_F and E_t are Fermi energy level and trap energy level of the material respectively. Therefore, the lifetime of electrons and holes can be expressed as

$$\tau_n = \tfrac{1}{N_t v_{th} \sigma_n}, \tag{5.6}$$

$$\tau_p = \tfrac{1}{N_t v_{th} \sigma_p}. \tag{5.7}$$

Considering these expressions, the lifetime of the SRH mechanism can be represented as

$$\tau_{SRH} = \frac{\tau_p \left(n + \sqrt{n_0 p_0}\ e^{(E_t - E_F)/k_B T}\right) + \tau_n \left(p + \sqrt{n_0 p_0}\ e^{-(E_t - E_F)/k_B T}\right)}{n_0 + p_0 + n_{exc}}. \tag{5.8}$$

Auger recombination is more prominent in semiconductors at high injection rates. In this process, the energy of electron-hole recombination is released non-radiatively by promoting a third particle (electron or hole) deeper into their respective bands [Figure 5.1(b)]. This hot carrier eventually releases its excess energy via phonon emission. Since this process involves three carriers ($\propto n^2 p$ or $\propto np^2$) the recombination rate can be expressed as

$$R_{Auger} = C_n \left(n^2 p - n_0^2 p_0\right) + C_n \left(np^2 - n_0 p_0^2\right), \tag{5.9}$$

where C_n and C_p are Auger coefficient for electrons and holes. Therefore, the lifetime of this process can be expressed as

$$\tau_{Auger} = \frac{1}{\gamma\ n_{exc}^2}, \tag{5.10}$$

with γ being Auger-recombination coefficient.

If an excited carrier transition into a trap state and the released energy promotes another carrier this is known as trap-assisted Auger recombination [180], which is a non-radiative process that is slower than Auger recombination.

Therefore, with the initial generation of excess carriers, the relaxation of these carriers can be represented as

$$\frac{\mathrm{d}n_{exc}}{\mathrm{d}t} = -\frac{n_{exc}}{\tau} = -(\alpha\ n_{exc} + \beta\ n_{exc}^2 + \gamma\ n_{exc}^3 + \cdots), \tag{5.11}$$

where α being SRH coefficient, and τ is the carrier lifetime. Since the total carrier lifetime consists of individual recombination mechanisms, τ can be represented as

$$\frac{1}{\tau} = \frac{1}{\tau_{SRH}} + \frac{1}{\tau_{RAD}} + \frac{1}{\tau_{\text{Auger}}} + \cdots . \tag{5.12}$$

Similar process can be defined for holes.

5.3 Inversion analysis

Decay dynamics like Auger recombination and radiative recombination are not single-exponential decays and deviate from simple solutions. Typically, experimental results are fit to a sum of exponential functions with each decay constant assigned to a different decay mechanism. An assumption is made that all lifetimes are independent from the carrier density, which is only valid for low carrier injection rates and at least average at high carrier consentrations. Each component of the exponential sum can also considered to be attributed to a single loss despite carrier density. A single transient that comprises multiple decay mechanisms is a solution to the rate equation involving those decay mechanisms.

The inversion analysis technique transforms the transient back into the underlying rate equation at all carrier densities and overcome the assumptions made about mechanisms.

First, the transient absorption data are converted into carrier density [181] by

$$n_{exc} = -\frac{1}{\sigma d} \ln \left[1 - \text{abs} \left(\frac{\Delta E}{E} \right) \right], \tag{5.13}$$

where n_{exc}, σ and d are the excited carrier density, absorption cross-section and thickness of the sample. The σ is an energy dependent parameter, and can be found by

$$n_{exc} \approx \tfrac{I_0 \cdot \alpha_{pump}}{\hbar\omega}, \tag{5.14}$$

$$\tfrac{\Delta E}{E} = \exp(-\sigma n_{exc} d) - 1 \approx \sigma n_{\text{exc}}, \tag{5.15}$$

where I_0 and α are the incident pump flux (J/cm^2) and the absorption coefficient (cm^{-1}). Therefore, the σ is determined by taking the inverse of the slope of the maximum of the transient absorption and the excitation pump intensities.

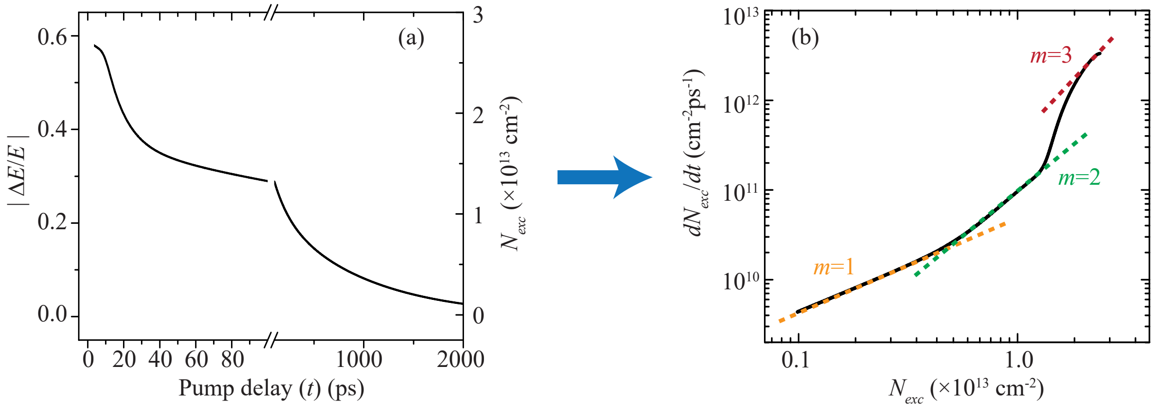

Figure 5.2: (a) Transient differential THz-electric field $[\Delta E(t)/E]$ through the MQW sample at 4 K for the excitation photon energy of 1.03 eV. (b) Relaxation and/or recombination rate of excited-state carriers. Dashed guides to the eye represent known recombination mechanisms ($m = 1$: SRH, $m = 2$: Radiative and trap-assisted Auger recombination, $m = 3$: Auger recombination).

5.4 Relaxation dynamics of hot carriers

5.4.1 Energy dependence of hot-carrier relaxation

The previous chapter discussed the transient absorption measurements of these InAs/ AlAsSb MQWs, performed at single excitation energy above the lowest interband transition, leaving unresolved the exact origin of the various competing phonon- and electron-scattering mechanisms that can contribute to the longevity of hot carriers [50, 179]. In this chapter, transient absorption measurements are performed for a range of excitation conditions (charge-carrier density and excess-photon energies) to disambiguate the complexity of the charge-carrier dynamics of InAs/$\mathrm{AlAs_{0.16}Sb_{0.84}}$ MQWs for a range of lattice temperatures. Analyzed results reveal contributions from the transitions from the various hole states to the electronic resonance in the InAs well. The most striking result is a strong plateau observed in the transient absorption for low excitation densities, sufficient excess-photon energy, and low-to-moderate lattice temperatures.

Figure 5.3(a) shows a schematic of the optical pump and THz probe spectroscopy performed on an InAs/$\mathrm{AlAs_{0.16}Sb_{0.84}}$ MQW. More details of this technique were discussed in chapter 2. As a reminder, the tuning range is 1200 nm (1.03 eV) to 1600 nm (0.775 eV). Throughout the tuning range, the excitation density in the MQW is kept constant at $\sim 10^{13}$ cm^{-2}.

Figure 5.3(b) shows two examples of transient differential THz electric field $[\Delta E(t)/E]$ transmitted through the MQW sample which is cooled to 4 K and excited with 0.85 eV and 0.97 eV pump photon energies. The transients exhibit a fast rise with a multi-exponential decay that persists for over a nanosecond. The maximum amplitude of the transients increases with increasing pump photon energy, and a plateau, lasting a few picoseconds in

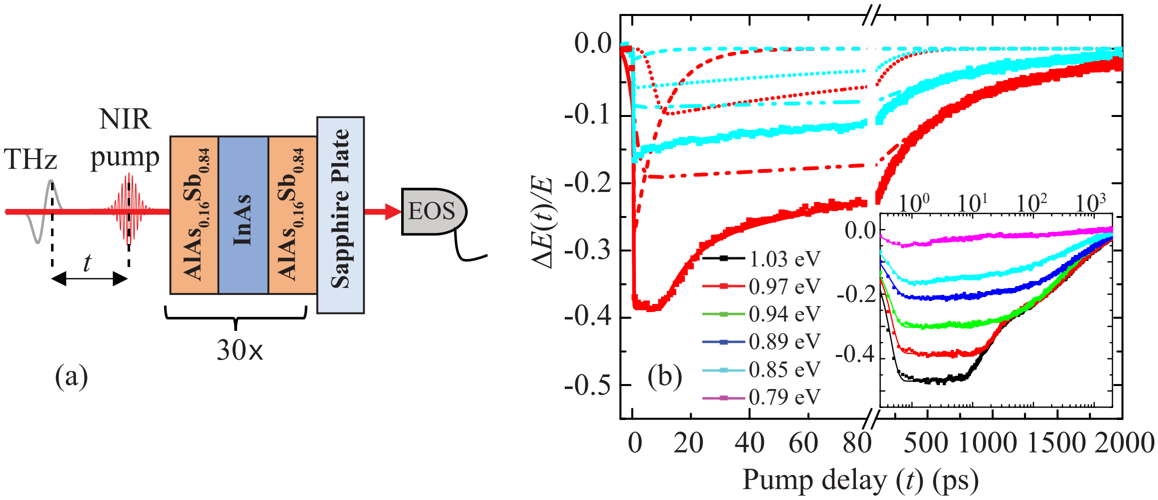

Figure 5.3: (a) Schematic of the optical pump THz probe experiment geometry. EOS = electro-optic sampling. (b) Transient differential THz-electric field $[\Delta E(t)/E]$ through the MQW sample at 4 K for the excitation photon energies of 0.85 eV (cyan) and 0.97 eV (red). Multi-exponential fits are shown as solid lines, comprised of a fast (dash line), intermediate (dotted line), and slow (dash dot-dot line) component. The insets show a semi-log plot of the transient data and respective fits in the range 0.79 – 1.03 eV. Figure modified from Piyathilaka *et al.* [142].

duration, emerges in the higher pump photon energy transients. This plateau is more clearly visible in the inset of the figure, where the pump-probe delay time is plotted on a semi-logarithmic scale, and data are shown for the excitation range of 0.79 eV to 1.03 eV. This excitation range corresponds to an excess-photon energy range of -50 meV$<\Delta<$175 meV ($\Delta(T) = E_{pump} - E_g(T)$) at 4 K and blue shifts with increasing temperature. Transients are also recorded for 100 K, 200 K, and 300 K.

To capture the plateau, the transients are fit to a three-component solution to the canonical rate equation

$$\frac{\Delta E(\Delta t)}{E} = \sum_{i=1}^{3} \frac{A_i}{2} \left[1 + \mathrm{erf}\left[-\frac{(t-t_0)}{\tau_{Ri}}\right]\right] \exp\left[-\frac{(t-t_0)}{\tau_{Di}}\right], \tag{5.16}$$

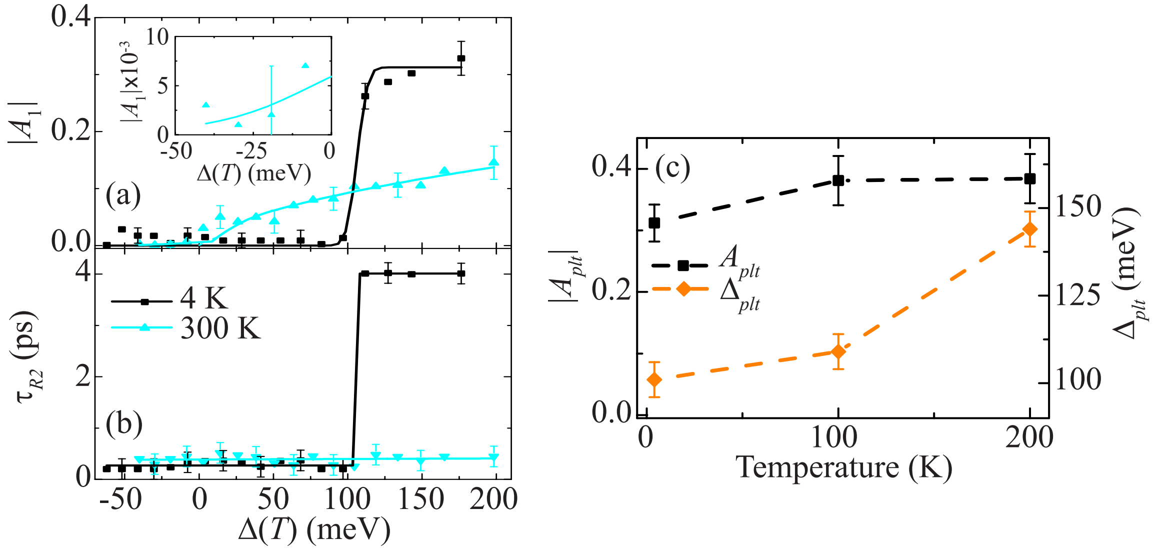

Figure 5.4: Excess-photon energy dependent of (a) $|A_1|$ and (b) τ_{R2} from the fitted transients for 4 K and 300 K, revealing a plateau in the former. The inset in (a) shows the below bandgap response of A1(300 K). (c) Temperature dependence (up to 200 K) of the on magnitudes for fast decay mechanism black square ($|A_{plt}|$) for step function and orange diamond for energy onset of the plateau. Figure modified from Piyathilaka *et al.* [142].

where $\Delta t = t - t_0$, and A$_i$, τ_{Ri}, and τ_{Di} are amplitude, rise time and decay time for the ith component respectively. For best fitting, the first rise component (τ_{R1}) is chosen to be the cross-correlation of the pump and probe pulses, rounded to $\sim$ 200 fs. The second and third rise components (τ_{R2} and $\tau_{R3} = \tau_{R2}$) are free parameters to best fit the plateau region at early delay times in the transients. The various parameters extracted from the fits are plotted in the next few figures along with temperature- and energy-dependent analysis.

Figure 5.4(a) and (b) show the extracted magnitude ($|A_1|$) and rise time (τ_{R2}), as a function of $\Delta(T)$ for T = 4 K and 300 K. At 4 K, both $|A_1|$ and the τ_{R2} are correlated, exhibiting a transition at $\Delta_{plt} \approx 100$ meV. Δ_{plt} corresponds to the onset of the plateau in the transients and is best understood by comparing the constituent transients in Figure 5.3(b). For 0.85 eV excitation ($< \Delta_{plt}$), $|A_1|$ is small (exhibiting a weak free-carrier absorption signal) and $\tau_{R2} \approx \tau_{R1}$, indicating excitation into long-lived states that are responsible for strong PL [150]. By contrast for 0.97 eV excitation ($> \Delta_{plt}$), $|A_1|$ is significant, exhibiting both a fast rise and decay. The fast decay is simultaneous with a slow rise of the longer-lived states, indicating a subband transfer of charge carriers.

The magnitude of the metastable plateau is modeled as

$$|A_1(\Delta, T)| = A_{plt}(T) \left(\frac{1}{2} \operatorname{erfc} \left\{ -\frac{[\Delta - \Delta_{plt}(T)]}{w} \right\} \right), \tag{5.17}$$

where $A_{plt}(T)$ is the temperature-dependent amplitude of the plateau contribution and w is the transition width (limited by the spacing of the tuning of the laser's center photon energy). A similar expression can be determined for τ_{R2} with an addition of a τ_{R1}-like term below $\Delta_{plt}(T)$. Figure 5.4(c) shows that $A_{plt}(T)$ increases up to $T = 200$ K as the band structure contracts and the density of states at each energy interval increases. Figure 5.4(c) shows that Δ_{plt} also increases up to 200 K, most likely due to thermal-expansion-induced strain (resulting from the sample being adhered to the sapphire substrate that modifies the band positions with respect to one another [182]).

In contrast to the 4 K data, at 300 K, the Δ-dependence of $|A_1|$ does not show the plateau behavior. Instead, $|A_1(\Delta)|$ comprises a weak exponential growth for $\Delta < 0$ [see inset of Figure 5.4(a)] and a saturating power-law growth for $\Delta > 0$. This behavior is also seen for the magnitudes of the two slower decay components $|A_{2,3}|$; see Figure 5.5(a) and (b). Above E_g, the magnitude is indicative of the interband absorption and $\propto |A_{(i,q)}|\Delta^q$, where q is determined by the density of states [183]. [Namely, $q = 0$ for localized states, $q = 0.5$ for purely direct-gap transitions in bulk, $q = 1$ for transitions in an infinite quantum well, and $q = 2$ for purely indirect transitions in bulk.] Figure 5.5(c) shows that $q \approx 0.5$ at low temperature for all three constituents of the transient, indicating that the absorption is direct and bulk-like, which is unsurprising for the 30-periods InAs/AlAs$_{0.16}$Sb$_{0.84}$ MQW with a fairly large penetration depth of the wavefunctions into the barriers and with alloy-

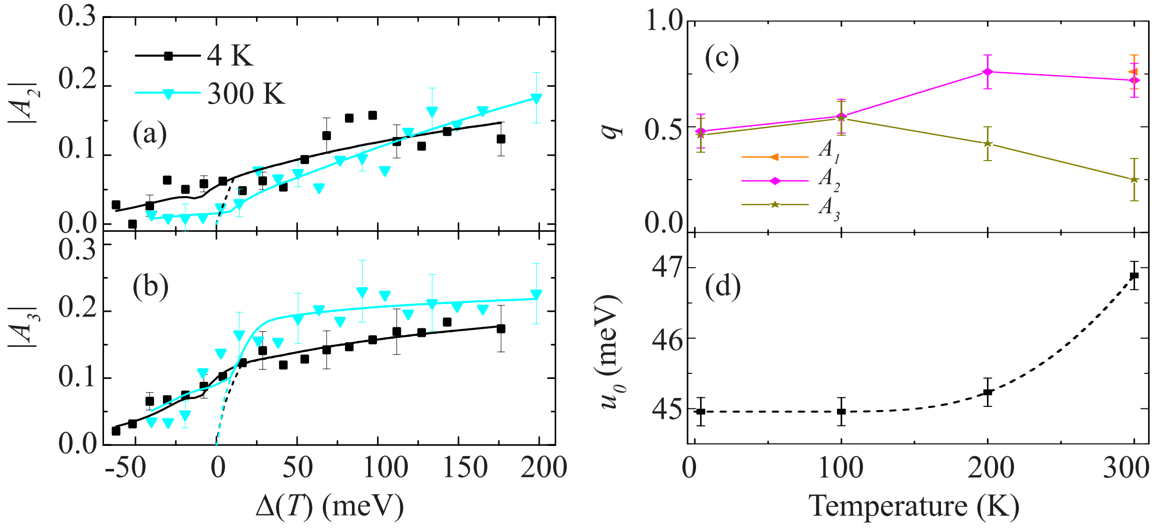

Figure 5.5: Excess-photon energy dependence of (a) $|A_2|$ and (b) $|A_3|$ at low and high lattice temperatures. Temperature dependence of (c) power value, q, to determine the band-to-band excitation transition type and (d) Urbach energy, u_0, for below-gap absorption contributions. Figure modified from Piyathilaka *et al.* [142].

intermixing states at the good interface [184]. As temperature increases, the fast and intermediate components increase by about 40% (and overlaps with the q value extracted from $|A_1|$ when the plateau vanishes at room temperature), while q decreases by about 50% for the slow component. A weighted sum may be able to determine the fraction of direct, indirect, allowed, and forbidden transition contributions [185].

Below E_g, the magnitude of the transients shows an absorption tail $\propto |A_{(i,u)}| \exp(\Delta/u_0)$, where the Urbach energy (u_0) characterizes the extent of the below-gap absorption tail due to structural and thermal disorder [186]. Figure 5.5(d) shows the temperature dependence of the Urbach energy exhibited in all transient components. At low temperature, $u_0 \approx 45$ meV and it increased by $\sim 4\%$ at 300 K. Lattice vibrations and dynamic structural disorder both effect $u_0(T)$ [187]. The former only increases $u_0(T)$ as a function of T due to a growing phonon distribution [188], whereas dynamic structural disorder can reduce $u_0(T)$ and has been related to the onset of medium-range order, typically in amorphous materials. For the high-quality MQW sample, the lattice vibration contribution to $u_0(T)$ must dominate. This is supported by the analysis of Urbach energy using the Einstein model

$$u_0(T) = \frac{k_B\Theta}{\sigma_0}\left[\frac{1+X}{2} + \frac{1}{\exp(\Theta/T)-1}\right], \tag{5.18}$$

where X is a dimensionless parameter related to structural disorders, $1/\sigma_0$ is a dimensionless constant related to electron-phonon coupling and Θ is the Einstein temperature (which is $\sim \frac{3}{4}$ of the Debye temperature). Here, $X = 4.29 \times 10^{-3}$, approaching the value for a perfect crystal ($X = 0$) [189], due to very mild disorders [159–161]. Although not the central focus of this chapter, it would be possible to add a disorder potential to band structure calculations in order to simulate the extracted Urbach parameter at low temperature.

The long-lived components of the decay transients are responsible for the strong PL and their decay times appear to be somewhat unaffected by the pump photon energy. For 4 K and averaged over the pump detuning, $\tau_{D2} = 0.16$ ns and $\tau_{D3} = 0.91$ ns; see inset of Figure 5.6(a). Both of these values increase with increasing temperature, which is associated with the increase of the phonon distribution and the expected phonon-induced stabilization of the hot carriers (discussed in the Chapter 4) [50].

Decay mechanisms can be determined by recapturing the rate-equation by inverting the transient and converting it into $\partial[n,p]/\partial t$ versus $[n,p]$ by use of the linear absorption coefficient for excitation pulse. In this case, n and p are the photoexcited electron and hole populations [190] and the slope indicates the decay mechanism. Figure 5.6(a) shows the rate equation for 1.03 eV excitation ($\Delta > \Delta_{plt}$) at 4 K and 300 K on a logarithmic scale. Overlaid are guides to the eye demarcating the $[n,p]^m/\tau$ slopes with τ as the instantaneous decay time. In this analysis, $m = 1$ corresponds to SRH dynamics, which involve recombination of electrons or holes with defect state (hence, $\sim n/\tau$ or $\sim p/\tau$); $m = 2$ corresponds to interband radiative recombination ($\sim np/\tau$) or trap-assisted Auger scattering, where SRH

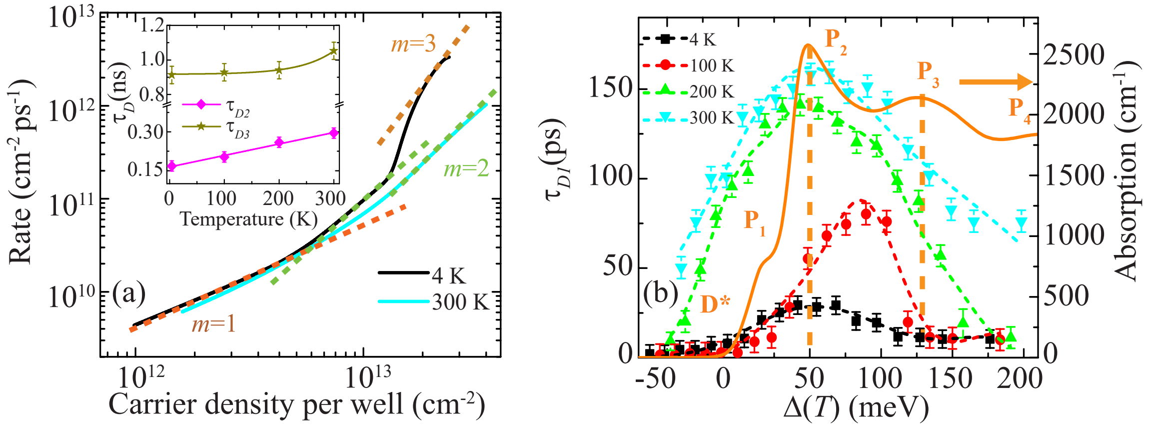

Figure 5.6: (a) Relaxation and/or recombination rate of excited-state carriers for 1.03-eV excitation at 4 K (black) and 300 K (cyan). Dashed guides to the eye represent known recombination mechanisms. Inset: temperature dependence of decay times τ_{D2} and τ_{D3}, averaged over excess-photon energy. (b) Excess-photon energy dependence of fast decay time (τ_{D1}) fit with five Gaussian distributions centered at D* and P$_1$-P$_4$ (dashed lines). The latter is determined from the simulated optical absorption (solid line). Figure modified from Piyathilaka *et al.* [142].

.

recombination results in scattering of a carrier of the same species ($\sim n^2/\tau$ or $\sim p^2/\tau$); and $m = 3$ corresponds to Auger scattering, where interband recombination results in scattering of a carrier ($\sim n^2p/\tau$ or $\sim np^2/\tau$) [191–193].

For 4 K, the slope indicates the dominance of Auger recombination at high carrier concentration as might be expected in a high-confinement nanostructure. This corresponds to the plateau region at the beginning of the transient. Auger recombination gives way to trap-assisted Auger or radiative recombination and finally SRH dynamics as the carrier concentration continually decreases. In contrast, 300 K data does not show the initial Auger scattering, $m = 2$ processes persist to much higher carrier concentrations and the trend is otherwise similar to the low-temperature results at lower carrier concentrations.

Table 5.1: Rate constant for 1.03 eV pump excitation (Linear (α), quadratic (β), and cubic (γ)).

T (K)	α (ps^{-1})	β (cm^{-2}ps^{-1})	γ (cm^{-4}ps^{-1})
4	4.68×10^{-3}	9.75×10^{-16}	4.8×10^{-29}
300	4.45×10^{-3}	5.96×10^{-16}	–

The temperature behavior is consistent with PL results [150] only if (i) Auger-scattering during the plateau region leads to a persistence of hot carriers followed by a strong burst of radiative emission as the carrier concentration decays and (ii) radiative recombination dominates over trap-assisted Auger when excitation does not lead to the plateau behavior. For this Δ, conversion from dynamics that include the plateau response at low temperature to dynamics without it at near-room temperature is likely related to the higher-temperature delocalization of the valence bands throughout the MQW structure [150].

The high carrier-excitation regime varies significantly with temperature; therefore, it is reasonable to expect that – unlike the long-lived decay times – τ_{D1} exhibits a strong dependence on both Δ and T; see Figure 5.6(b). Data are fitted with five Gaussian distributions, each with a center position that corresponds to either the defects D* (below E_g) or P$_1$ through P$_4$ and with widths that are commensurate with the Urbach tailor, the width of the calculated optical absorption also shown in the figure [151]. At low temperature, τ_{D1} increases from just below E_g to a maximum at the P$_2$ energy identified in the absorption calculations and decreases above that energy. At 100 K, the maximum of τ_{D1} shifts between P$_2$ and P$_3$ and is about three times slower. Excitations at the band edge (P$_1$) now have a faster decay, while excitation at or above P$_2$ are stabilized by phonons and the Auger recombination process. This result clearly indicates that the various hole states indeed have different decay times. At 200 K, the MQW band alignment is known to be type-II and τ_{D1} is radically increased across the entire pump detuning range, exhibiting slower decays from defect contributions below P_1 and ever slower decays from the states above. This behavior is similar for 300 K with a further slowing at the higher range of Δ where it is presumed the increased phonon distribution better stabilizes the hot carriers. For all temperatures, large τ_{D1} values are limited at upper energy of P_3 which corresponds well with $\Delta_{plt}(T)$ determined from the amplitude analysis. Above this upper energy limit, all excitations are fast and result in transitions to the longer-lived states. Only the data for 300 K show a significant τ_{D1} above P_3, where the P_4 resonance also contributes to slowing the initial decay.

The energy and temperature dependence of the charge-carrier dynamics in the InAs/Al $As_{0.16}Sb_{0.84}$ MQW are complicated due to the multiple hole subbands, the unusual interaction with phonons, the changing of the localization of the holes with temperature, and the possible interaction with moderate numbers of defects that give a non-zero contribution to the dynamics below the bandgap. Analysis of the dynamics encourage several questions, the most prominent being *what is the origin of the metastability at early times and the resulting plateau seen in various components of the deconvolved transients?*

Defects associated with the alloy fluctuations have mean binding energy of ~ 25 meV [150], which is four or five times smaller than Δ_{plt} extracted from Figure 5.4(c). Hence, alloy fluctuations are excluded from consideration as the origin of the metastability. Nonetheless, these defects play a role directly in short-time dynamics when the excitation is below the bandgap or through long-timescale recombination dynamics, such as trap-assisted Auger and SRH mechanisms, when exciting above the bandgap.

One possible origin is the excitation at $k \neq 0$ states, where due to valence-band mixing there are saddle points and even local minimum in hh3 such that the dispersion can slow the relaxation of the holes and limit recombination with e1 electrons. In the simulations, the exact energy of the local minima is more error-prone than the determination of $k \neq 0$ states. Reasonably errors of $\sim 10 - 20$ meV provide a sufficient margin to suppose that optical excitation from hh3 →e1 occurs at $\Delta \approx 100$ meV at low temperature and slightly more at elevated temperatures. If this argument is upheld, it may also explain why there are so many components observed in the transients, since the signal would be dominated by the hole bands, both in terms of the response to excitation and in terms of the mechanisms of decay. For example, it is clear that the metastable state at early times does eventually relax into long-lived states where stable hot carriers persist through the inhibited electron-phonon interaction. This is consistent with increasing temperature delocalizing the hole wavefunctions and allowing this metastability to no longer play a role in the dynamics.

Alternatively, even though the onset of the plateau occurs several 100's of meV below the excitation energy required to expect easy intervalley scattering to the L-valley [32, 42, 153, 179, 194], the electric field of the THz probe is approximately double the required field to result in a Gunn effect in these samples ~17 kV/cm [153].

However, if hot electrons persist and are even heated through electron-phonon interactions after their initial excitation, some degree of band tilting due to the THz field may scatter e1 electrons into the L-valley [39] to contribute to the complicated transient response. This effect does not quite match with the initial experiments performed for a range of probe electric field strengths (straddling ~ 17 kV/cm), where it might be expected that at lower field strengths the sharp edge of the plateau in $|A_1|(\Delta)$ may soften or the plateau may even vanish. To test this hypothesis, transient absorption data were collected as a function of THz probe intensity at 4 K. The pump energy is chosen to be at the onset of the plateau [refer Figure 5.7; Change of the amplitude in (a) is attributed to the fluctuations of pump intensity]. The data are fitted with the multi-exponential rate equation (equation 5.16). According to the analysis, even at a probe field strength of ~ 8 kV/cm, the onset of the

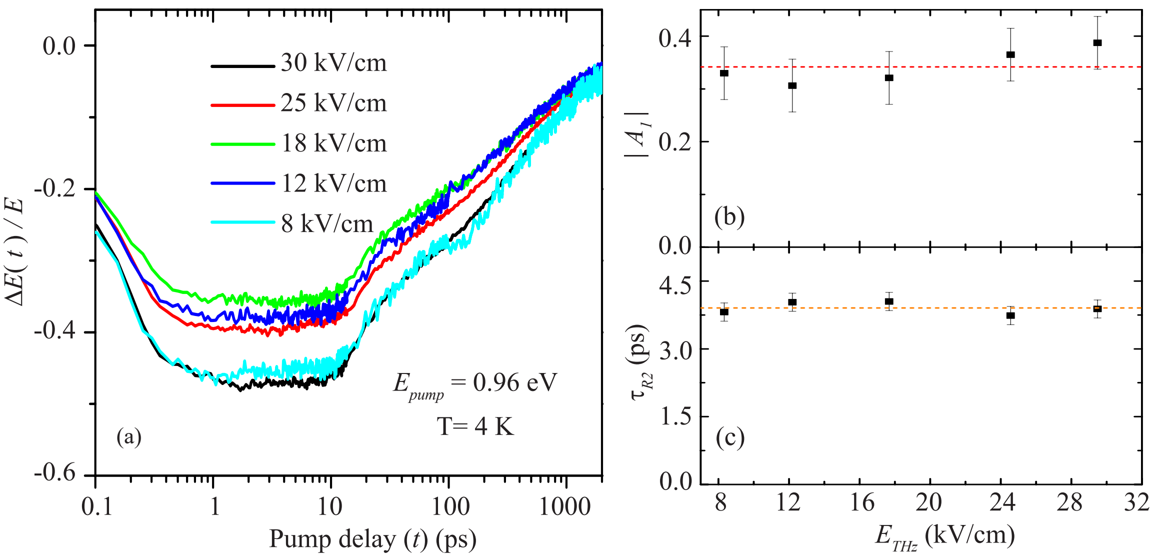

Figure 5.7: (a) THz electric field dependent transient absorption of the MQW sample at 4 K for the excitation photon energies of 0.96 eV. THz electric field dependent of (b) $|A_1|$ and (c) τ_{R2} from the fitted transients.

plateau is still sharp and unmodified [Figure 5.7 (b) and (c)].

A final and less likely alternative is the trapping of charge carriers in defect states. Despite the high-quality epitaxial growth InAs/AlAsSb quantum wells are known to have the disorder [160, 195, 196] – as evidenced by the Urbach tail. There are a host of potential unintentional defects that may trap the carriers, but without testing the specific sample with electron paramagnetic resonance spectroscopy it would be hard to identify a particular defect that may be expected to result in long-lived carrier trapping.

Based on this discussion, Figure 5.8 summarizes the nonequilibrium dynamics of photoexcited electrons and holes in the MQWs. For excess photon energies below the onset of the metastable plateau in the dynamics ($\Delta < \Delta_{plt}$), the excitation amplitude shows a mostly square-root dependence as a function of Δ. This is indicative of exciting direct transitions hh1-e1, lh1-e1, and hh2-e1, with carriers promoted symmetrically into the parabolic band at in-plane wavevector $k_\perp > 0$. Carriers then undergo charge separation into type-II-aligned

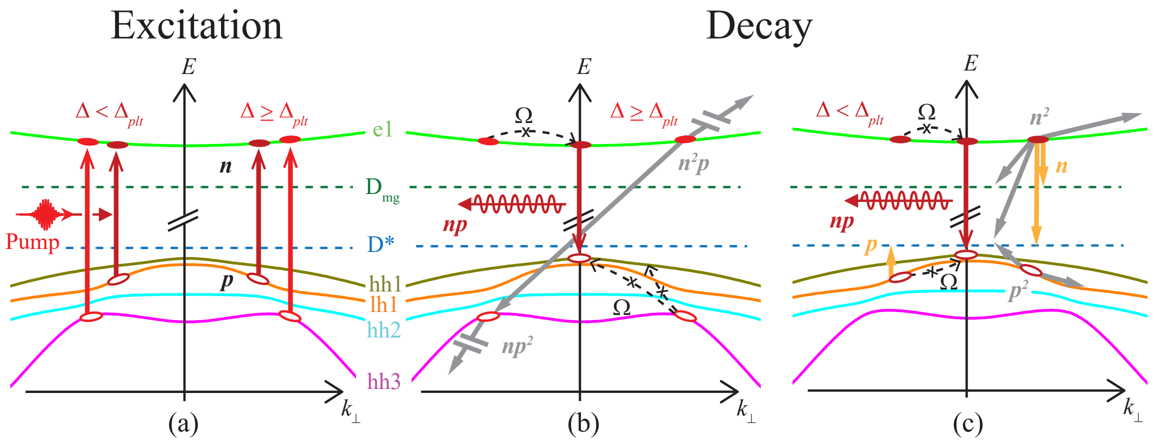

Figure 5.8: (a) Interband Excitation by the optical pump creates holes (p) and electron (n) in the valence and conduction bands [151] at non-zero in-plane wavevectors. (b) Excitation with pulse detuning at $\Delta \geq \Delta_{plt}$ results in decay by Auger-scattering [$\propto n^2p, np^2$], followed by intraband relaxation via phonon emission [Ω], then (c) trap-assisted Auger [$\propto n^2, p^2$] and radiative recombination [$\propto np$] and finally by Shockley-Read-Hall dynamics [$\propto n, p$]. Excitation with $\Delta < \Delta_{plt}$ results in decay only through the stages outlined in (c). Figure modified from Piyathilaka *et al.* [142]

wells and barriers, trap-assisted Auger scattering ($\propto n^2, p^2$) with InAs interface traps [150, 197, 198], radiative recombination (np) responsible for PL [150] and SRH non-radiative recombination ($\propto n, p$) with interface and mid-gap states [150]. Weak electron-phonon coupling and phonon-phonon scattering [167] slows carrier thermalization and intraband relaxation, instead stabilizing the hot carriers and resulting in prolonged decay times. In addition, for $\Delta > \Delta_{plt}$ at temperatures $\geq$ 200 K, hh3-e1 transitions are symmetrically excited at $k_\perp > 0$, where local minima in the hh3 states are suspected to further stabilize the holes and even reduce charge separation by reducing wavefunction overlap. During the plateau regime, scattering to $k = 0$ states is further reduced and conventional Auger scattering ($\propto n^2p, np^2$) occurs pushing carriers deep into their respective bands. In InAs, Auger scattering is dominant for holes [191–193]. Slowly, the carrier density decreases via intra-valence band scattering and the dynamics revert to that seen for excitation $\Delta > \Delta_{plt}$.

5.4.2 Intensity dependence of hot-carrier relaxation

The InAs/AlAsSb MQW structure was photoexcited by 1.03 eV pump energy for a series of pump intensities at selected lattice temperatures of 4 K, 100 K, 200 K, and 300 K. Figur 5.9 shows the differential transients at 4 K for a range of pump intensities. The transients consist of a fast rise with multiple exponential decays. The amplitudes of transients increase with increasing pump intensity and exhibit metastability of nonequilibrium carriers above ∼ 5 GW/cm^2 pump intensities. The metastability was previously investigated for a series of photoexcitation energies.

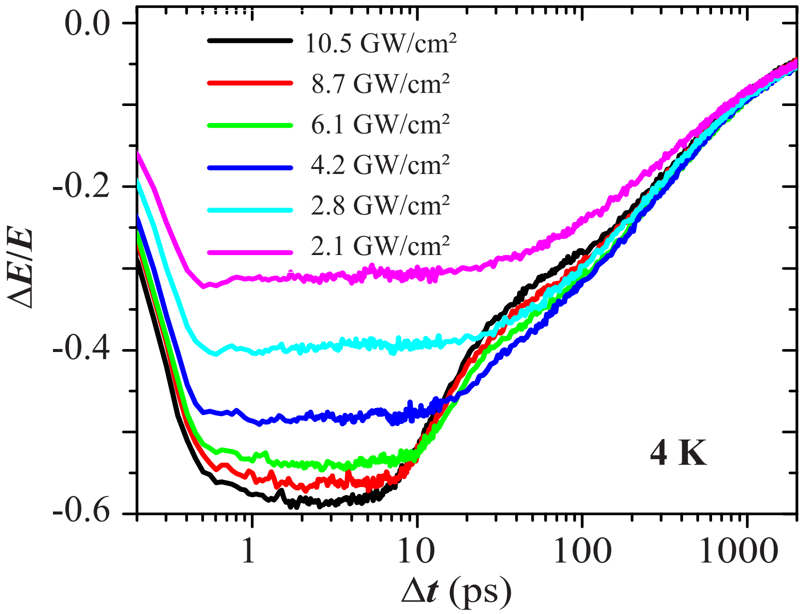

Figure 5.9: Differential transient for a range of pump intensities with photon energy of 1.03 eV and the lattice temperature of 4 K.

Photoexcited carrier dynamics are modeled by fitting the transients with a solution to the rate equation (equation 5.16). When the transients exhibit metastability, A_1 and τ_{R2} shows a step, where this can be described by

$$A_1(T) = A_{10}(T) + \frac{1}{2}A_{11}(T)\,\mathrm{erfc}\left(-\frac{I - I_0(T)}{w}\right), \tag{5.19}$$

$A_{11}(T)$ is the temperature-dependent amplitude that contributes to the plateau, and w is the transition width of the step function. $I_0(T)$ is the pump intensity where the metastability is visible in the transient. $A_{10}(T) = A_0[1 - \exp(-\alpha I)]$ for the intensities below the plateau in the transient and for higher lattice temperatures where transients do not exhibit a step. To model τ_{R2}, the same procedure was followed, and at lower pump intensities and higher lattice temperatures, τ_{R2} becomes $\tau_{R1} \approx 200$ fs. The fitting allows for the identification of the metastable regime and qualifies the expected decay rates. It also demonstrates how metastability dominates the transient response under appropriate excitation conditions. Finally, the results show that the excitation saturates at high lattice temperatures.

Converting the transient into the rate-equation allows for determination of the relaxation rate and decay mechanisms when plotting rate $(\partial N_{exc}(N_{exc})/\partial t)$ [142, 190, 199, 200]. Figures 5.10 shows the (c,d) rate versus carrier concentration and (e,f) carrier lifetime versus carrier concentration for pump intensities of ≈ 4.2 GW/cm^2 and ≈ 6.1 GW/cm^2 and lattice temperatures of (c,e) 4 K and (d,f) 300 K. The pump intensities were chosen to straddle the onset of the metastable regime due to excitation density at low temperature. Guides to the eye represent the carrier recombination mechanism. In green, $m = 1$ represents the SHR mechanism (n/τ or p/τ) where recombination occurs through impurity levels [Dmg or D* in Figure 5.8] and dominate the low excitation density regime. In orange, $m = 2$ represents radiative recombination (np/τ) or trap-assisted Auger recombination (n^2/τ or p^2/τ), typically dominating the middle range of excitation densities. In red, $m = 3$ represents the Auger recombination mechanism (n^2p/τ or np^2/τ) typically occurring

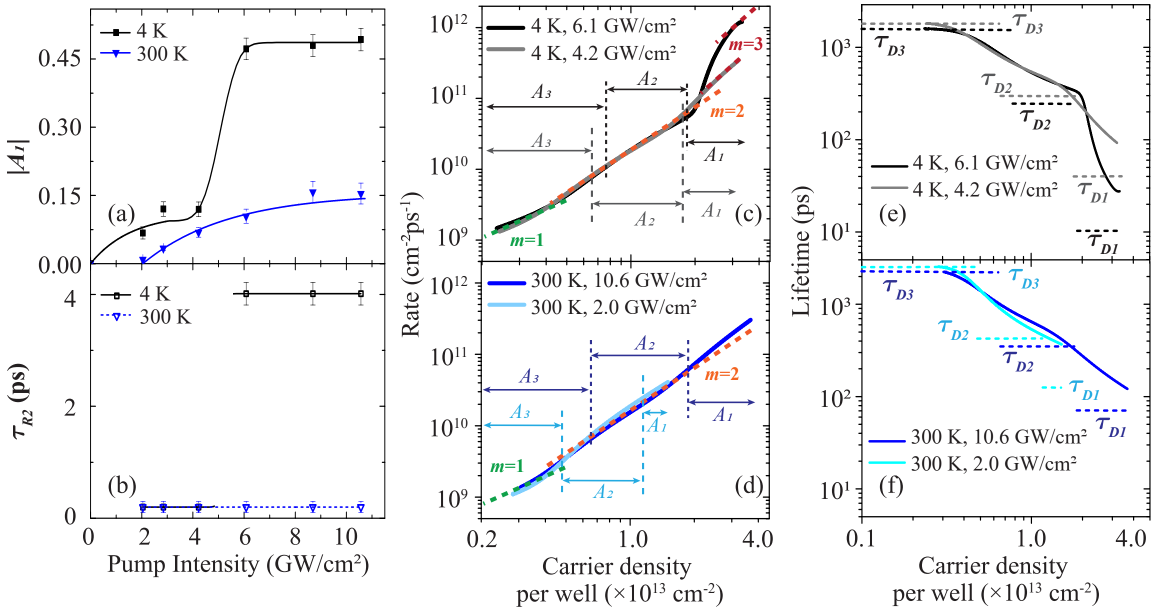

Figure 5.10: Intensity dependence of (a) A_1 and (b) τ_{R2} of the multi-exponential rate equation. Recombination rate of photo-excited carriers at 1.03 eV pump excitation for selected pump intensities at (c) 4 K and (d) 300 K lattice temperatures. Dashed lines (red, orange, and green) represent the relaxation mechanisms, and the region separated by black and gray dashed lines represents the amplitudes of the multi-exponential fitting. Nonequilibrium carrier lifetimes at (e) 4 K and (f) 300 K lattice temperatures. Dashed lines represent the carrier density range for extracted carrier decay times from multi-exponential fitting.

at higher excitation densities.

From this analysis, it is clear that the higher-order relaxation mechanisms are directly related to the step behavior of A_1, which was hypothesized in the previous studies. Overlaid on Figures 5.10 (b) and (c) are the ranges of A_1, A_2, and A_3 for comparison. It is can be seen that the general overlap allows for an understanding of which mechanism should correspond to which exponential decay component. For high intensities and low lattice temperatures,

Table 5.2: Cubic rate constant (γ) for 1.03 eV pump excitation at 4 K lattice temperature.

Pump intensity (GW/cm^2)	γ (cm^{-4}ps^{-1})
4.2	1.08×10^{-29}
6.1	4.57×10^{-29}

the initial response of the system is dominated by Auger recombination, which scatters excited carriers deeper into their respective bands and allows them to experience slower recombination rates through the lower-order mechanisms.

Auger scattering still occurs for the lower intensity plot in Figure 5.10 (b) but at a lower rate, most likely because the excitation density requires such quick scattering of carriers and dissipation of energy. By contrast, the Auger-scattering mechanism is suppressed at high temperatures regardless of excitation intensity. The dominant decay mechanisms are either radiative recombination or trap-assisted Auger scattering. Given the reasonably strong PL at high temperatures in this sample [150], it is most likely that the former mechanism dominates.

Figures 5.10 (e) and (f) show the inverting decay rates, namely the instantaneous carrier lifetime as a function of excitation density. For comparison to the more comprehensive analysis of instantaneous lifetimes, the average values of τ_{D1}, τ_{D2}, and τ_{D3} are overlaid, showing that they generally agree especially for the lower-order decay mechanisms. The deviation for the higher-order illustrates the problem with the multiple-exponential decay and in this case, τ_{D1} values include the rise τ_{R2} – used to model the metastability – that further distorts the simple analysis. The inversion analysis allows direct read-off of the carrier lifetime as a function of excitation density.

5.5 Chapter Summary

Hot-carrier dynamics were investigated using TRTS with respect to the temperature, excitation pump energy, and excitation pump intensity. The excited metastable carriers can be observed when the excess photon energy exceeds ∼100 meV at sufficiently low lattice temperature. This metastability most likely corresponds to local minima in the non-zero in-plane wavevector states of the hh3 band and leads to an accumulation of carriers that have a slow intra-valence cooling. The dynamics of the metastable states are dominated by Auger scattering that can potentially increase hot carrier extraction, assuming that extraction can be achieved faster than the cooling. Once intra-valence band scattering occurs the electron and hole recombination rates are typically slow due to charge-carrier separation in the MQW structure and a slow cooling mechanism due to phonon-phonon coupling limits and a thermal conductivity mismatch in the structure.

As a function of pump intensity, metastability of the excited carriers vanishes with the reduction of pump intensity. And it confirms that the Auger scattering exhibited at higher excitation densities and lower temperatures dominate in the metastable regime. Moreover, when the pump intensity is increased, the Auger scattering rate increases to mitigate the build-up of carriers. This lowers the carrier concentration and allows for slower recombination rates to dominate the hot-carrier dynamics.

Chapter 6:

Non-equilibrium (photoexcited) state hot-carrier transport

6.1 Introduction

In HCSC, the hot carriers must be extracted using energy-selective contacts before the emission of optical phonons, which eventually convert into acoustic phonons. This is crucial because the MQW structure used here exhibits a phonon bottleneck [50] that inhibits this cooling. In order to do this, carriers must be transport themselves to the contacts. Therefore, exploring the carrier transport mechanisms gives insight into the development of hot carrier extraction.

The development of MQW structures using III-V semiconductors received significant attention because it allows the control of the position of valance and conduction bands as well as the purity of the superlattice [151]. Previous chapters discuss the hot-carrier dynamics in the InAs/AlAsSb type-II MQW structure [50, 142] shows a long-excited level carrier lifetime in addition to the meta-stability at early exciting times for 100 meV above the bandgap excitation [142]. The spatial separation of electrons and holes and the inhibit phonon-phonon interactions contribute to the long carrier lifetime, while complex valance band states with local minima's contribute to the system's meta-stability. Therefore, investigation of transport mechanisms in excited-state hot-carriers facilitates the researchers to explore energy selective carrier extraction methods for HCSC consisting of MQWs.

In this chapter, THz AC-photoconductivity measurements are performed on InAs/Al

As$_{0.16}$Sb$_{0.84}$ MQW structures for a range of lattice temperatures and optical excitation conditions. This technique will facilitate investigating the MQW system's carrier transport when the system is at metastable and non-metastable states.

6.2 Excited-state conductivity

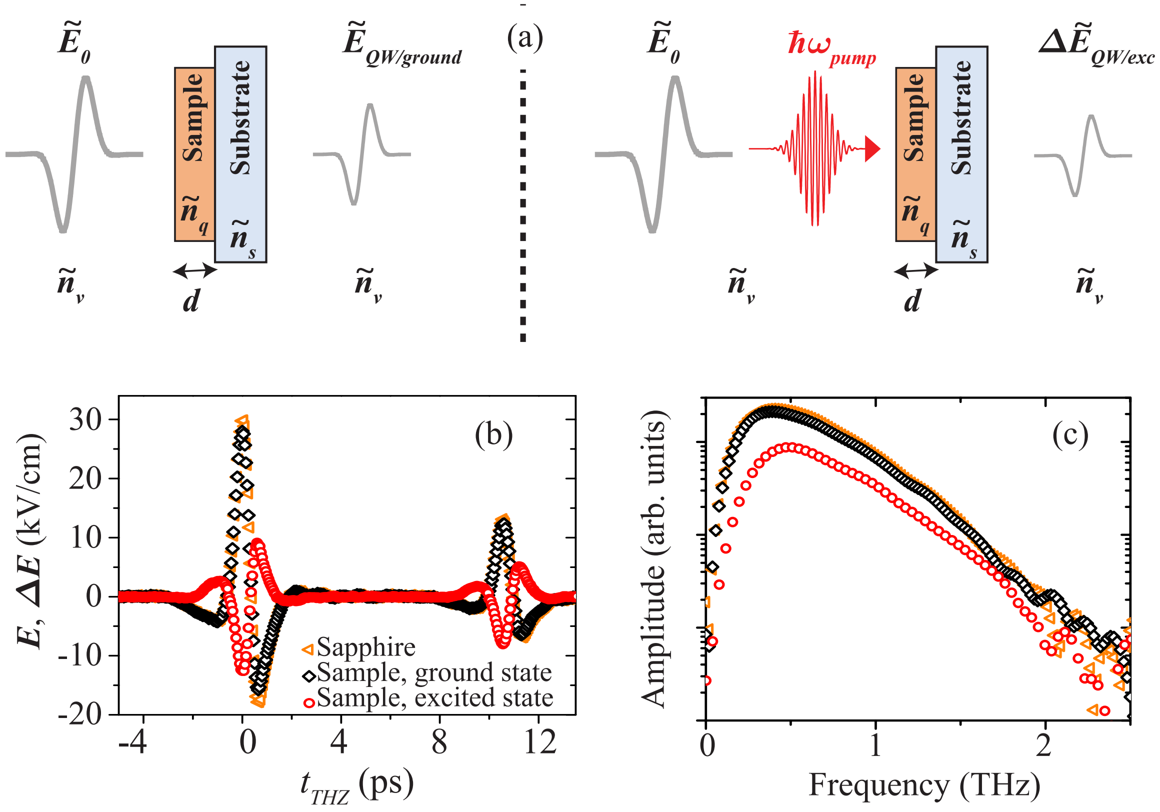

Figure 6.1: (a) Schematic of THz transmission through the photoexcited MQW sample. (b) Transient of THz transmission through the sapphire substrate and InAs/AlAs$_{0.16}$Sb$_{0.84}$ MQW sample with photo-excitation. (c) Associated amplitude spectra resulting from a numerical Fourier transform.

Compared to THz-TDS, which is sensitive to equilibrium charge carriers, TRTS measures the photoinduced conductivity ($\Delta\tilde{\sigma}_q(\omega)$) of the system. As discussed in section 2.3, the optical pump excites carriers into the conduction band, and the THz pulse probes the excited charge carriers. The THz transmission through the sample is diminished because of the photoconductivity due to excited charge carriers. The change in transmission of THz due to photoexcitation can be calculated using

$$\frac{\Delta\tilde{T}(\omega)}{\tilde{T}(\omega)} = \frac{\Delta\tilde{E}_{QW/exc}(\omega)}{\tilde{E}_{QW/ground}(\omega)}, \tag{6.1}$$

where $\tilde{E}_{QW/ground}$ and $\Delta\tilde{E}_{QW/exc}(\omega)$ are FFT of ground-state THz transmission and excited-state THz transmission signal [see Figure 6.1(a)].

The induced photoconductivity $\Delta\tilde{\sigma}_q(\omega)$ is directly proportional to the differential transmission $\Delta\tilde{T}(\omega)/\tilde{T}(\omega)$. Considering the THz wave propagation through the sample with and without photoexcitation, $\Delta\tilde{T}(\omega)/\tilde{T}(\omega)$ can be described as

$$\frac{\Delta\tilde{T}(\omega)}{\tilde{T}(\omega)} = \frac{\left(\tilde{n}_v + \tilde{n}_q^*\right)\left(\tilde{n}_q^* + \tilde{n}_s\right)}{\left(\tilde{n}_v + \tilde{n}_q\right)\left(\tilde{n}_q + \tilde{n}_s\right)} \exp\left(\frac{i\omega d}{c}\left(\tilde{n}_q^* - \tilde{n}_q\right)\right)\frac{FP_{vqs}^* FP_{qsv}^*}{FP_{vqs}FP_{qsv}} - 1, \tag{6.2}$$

where $\tilde{n}_v, \tilde{n}_s, \tilde{n}_q, c, d$ and FP_{ijk} are defined previously (equation 3.3), and subscript * represents the values when the sample is at photoexcitation. Considering the thin film limit ($d \ll \lambda, P \to \infty$) and substrate being very thick ($d_s > \lambda, P = 0$) the equation 6.2 can be simplified as

$$\frac{\Delta\tilde{T}(\omega)}{\tilde{T}(\omega)} = \frac{i\omega d}{c}\frac{\left(\tilde{n}_q^{*2} - \tilde{n}_q^2\right)}{(1+\tilde{n}_s)}, \tag{6.3}$$

$$\tilde{n}_q^{*2} - \tilde{n}_q^2 = -\frac{ic(1+\tilde{n}_s)}{\omega d}\frac{\Delta\tilde{T}(\omega)}{\tilde{T}(\omega)}. \tag{6.4}$$

Then the complex photoconductivity can be calculated considering the photoinduced complex dielectric function.

$$\tilde{n}_q^{*2} - \tilde{n}_q^2 = \epsilon_q^* - \epsilon_q, \tag{6.5}$$

$$\epsilon_q^* - \epsilon_q = \frac{i\Delta\tilde{\sigma}_q}{\omega\epsilon_0}, \tag{6.6}$$

$$\Delta\tilde{\sigma}_q(\omega) = -\frac{\epsilon_0 c(1+\tilde{n}_s)}{d}\frac{\Delta\tilde{T}(\omega)}{\tilde{T}(\omega)}. \tag{6.7}$$

In above equation $\Delta\tilde{\sigma}_q(\omega)$ is the photoconductivity of the MQW sample.

6.2.1 Conductivity models: AC-photoconductivity

To analyze photoconductivity, suitable conductivity models have to be employed. The most commonly used models are the Drude-Lorentz and Drude-Smith models, which were discussed earlier. Apart from those conductivity models, the Hopping model and Plasmon model can be used to analyze the photoconductivity for this MQW system.

6.2.1.1 Plasmon conductivity model

The Plasmon model was proposed as a generalization of the Drude-Lorentz model [201], where carriers experience an electrostatic restoring force. This model describes the conductivity of carriers where they are smaller than the THz wavelength. Due to this variance, charge carriers cannot travel beyond the system's boundaries, which creates Plasmon resonance. Therefore, the motion of charge carriers is described considering the motion of the forced damped harmonic oscillator.

$$\frac{d^2x}{dt^2} + \gamma\frac{dx}{dt} + \omega_0^2 x = \frac{q}{m^*}E_{THz} \tag{6.8}$$

Here ω_0 is the resonant frequency of the oscillator. Considering equation 6.8 the Plasmon conductivity model can be described as

$$\tilde{\sigma}_p(\omega) = \left(\frac{Nq^2}{m^*}\right)\left(\frac{\tau}{1 - i\tau\left(\omega - \omega_0^2/\omega\right)}\right). \tag{6.9}$$

The Plasmon model exhibits a negative imaginary part, and the model can be simplified to the Drude model when $\omega_0 \ll \omega$. The resonant frequency can be represented as

$$\omega_0 = \sqrt{g \frac{Nq^2}{\epsilon_0 m^*}}, \tag{6.10}$$

where g is related to the dielectric constant and geometry of the system. The Plasmon model is well suited for metallic nanostructure materials where the ω_0 lies in ultra-violate, visible, and near-infrared range due to higher carrier densities. But for semiconductor nanostructures, ω_0 lies in the THz range because of lower carrier densities than the metallic structures. It follows a linear relationship with the square root of carrier density.

6.2.1.2 Hopping conductivity model

Hopping model [202] is another way to analyze THz conductivity by treating the carrier transport consisting of an intra-particle and an inter-particle component. In these MQW heterostructures, there is a probability of carriers tunneling through one grain to another quantum mechanically, contributing to the system's overall conductivity.

The conductivity arising from quantum tunneling is represented by

$$\tilde{\sigma}_t = \frac{N_t e^2 d_b^2}{6 k_B T \tau_t}, \tag{6.11}$$

where $N_t, e, k_B, d_b, \tau_t,$ and T are tunneling carrier density, charge of carrier, Boltzmann constant, barrier width, tunneling time, and lattice temperature respectively. Therefore, Hopping conductivity arises from tunneling is

$$\tilde{\sigma}_h(\omega) = \frac{-\tilde{\sigma}_t i\omega\tau_t}{\ln\left(1 - i\omega\tau_t\right)}. \tag{6.12}$$

Therefore, the total conductivity of the system is calculated by

$$\frac{1}{\tilde{\sigma}^*(\omega)} = \frac{f}{\tilde{\sigma}_L(\omega)} + \frac{1-f}{\tilde{\sigma}_h(\omega)}, \tag{6.13}$$

where intra-particle conductivity is assumed to be in the form of the Drude-Lorentz model (section 3.1), and effective conductivity $\tilde{\sigma}^*(\omega)$ was calculated by considering two channels combined in series, where f is the volume filling fraction. Therefore this model is also a suitable candidate to describe the conductivity of the systems like MQW structures.

6.2.2 AC-photoconductivity model for MQW system

To identify the suitable conductivity model for the AC-photoconductivity of the system, the Hopping model, Plasmon model, and Drude-Smith model were fitted to the data at 4 K, and parameters and goodness of fit were compared. Figure 6.2 shows the fitting for each model. Complex photoconductivity data were chosen to be in the range of 0.2 THz - 1.5 THz for all the data.

To compare the extracted carrier densities, the photoexcited carrier density was calculated using the method discussed in section 5.3. The calculated value for N_{exc} at 3 ps after photo excitation for 1.03 eV ($\alpha d \approx 0.24$) excitation is $2.6 \times 10^{13}\ \ \mathrm{cm}^{-2}$.

Table 6.1: Fitting parameters of Hopping model.

$N\left(\mathrm{cm}^{-2}\right)$	$N_t\left(\mathrm{cm}^{-2}\right)$	$N+N_t\left(\mathrm{cm}^{-2}\right)$	$\tau(\mathrm{s})$	$\tau_t(\mathrm{s})$	f
2.06×10^{12}	1.05×10^{11}	2.17×10^{12}	8.56×10^{-15}	7.6×10^{-18}	0.0115

Figure 6.2(b) shows the fitting, and Table 6.1 shows the extracted parameters of Hopping model fitting. According to the parameters, the total density is an order of magnitude smaller than the photo-excited carrier density. Moreover, the tunneling rate exceeds the carrier-carrier scattering rate by $\times 10^3$ times. This is not possible because carrier-carrier scattering happens much faster than the tunneling rate. Also, intra-particle conductivity

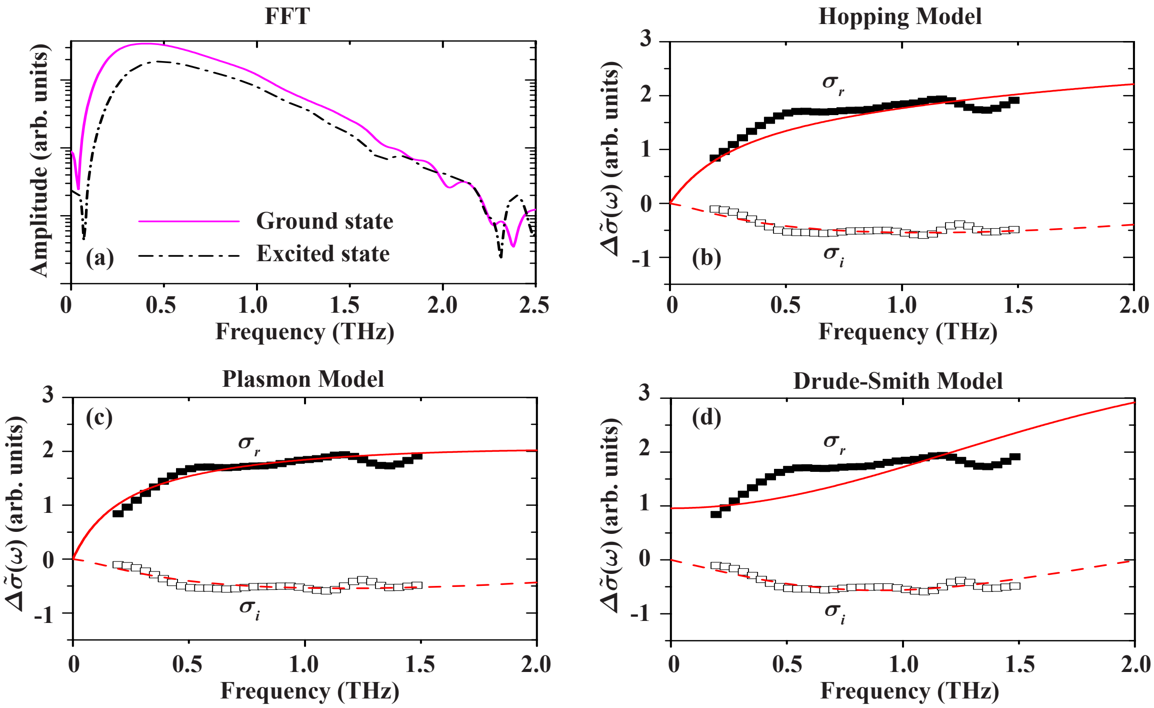

Figure 6.2: (a) FFT of THz transmission through the ground-state and photo excited-state of MQW sample. Real (σ_r) and imaginary (σ_i) parts of AC-photoconductivity fitted using (b) Hopping model, (c) Plasmon model, and (d) Drude-Smith model.

should have a higher filling fraction than the Hopping conductivity because tunneling probability should be very small. Due to these reasons, the Hopping model can be rejected for modeling the AC photoconductivity in the MQW sample.

Table 6.2: Fitting parameters of Drude-Smith model.

$N\ (\text{cm}^{-2})$	$\tau(\text{s})$	c_b
2.42×10^{13}	5.45×10^{-14}	-0.81

Figure 6.2(d) shows the fitting, and Table 6.2 shows the extracted parameters of Drude-Smith fitting for conductivity data. According to the data, the photoexcited carrier density is approximately the same as the calculated carrier density at 3 ps pump delay time. The

carriers have close to total backscattering because $c_b = -0.81$ for a single scattering event. This is reasonable due to the sample being a thin film. The fitting shows nonzero conductivity at zero frequency, but this contradicts with the data. Data clearly shows zero conductivity at zero frequency.

Table 6.3: Fitting parameters of Plasmon model.

$N\left(\mathrm{cm}^{-2}\right)$	$\omega_0(\mathrm{THz})$	$\tau(\mathrm{s})$
2.71×10^{13}	2.85	2.23×10^{-14}

Next, the Plasmon model was fitted to the conductivity data. According to the extracted parameters (Table 6.3), the carrier density follows the calculated excited carrier density. Also, fit [Figure 6.2(c)] follows the experimental data, indicating zero conductivity at zero frequency. The resonant frequency lies in UV, visible, and near IR ranges for metallic nanostructures. However, for semiconductor nanostructures, it lies in the THz range because of the lower carrier density in the structure compared to metallic structures. Considering the fitting accuracy and the excited carrier density comparison, it can be concluded that the Plasmon model is the best conductivity model for the analysis of photoconductivity in the InAs/AlAsSb MQW sample.

6.3 AC-photoconductivity in InAs/AlAsSb MQW

A complex AC-photoconductivity spectrum $\Delta\tilde{\sigma}(\omega)$) is determined from the time-domain THz transmission spectra for excited-states discussed in section 6.2.

Figure 6.3(a) shows the real and imaginary parts of $\Delta\tilde{\sigma}(\omega) = \sigma_r(\omega) + i\sigma_i(\omega)$ for a series of pump-probe delay times with fixed excitation at 1.03 eV and lattice temperature of 4 K.

Increasing Δt reduces the excited-carrier density N_{exc}, because carriers relax and recombine through a range of dynamic mechanisms [181, 190]. Conductivity is directly proportional to N_{exc} [139], therefore σ_r (and to some extent σ_i) is also expected to decrease with increasing Δt. However, as carrier density decreases, the mean free path l_f of those excited carriers increase. The scattering time is $\tau = l_f / v_{th}$, where

$$v_{th} = \sqrt{\frac{3k_B T}{m^*}} \tag{6.14}$$

is the thermal velocity of the carrier. Estimated values for l_f are presented in Table 6.4 and discussed later. It is now clear that both through the mean-free path, the scattering time is indirectly dependent on N_{exc} and on closer inspection, the conductivity may not decrease directly proportionally to N_{exc}.

Figure 6.3(b) shows σ_r and σ_i for excitation energies of 0.93 eV and 1.03 eV for $\Delta t = 3$ ps and $T = 4$ K. Overall, the higher excitation energy has a stronger conductivity, which is indicative of a higher N_{exc}. This is consistent with data determined from the photon-energy-dependent excitation dependence and dynamics described thoroughly in the previous chapter. Figure 6.3(c), shows the transient absorption at the maximum of the ground-state THz field $E^{\max}_{QW/ground}$ converted into excited carrier density (discussed in section 5.3). Results confirm that at short delay times, N_{exc} is indeed higher for the 1.03 eV excitation. These two photon energies straddle the onset of a metastable response, associated with an indirect hh3→e1 transition > 0.98 eV and a higher density of states. The dynamics in this regime have shown an increased Auger-scattering during early times that prolongs hot carriers beyond their lifetime arising from the phonon bottleneck due to a reduced thermal conductivity [50].

Spectra in Figure 6.3(a) and (b) where fitted using the Plasmon conductivity model (section 6.2.1.1) to match positive σ_r and negative σ_i, with both trending toward zero for low frequency with geometry factor g being 0.52 [136]. The Plasmon model has previously

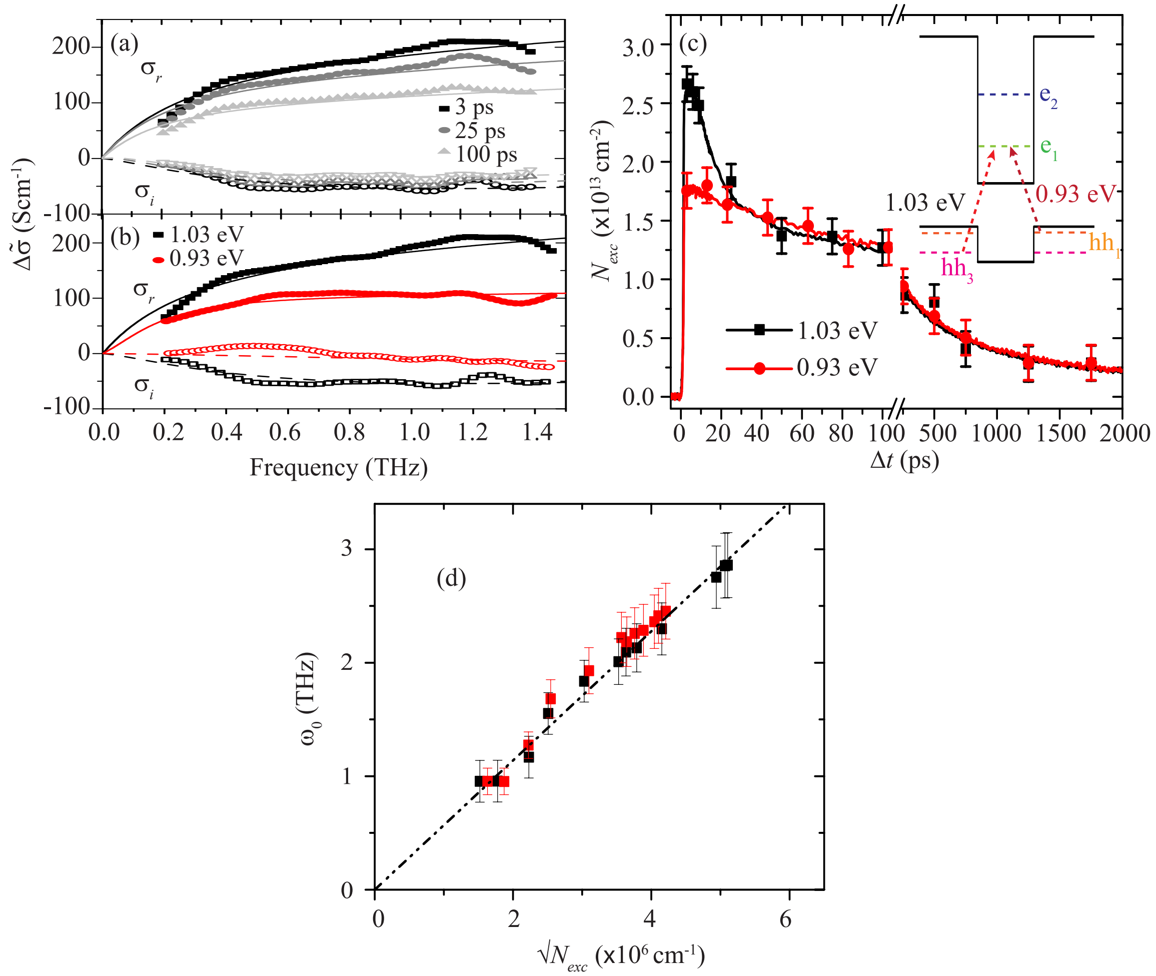

Figure 6.3: AC photoconductivity spectra for the MQW sample at a lattice temperature of 4 K for (a) a range of pump-probe delay times and fixed excitation of 1.03 eV, and (b) excitation of 0.93 eV and 1.03 eV for fixed $\Delta t = 3$ ps. All the results are fitted with a Plasmon conductivity modelling. (c) Photocarrier density versus pump-probe delay time for both excitation energies measured by transient absorption of $E^{\max}_{QW/ground}$ (solid lines), overlaid with the N_{exc} from the Plasmon model for various excitation conditions. Inset shows the two excitation schemes in a single quantum well. (d) Resonant frequency as a function of the square root of photoexcited carriers. Figures (a)-(c) are modified from Piyathilaka *et al.* [203].

been applied to semiconductors and their nanostructures. It agrees well with the measured spectra for all pump-probe delay times for both 0.93 eV and 1.03 eV photoexcitation. In all the cases, the photocarriers experience a restoring force because charge separation occurs upon excitation followed by strongly damped harmonic oscillatory motion with ω_0, where this changes linearly with respect to the $\sqrt{N_{exc}}$ from 0.95 THz to 2.85 THz [see Figure 6.3(d)].

Figure 6.3(c) shows the extracted $N_{exc}(\Delta t)$ (data points) overlaid on the directly measured transients. The transients only measure variations in the maximum $E_{QW/ground}(\omega)$ in the THz trace while varying Δt and are insensitive to the subtleties of the full THz spectrum. Additionally, fitting the full THz spectrum by the Plasmon (or other) model considers the sample geometry and carrier scattering mechanisms, such that N_{exc} can return values that do not match that of the transient. A good agreement between the two approaches further confirms the validity of the Plasmon model.

The temperature and excitation dependencies of the excited carrier transport in the metastable regime are obtained using the same approach, namely, by fitting the Plasmon model to the AC photoconductivity spectra for the MQW sample with excitation at 1.03 eV. Figure 6.4 shows typical results for σ_r and σ_i excited at 1.03 eV comparing $\Delta t = 3$ ps and 90 ps for (a) $T = 4$ K and (b) $T = 300$ K. At both temperatures the earlier conductivity is stronger and approximately equal. As with the excitation energy comparison, the excitation density decreases with increasing Δt, with a reduction in σ_r (@1 THz) from 3 ps to 90 ps is $\sim 60\%$ at $T = 4$ K and only $\sim 35\%$ at 300 K. This result is consistent with a slower carrier density decay at the higher temperature [142]. All spectra exhibit the characteristics of the Plasmon model, so values of N_{exc} can be extracted for lattice temperature and pump-probe delay time.

Figure 6.4(c) shows $N_{exc}(\Delta t)$ for 1.03 eV photoexcitation $T = \{4,100,200 \;\&\; 300\}$ K de-

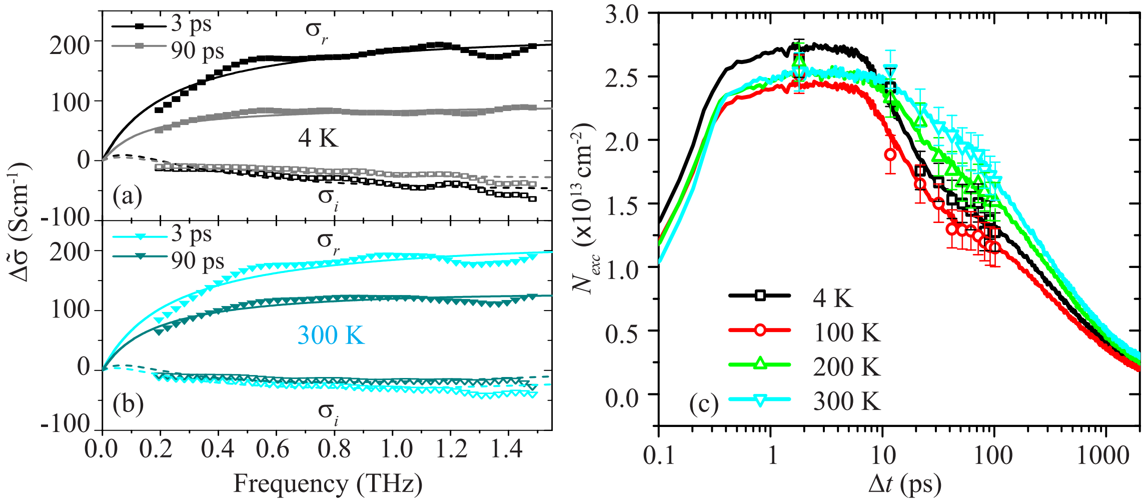

Figure 6.4: AC photoconductivity spectra for the MQW sample excited at 1.03 eV for $\Delta t = 3$ ps and 90 ps at (a) 4 K and (b) 300 K. (c) Photocarrier density decays for excitation of 1.03 eV for a range of lattice temperatures from transient absorption (solid lines) and Plasmon modelling (points). Figure modified from Piyathilaka *et al.* [203].

termined from the transient absorption (solids lines) and the Plasmon model (data points). The measured and extracted N_{exc} match for the entire temperature and delay-time parameter space. Results are plotted on a semilog scale to accentuate the various decay regions, especially the metastability distinctly observed as a $\sim$ 10 ps plateau in the 4 K and 100 K transient signals [142]. This plateau is less visible in the 200 K and 300 K transients. At 300 K, the hole bands are expected to flatten sufficiently throughout the Brillouin zone, overcoming the indirect nature of the hh3→e1 transition that is expected to be responsible for the metastability [151]. As with the individual AC photoconductivity spectra, the higher temperature shows a slower decay due to an extended hot carrier density that is slow to recombine because the charge-to-thermal energy pathway is hindered, both by a phonon bottleneck in the decay of optical-to-acoustic phonon scattering and low thermal conductivity [50], resulting in reabsorption of optical phonons by carrier that prevents their thermalization. Therefore, at higher temperatures, the higher conductivity persists for longer and is not enhanced or diminished by the lack of metastability exhibited at lower lattice temperatures.

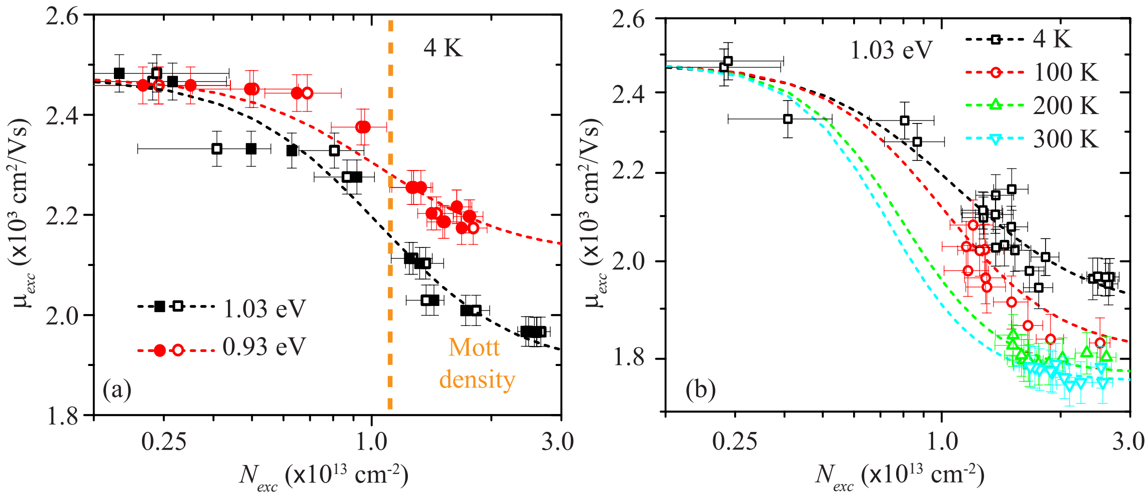

Figure 6.5: Mobility versus carrier density for the MQW sample at (a) 4 K, photoexcited at 0.93 eV and 1.03 eV, and (b) photoexcited at 1.03 eV for a range of lattice temperatures. Filled and open symbols represent $\mu(N_{exc})$ extracted carrier density from the transient absorption and the Plasmon model respectively. Data are empirically fitted with the Caughey-Thomas curves. Figure modified from Piyathilaka *et al.* [203].

Scattering times (τ) determined from the Plasmon model are related to the carrier mobility $\mu = e\tau/m^*$. Since τ are simultaneously found with the N_{exc}, $\mu(N_{exc})$ can be plotted to illustrate the effect of carrier-carrier interaction on the mobility for different excitation conditions. Figure 6.5(a) shows $\mu(N_{exc})$ for 1.03 eV and 0.93 eV photoexcitation at $T = 4$ K. Data points are obtained from both the transient and Plasmon model estimates of N_{exc} At both excitation energies, $\mu(N_{exc})$ starts at a similar value and then decreases with higher carrier concentration in a manner that looks like the hyperbolic tangent of a Fermi-Dirac distribution. This is consistent with the doping-concentration dependency of mobility identified by Caughey-Thomas as sigmoidal curves [204] and applied elsewhere in photoexcited carrier GaAs [83] and Si [139] probed by time-resolved THz spectroscopy. The $\mu(N_{exc})$ data can be empirically fitted by

$$\mu^{\|} = \frac{\mu^{\|}_{\text{max}} - \mu^{\|}_{\text{min}}}{1 + (N_{exc}/N_c)^{\beta}} + \mu^{\|}_{\text{min}}, \tag{6.15}$$

where $\mu^{\|}_{\text{max}}$ and $\mu^{\|}_{\text{min}}$ are the maximum and the minimum mobility driven parallel to the THz electric field, and N_c and β are the center and slope of the inflection between the maximum and minimum values. For $N_{exc} < 2 \times 10^{12}$ cm^{-2}, $\mu^{\|}_{\text{max}} \approx 2.48 \times 10^3$ cm^2/Vs and $N_c \approx 1.04 \times 10^{13}$ cm^{-2} for both excitations, whereas $\mu^{\|}_{\text{min}} \approx 2.13 \times 10^3$ cm^2/Vs and $\approx 1.85 \times 10^3$ cm^2/Vs for 0.93 eV and 1.03 eV excitation respectively. The lower $\mu^{\|}_{\text{min}}$ for 1.03 eV excitation is due to an increased carrier-carrier scattering, that decreases the mean-free path between scattering events, and hence a decreased drift velocity ($v_d = -\mu^{\|}E$). Given a maximum driving THz field of ≈ 25 kV/cm the maximum v_d is 6.2×10^7 cm/s for both excitation energies, which drops to minima of 5.33×10^7 cm/s and 4.63×10^7 cm/s for 0.93 eV and 1.03 eV excitation energy. These values are consistent with v_d reported in confined 2D structures [205–208].

Figure 6.5(b) shows $\mu(N_{exc})$ as a function of T for 1.03 eV photoexcitation. For $T = 4$ K, data are the same as in Figure 6.5(a), while the other temperature data are acquired using μ from the Plasmon model and N_{exc} from the transient absorption. All four data sets exhibit the same sigmoidal behavior consistent with the Caughey-Thomas curves, with fitting values given in Table 6.4. For all four temperatures, the maximum mobility is set to $\mu^{\|}_{\text{max}} \approx 2.48 \times 10^3$ cm^2/Vs consistent with the data from Figure 6.5(a), because this value is determined from the low-excitation-density region of the transient where N_{exc} is decaying toward zero regardless of the temperature. Moreover, this value is two orders of magnitude larger than the ground-state carrier density (determined without the use of an optical excitation pulse) and hence seems to be unrelated to and unaffected by the lattice temperature that only weakly affects the AC conductivity results [Figure 3.3].

The remainder of the fitting parameters, by contrast are temperature-dependent: Increasing T decreases $\mu^{\|}_{\text{min}}$ and N_c, and increases β. The reduction in $\mu^{\|}_{\text{min}}$ may suggest increased scattering at the early times after excitation even though there is little change in the carrier density and unlike the photon energy independence of the position of N_c, its change, in this case, suggests carrier-lattice interactions. The increase in β simply means that the transition from $\mu^{\|}_{\text{max}}$ to $\mu^{\|}_{\text{min}}$ occurs over a narrower range of carrier density.

Table 6.4: Caughey-Thomas curve fitting parameters, calculated ambipolar diffusion coefficient and mean free path for a range of lattice temperatures. Table modified from Piyathilaka *et al.* [203]

T (K)	$\mu^{\|}_{\text{min}}$ $(\times 10^3\text{cm}^2/\text{Vs})$	N_c $(\times 10^{13}\text{cm}^{-2})$	D_{am} (cm^2/s)	L_D (nm)	l_f (nm)
4	1.85 ± 0.08	1.04 ± 0.05	0.4 ± 0.03	24.5 ± 0.5	2.13 ± 0.07
100	1.80 ± 0.08	0.95 ± 0.05	10.19 ± 0.67	174.8 ± 0.9	9.92 ± 0.38
200	1.78 ± 0.08	0.75 ± 0.04	20.44 ± 1.34	391.5 ± 2.7	13.82 ± 0.54
300	1.76 ± 0.08	0.70 ± 0.04	30.74 ± 2.01	619.9 ± 3.5	16.67 ± 0.66

Carrier mobility is related to the MQW structure, and it is known that the electrodynamics properties of nanostructures are often excitonic, especially when length scales within the structure are smaller than the excitonic Bohr radius [209, 210]. In this case, because the AC photoconductivity fits a Plasmon model, the excited carriers are considered as electron-hole pairs, that are loosely bound and experience ambipolar diffusion. The exciton Bohr radius is

$$a_X = \frac{\hbar^2 \varepsilon}{e^2 m_r^*}, \tag{6.16}$$

approximately 3 nm [211, 212], where ε and m_r^* are the permittivity and reduced effective mass estimated from values of InAs and AlAsSb [149], and $\hbar$ is the reduced Planck constant. From the Bohr radius, the Mott density is estimated to be

$$N_{Mott} = \frac{1}{a_X^2}, \tag{6.17}$$

approximately 1.1×10^{13} cm^{-2} [213], which denotes the transition from a gas to a plasma of the charge carriers, and it is illustrated by a dashed vertical line in Figure 6.5(a). For comparison, the recombination dynamics have been assessed at different temperatures [142], demonstrating that at early times of the transient, corresponding to $\mu^{\parallel}_{\min}$, are likely dominated by Auger recombination, whereas $N_c(4\text{ K}) \approx N_{Mott}$ occurs in the carrier density range where radiative recombination dominates, and $\mu^{\parallel}_{\max}$ corresponds to a carrier density dominated by SRH recombination. For low temperature, the Mott density is slightly below the transition from dynamics dominated by radiative recombination ($N_{exc} < N_{Mott}$) to Auger recombination $N_{exc} > N_{Mott}$. For the low temperature, it is reasonable that Auger scattering leads to the break up of electron-hole pairs and energizes a plasma of the majority carriers. At higher temperatures, this transition to Auger recombination does not occur, so while the dynamics offer insight into the low temperature, they do not completely explain the variation in N_c through the Mott density.

A drift-diffusion model can be applied to the transport of the native and excited carriers. Shortly after excitation, photocarriers act as mostly neutral electron-hole pairs, so that they are only partly driven by the probe THz electric field. Moreover, the drift contribution is weakly dependent on temperature because the THz probe is fixed in strength. Hence, the following analysis is limited to ambipolar diffusion [214] determined by an Einstein model to be

$$D_{am}\left(T\right) = \frac{k_B T}{e}\left[\left(2N_{exc} + N_0\right) / \left(\frac{N_{exc}}{\mu_p} + \frac{N_{exc} + N_0}{\mu_n}\right)\right], \tag{6.18}$$

where N_0 is native carrier concentration estimated from ground-state AC conductivity and photoluminescence to be $\approx 0.5(1.5) \times 10^{11}$ cm^{-2} at low(high) lattice temperatures, and

$\mu_{n(p)}$ are electron(hole) mobility estimated from

$$\mu^{\|}_{\text{min}} \approx \tfrac{\mu_n \mu_p}{\mu_n + \mu_p}, \tag{6.19}$$

$$\mu^{\|}_{\text{max}} \approx \mu_n + \mu_p, \tag{6.20}$$

because $N_{exc} \gg N_0$ [214].

In Table 6.4, D_{am} is shown to increase as a function of temperature, which results in an increase in the average distance a carrier travels between excitation and recombination. This is characterized by the diffusion length [215, 216]

$$L_D = \sqrt{D_{am}\tau_R}, \tag{6.21}$$

where τ_R is the carrier lifetime. Table 6.4 also shows L_D values estimated with τ_R set as the first decay component for fitting the transient absorption [142]. Figure 6.4(c) shows that τ_R increases with lattice temperature and leads to a larger N_{exc} at longer Δt delays. Hence, as T increases τ_R and $\mu^{\|}_{\text{min}}$ are inversely correlated and the measured values $\mu^{\|}_{\text{min}}$ persist to lower values of N_{exc}. This effect result in decreasing N_c with T.

Overall, as the carrier dynamics in the region of $\mu^{\|}_{\text{min}}$ transition from Auger to radiative recombination with increasing temperature, D_{am} and L_D increase and $\mu^{\|}_{\text{min}}$ decreases as is seen in the Figure 6.5(b). Increased diffusion might be expected to spread the carriers in space and reduce the likelihood of Auger scattering. Additionally, this can be related to the mean-free path l_f that is also tabulated above. Comparison shows that both L_D and l_f increase with T, but the ratio L_D/l_f reveals that there are approximately 11(37) scattering events on average before recombination at low(high) lattice temperatures. Figure 6.6(a) summarizes the photocarrier dynamics (Auger, then radiative then SRH) and transport through diffusion. Schematic diagrams of the photocarrier distribution during the cooling process are shown at (b) $T \approx 4$ K, where strong Auger recombination initially occurs, and (c) $T \approx 300$ K, where diffusion quickly spreads the distribution. The increased scattering at higher temperature is consistent with a decreased $\mu^{\|}_{\min}$. Hence, in the extremely high excitation regime, lower temperature leads to both the metastable dynamics and the better mobility.

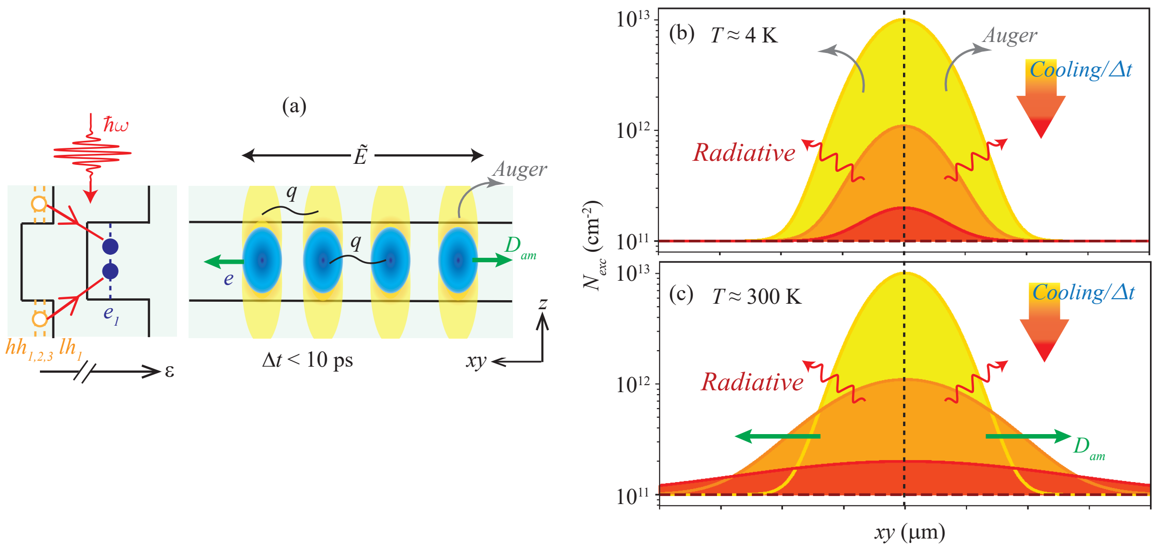

Figure 6.6: (a) Schematic diagram of the type-II band alignment, photoexcitation of charge carriers into e1, hh1-3, lh1 bands, and the interaction of carriers including diffusion (D_{am}), Auger scattering and electron-phonon scattering (q). [ϵ is band energy, $\hbar\omega$ is the photon energy.] These interactions vary the spatial distribution of the cooling charge carriers depending on the lattice temperature and are illustrated for (b) $T \approx 4$ K and (c) $T \approx 300$ K. Figure modified from Piyathilaka *et al.* [203].

Finally, the sample temperature will affect photocarrier transport through interactions with the lattice. The data shows that $\mu^{\|}_{\max}(T)$ is temperature independent and that $\mu^{\|}_{\min}(T)$ decreases somewhat linearly by only about 5% over the temperature range. The weakness of the latter tem-perature dependence does not match any individual compo-nent of the ground-state carrier-lattice interaction which are determined by either THz spectroscopy or Hall-effect measurements [162] (discussed in Chapter 3). Namely, carrier mobility $\propto T^{-0.5}$ due to deformation potential scattering, $\propto T^{1.5}$ due to piezoelectric potential scattering and

$\propto \exp(1/T)$ for polar optical scattering. To maintain an almost T-independent response, piezoelectric potential scattering by acoustic phonons and polar optical scattering limits the carrier mobility in the low and high-temperature regimes, respectively. While more data is required to properly interpret the carrier-lattice interactions, it is clear that the carrier density has a more significant effect on the transport than the temperature dependence. This sug-gests that temperature would play a smaller role in limiting the operational range for InAs/AlAsSb-based devices.

6.4 Chapter Summary

AC photoconductivity measurements are presented for the InAs/AlAsSb MQW that exhibits metastability in the charge carrier dynamics at an early time for cryogenic temperatures. Due to the increased density of states, the high carrier concentration in this region leads to larger AC photoconductivity compared to the measurement performed below the excitation energy onset of the metastability and for the same lattice temperature. However, the increased AC photoconductivity in the metastable regime translates into slightly lower carrier mobility than without the metastable carrier dynamics.

The excitation density dependence of the mobility in the metastable regime is related to the Auger scattering (discussed in Chapter 5). It converts the excited electron-hole gas into an electron plasma. As the lattice temperature increases, this process is switched off, and the ambipolar diffusion of the electron-hole gas decreasing dominates the transport. Increasing temperature also leads to more significant scattering before recombination, decreasing the high carrier concentration mobility.

Chapter 7:

Conclusion

7.1 Summary of Thesis

This thesis used Terahertz spectroscopy techniques to investigate the hot carrier dynamics and transport mechanisms in InAl/AlAsSb type-II MQW structure. Identifying the carrier relaxation and carrier transport characteristics is essential, as the MQW system is a potential candidate for developing the HCSC absorber.

This work presented experimental results on two bases: (i) exploration of the system's intrinsic nonexcited (ground) state properties (ii) characterization of the hot carriers. Analysis indicated that lattice temperature significantly influences the ground-state conductivity, carrier density, and carrier mobility of this MQW structure. Fermi-Dirac analysis showed that the system contained 1.45×10^{11} cm^{-2} unintentional doping concentration. It also showed that in the unexcited ground-state mobility is dominated by impurities and optical phonons.

Using the optical pump-THz probe measurements, hot carriers were observed, persisting long excited-state lifetimes. This is attributed to the system's inhibited phonon bottleneck and the dynamic band alignment. Pump energy-dependent studies showed metastability of photoexcited carriers when the excitation energy exceeded $\sim$ 100 meV at sufficiently low lattice temperature for carrier densities above the Mott density. Dynamics of the metastable state were dominated by Auger scattering, and the scattering rate depended on the lattice temperature and the excitation carrier density. These phenomena correspond to the local minima in the non-zero in-plane wavevector states of the valence band.

AC photoconductivity measurements are presented for a type-II InAs/AlAsSb heterostructures to determine the transport of photocarriers for a range of lattice temperatures and excitation conditions. The results complement photocarrier dynamics that identified the recombination mechanisms and highlighted an intriguing metastability at low temperatures and for sufficient excess excitation energy. While the photon energy dependence shows that carrier transport in the metastable regime's exhibits higher conductivity, the mobility is slightly reduced compared to other excitation regimes.

At lower excitation densities that are within the reach of moderate solar concentration, photocarrier transport is temperature independent. At warmer temperatures close to ambient operating conditions, hot-carrier lifetimes remain pro-longed, and ambipolar diffusion and radiative recombination govern the transport and dynamics. Moreover, mobility for low excitation density is comparable to elemental and III-V based photovoltaic devices [24, 217, 218], and exceeds that of organic [219] and hybrid-perovskite [220] solar cells by several orders of magnitude.

In principle, the increased Auger scattering rate for higher excitation and the rapid reduction in carrier density with a long lifetime could be beneficial for hot carriers in solar cell applications that exploit solar concentrators. However, this would necessitate cryogenic lattice temperatures and result in reduced carrier mobility despite of increased conductivity. This would have a significant implication on the design parameters of HCSCs. By contrast, operating near room temperature results in low mobility, moderate conductivity, and slower carrier recombination. In this regime, HCSCs may demonstrate reasonable efficiency. Therefore, efforts should be made to adjust the band structure to operate at solar-friendly regimes and to develop multiple energy-selective contacts for hot-carrier extraction [see Figure 7.1].

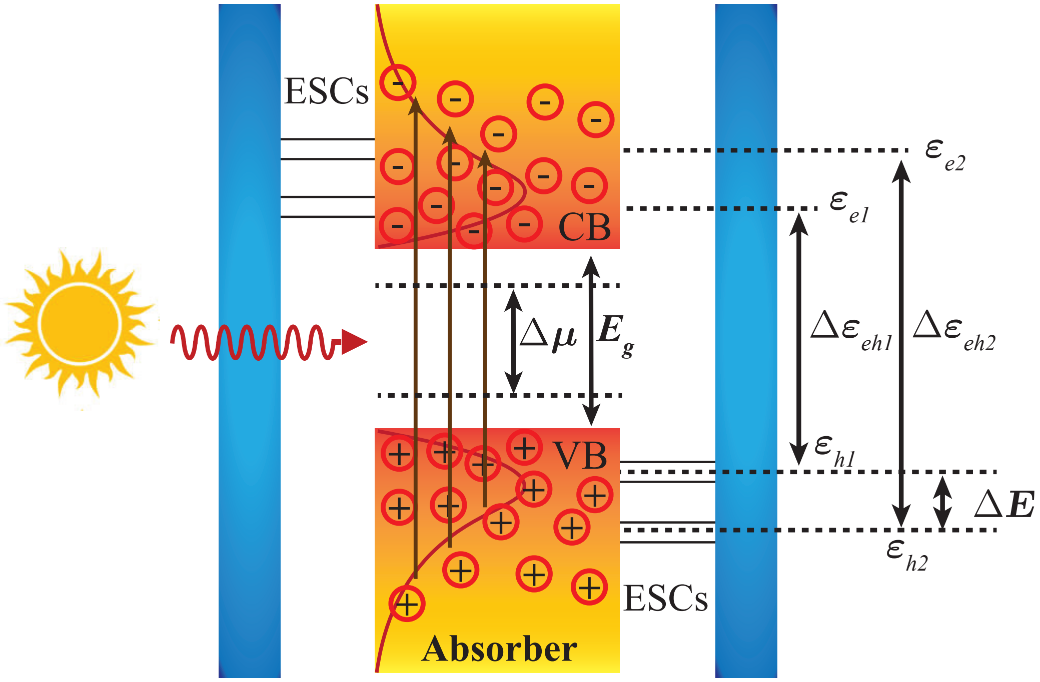

Figure 7.1: Schematic diagram of hot-carrier solar cell with multiple energy-selective contacts.

7.2 Future Research

Even though most of the carrier dynamics and carrier transport mechanisms are discussed in this thesis, further investigations are still available. In the THz-TDS experiments, we investigated the characteristics of all the carriers in the system. Characteristics were not identified for electrons and holes separately. It is possible to characterize the behavior of minority and majority carriers separately by applying an external magnetic. In addition, the bandwidth of the THz spectrum in the setup is limited to 1.5 THz. This can be increased by using thin $CdSiP_2$ crystal [117], different windows for cryostat, and different detection crystals. By exceeding this limit, an identification of the resonant features of the photoconductivity of the system will be possible. Achieving the bandwidth of 10 THz at room temperature will identify the resonant due to phonons in the MQW system.

The carrier dynamics and transport mechanisms of photoexcited carriers were investigated by exciting electrons just above the bandgap of the MQW system. Since the MQW system consists of L (1.26 eV) and X (1.86 eV) valleys, TRTS can be conducted by photoexciting the system just above those valleys' energies, and the valley dynamics of the MQW system can be explored as a function of pump intensity, lattice temperature, and the THz probe intensity. These experimental observations will provide details of the valley scattering time and the effect on the hot carrier lifetime due to the valley scattering.

Bibliography

[1] Hannah Ritchie and Max Roser. "Energy". In: *Our World in Data* (Nov. 28, 2020). URL: `https://ourworldindata.org/renewable-energy`.

[2] David Feldman et al. "U.S. Solar Photovoltaic System and Energy Storage Cost Benchmark: Q1 2020". In: *Renewable Energy* (2021), p. 120.

[3] Larry Partain et al. "'Swanson's Law' Plan to Mitigate Global Climate Change". In: *2016 IEEE 43rd Photovoltaic Specialists Conference (PVSC)*. 2016 IEEE 43rd Photovoltaic Specialists Conference (PVSC). June 2016, pp. 3335–3340. DOI: `10.1109/PVSC.2016.7750284`.

[4] Tomas Kåberger. "Progress of renewable electricity replacing fossil fuels". In: *Global Energy Interconnection* 1.1 (Jan. 2018), pp. 48–52. ISSN: 2096-5117. DOI: `10.14171/j.2096-5117.gei.2018.01.006`.

[5] Dmitrii Bogdanov et al. "Low-Cost Renewable Electricity as the Key Driver of the Global Energy Transition towards Sustainability". In: *Energy* 227 (July 15, 2021), p. 120467. ISSN: 0360-5442. DOI: `10.1016/j.energy.2021.120467`.

[6] Gregory M. Wilson et al. "The 2020 Photovoltaic Technologies Roadmap". In: *J. Phys. D: Appl. Phys.* 53.49 (Sept. 9, 2020), p. 493001. ISSN: 0022-3727. DOI: `10.1088/1361-6463/ab9c6a`.

[7] Vesselinka Petrova-Koch, Rudolf Hezel, and A. Goetzberger, eds. *High-Efficient Low-Cost Photovoltaics: Recent Developments.* Springer Series in Optical Sciences 140. Berlin: Springer, 2009. 225 pp. ISBN: 978-3-540-79358-8.

[8] E. Kymakis and G. a. J. Amaratunga. "Photovoltaic Cells Based on Dye-Sensitisation of Single-Wall Carbon Nanotubes in a Polymer Matrix". In: *Solar Energy Materials and Solar Cells* 4.80 (2003), pp. 465–472. ISSN: 0927-0248. DOI: `10.1016/j.solmat.2003.08.013`.

[9] *Solar Spectra.* URL: `https://www.nrel.gov/grid/solar-resource/spectra.html`.

[10] Nathan S. Lewis. "Powering the Planet". In: *MRS Bulletin* 32.10 (Oct. 2007), pp. 808–820. ISSN: 1938-1425, 0883-7694. DOI: `10.1557/mrs2007.168`.

[11] William Shockley and Hans J. Queisser. "Detailed Balance Limit of Efficiency of P-n Junction Solar Cells". In: *Journal of Applied Physics* 32.3 (Mar. 1961), pp. 510–519. ISSN: 0021-8979. DOI: `10.1063/1.1736034`.

[12] Matthew C. Beard, Joseph M. Luther, and Arthur J. Nozik. "The Promise and Challenge of Nanostructured Solar Cells". In: *Nature Nanotech* 9.12 (12 Dec. 2014), pp. 951–954. ISSN: 1748-3395. DOI: `10.1038/nnano.2014.292`.

[13] Sayak Bhattacharya and Sajeev John. "Beyond 30% Conversion Efficiency in Silicon Solar Cells: A Numerical Demonstration". In: *Sci Rep* 9.1 (1 Aug. 28, 2019), p. 12482. ISSN: 2045-2322. DOI: `10.1038/s41598-019-48981-w`.

[14] Louise Hirst et al. "Hot Carrier Dynamics in InGaAs/GaAsP Quantum Well Solar Cells". In: *2011 37th IEEE Photovoltaic Specialists Conference.* June 2011, pp. 003302–003306. DOI: `10.1109/PVSC.2011.6186643`.

[15] Louise C. Hirst and Nicholas J. Ekins-Daukes. "Quantifying Intrinsic Loss Mechanisms in Solar Cells: Why Is Power Efficiency Fundamentally Limited?" In: *Next*

Generation (Nano) Photonic and Cell Technologies for Solar Energy Conversion. Next Generation (Nano) Photonic and Cell Technologies for Solar Energy Conversion. Vol. 7772. SPIE, Aug. 24, 2010, pp. 124–129. DOI: `10.1117/12.860681`.

[16] Louise C. Hirst and Nicholas J. Ekins-Daukes. “Fundamental Losses in Solar Cells”. en. In: *Progress in Photovoltaics: Research and Applications* 19.3 (2011), pp. 286–293. ISSN: 1099-159X. DOI: `10.1002/pip.1024`.

[17] Daniel N. Micha et al. “Chapter 7 - Nanostructured Materials for High Efficiency Solar Cells”. In: *Sustainable Material Solutions for Solar Energy Technologies.* Ed. by Mariana Amorim Fraga et al. Solar Cell Engineering. Elsevier, Jan. 1, 2021, pp. 201–227. ISBN: 978-0-12-821592-0. DOI: `10.1016/B978-0-12-821592-0.00016-9`.

[18] Hans-Werner Schock. “Properties of Chalcopyrite-Based Materials and Film Deposition for Thin-Film Solar Cells”. en. In: *Thin-Film Solar Cells: Next Generation Photovoltaics and Its Applications.* Ed. by Yoshihiro Hamakawa. Springer Series in Photonics. Berlin, Heidelberg: Springer Berlin Heidelberg, 2004, pp. 163–182. ISBN: 978-3-662-10549-8. DOI: `10.1007/978-3-662-10549-8_10`.

[19] Taesoo D. Lee and Abasifreke U. Ebong. “A Review of Thin Film Solar Cell Technologies and Challenges”. In: *Renewable and Sustainable Energy Reviews* 70 (Apr. 1, 2017), pp. 1286–1297. ISSN: 1364-0321. DOI: `10.1016/j.rser.2016.12.028`.

[20] Gaurav Siddharth et al. “Progress in Thin Film Solar Cell and Advanced Technologies for Performance Improvement”. In: *Encyclopedia of Smart Materials.* Elsevier, 2022, pp. 661–680. ISBN: 978-0-12-815733-6. DOI: `10.1016/B978-0-12-815732-9.00115-7`.

[21] Susanne Siebentritt. “Chalcopyrite Compound Semiconductors for Thin Film Solar Cells”. In: *Current Opinion in Green and Sustainable Chemistry.* 4 Novel Materials

for Energy Production and Storage 2017 4 (Apr. 2017), pp. 1–7. ISSN: 2452-2236. DOI: `10.1016/j.cogsc.2017.02.001`.

[22] Martin A. Green. “Lambertian light trapping in textured solar cells and light-emitting diodes: analytical solutions”. In: *Progress in Photovoltaics: Research and Applications* 10.4 (2002). _eprint: https://onlinelibrary.wiley.com/doi/pdf/10.1002/pip.404, pp. 235–241. ISSN: 1099-159X. DOI: `10.1002/pip.404`.

[23] Wei Wang et al. “Broadband Light Absorption Enhancement in Thin-Film Silicon Solar Cells”. In: *Nano Lett.* 10.6 (June 2010), pp. 2012–2018. ISSN: 1530-6984, 1530-6992. DOI: `10.1021/nl904057p`.

[24] Hector Cotal et al. “III–V multijunction solar cells for concentrating photovoltaics”. In: *Energy Environ. Sci.* 2.2 (Jan. 2009). ZSCC: 0000566 Publisher: The Royal Society of Chemistry, pp. 174–192. ISSN: 1754-5706. DOI: `10.1039/B809257E`.

[25] *Multijunction III-V Photovoltaics Research.* Energy.gov. URL: `https://www.energy.gov/eere/solar/multijunction-iii-v-photovoltaics-research`.

[26] Antonio Luque, Antonio Martí, and Colin Stanley. “Understanding Intermediate-Band Solar Cells”. In: *Nature Photon* 6.3 (3 Mar. 2012), pp. 146–152. ISSN: 1749-4893. DOI: `10.1038/nphoton.2012.1`.

[27] T. Trupke, M. A. Green, and P. Würfel. “Improving Solar Cell Efficiencies by Down-Conversion of High-Energy Photons”. In: *Journal of Applied Physics* 92.3 (Aug. 2002), pp. 1668–1674. ISSN: 0021-8979. DOI: `10.1063/1.1492021`.

[28] Yunfei Shang et al. “Enhancing Solar Cell Efficiency Using Photon Upconversion Materials”. In: *Nanomaterials (Basel)* 5.4 (Oct. 27, 2015), pp. 1782–1809. ISSN: 2079-4991. DOI: `10.3390/nano5041782`. pmid: `28347095`.

[29] Deepak Verma, Tor O. Saetre, and Ole-Morten Midtgård. "Review on up/down Conversion Materials for Solar Cell Application". In: *2012 38th IEEE Photovoltaic Specialists Conference*. 2012 38th IEEE Photovoltaic Specialists Conference. June 2012, pp. 002608–002613. DOI: `10.1109/PVSC.2012.6318129`.

[30] Heather Goodwin et al. "Multiple Exciton Generation in Quantum Dot-Based Solar Cells". In: *Nanophotonics* 7.1 (Jan. 26, 2018), pp. 111–126. ISSN: 2192-8614. DOI: `10.1515/nanoph-2017-0034`.

[31] Robert T. Ross and Arthur J. Nozik. "Efficiency of Hot-carrier Solar Energy Converters". In: *Journal of Applied Physics* 53.5 (May 1982), pp. 3813–3818. ISSN: 0021-8979. DOI: `10.1063/1.331124`.

[32] D. K. Ferry. "In Search of a True Hot Carrier Solar Cell". In: *Semicond. Sci. Technol.* 34.4 (Mar. 2019), p. 044001. ISSN: 0268-1242. DOI: `10.1088/1361-6641/ab0bc3`.

[33] Wilfried GJHM van Sark et al. "Upconversion in Solar Cells". In: *Nanoscale Research Letters* 8.1 (Feb. 15, 2013), p. 81. ISSN: 1556-276X. DOI: `10.1186/1556-276X-8-81`.

[34] Jan Christoph Goldschmidt and Stefan Fischer. "Upconversion for Photovoltaics – a Review of Materials, Devices and Concepts for Performance Enhancement". In: *Advanced Optical Materials* 3.4 (2015), pp. 510–535. ISSN: 2195-1071. DOI: `10.1002/adom.201500024`.

[35] Hyun-Ju Kim et al. "Down Conversion of High-Energy Photons in Anatase-Based TiO 2 Solar Cells". In: Microelectronics, MEMS, and Nanotechnology. Ed. by Jung-Chih Chiao et al. Perth, Australia, Apr. 2, 2004, p. 507. DOI: `10.1117/12.530167`.

[36] Simon Kahmann and Maria A Loi. "Hot Carrier Solar Cells and the Potential of Perovskites for Breaking the Shockley–Queisser Limit". In: *Journal of Materials Chemistry C* (2019), p. 16.

[37] D. J. Farrell et al. “A Hot-Carrier Solar Cell with Optical Energy Selective Contacts”. In: *Appl. Phys. Lett.* 99.11 (Sept. 12, 2011), p. 111102. ISSN: 0003-6951, 1077-3118. DOI: `10.1063/1.3636401`.

[38] Yi Zhang et al. “A Review on Thermalization Mechanisms and Prospect Absorber Materials for the Hot Carrier Solar Cells”. In: *Solar Energy Materials and Solar Cells* 225 (June 2021), p. 111073. ISSN: 09270248. DOI: `10.1016/j.solmat.2021.111073`.

[39] D. K. Ferry et al. “Challenges, Myths, and Opportunities in Hot Carrier Solar Cells”. In: *Journal of Applied Physics* 128.22 (Dec. 2020), p. 220903. ISSN: 0021-8979. DOI: `10.1063/5.0028981`.

[40] H. Esmaielpour et al. “Control of Hot Carrier Thermalization in Type-II Quantum Wells: A Route to Practical Hot Carrier Solar Cells”. In: *2018 IEEE 7th World Conference on Photovoltaic Energy Conversion (WCPEC) (A Joint Conference of 45th IEEE PVSC, 28th PVSEC 34th EU PVSEC)*. June 2018, pp. 3682–3684. DOI: `10.1109/PVSC.2018.8548086`.

[41] Jean Rodière et al. “Experimental Evidence of Hot Carriers Solar Cell Operation in Multi-Quantum Wells Heterostructures”. In: *Appl. Phys. Lett.* 106.18 (May 4, 2015), p. 183901. ISSN: 0003-6951. DOI: `10.1063/1.4919901`.

[42] Hamidreza Esmaielpour et al. “Exploiting Intervalley Scattering to Harness Hot Carriers in III–V Solar Cells”. In: *Nat Energy* 5.4 (Apr. 2020), pp. 336–343. ISSN: 2058-7546. DOI: `10.1038/s41560-020-0602-0`.

[43] D König et al. “Non-Equilibrium Dynamics, Materials and Structures for Hot Carrier Solar Cells: A Detailed Review”. In: *Semicond. Sci. Technol.* (2020), p. 53.

[44] B. K. Ridley. “The Electron-Phonon Interaction in Quasi-Two-Dimensional Semiconductor Quantum-Well Structures”. In: *J. Phys. C: Solid State Phys.* 15.28 (Oct. 1982), pp. 5899–5917. ISSN: 0022-3719. DOI: `10.1088/0022-3719/15/28/021`.

[45] R. Heitz et al. “Existence of a Phonon Bottleneck for Excitons in Quantum Dots”. en. In: *Physical Review B* 64.24 (Nov. 2001). ISSN: 1098-0121, 1095-3795. DOI: `10.1103/PhysRevB.64.241305`.

[46] Y. Q. Huang et al. “Effect of a Phonon Bottleneck on Exciton and Spin Generation in Self-Assembled $In_{1-x}Ga_xAs$ Quantum Dots”. en. In: *Physical Review Applied* 9.4 (Apr. 2018). ISSN: 2331-7019. DOI: `10.1103/PhysRevApplied.9.044037`.

[47] Yi Zhang and Chao Huang. “Study the Mechanisms of Enhanced Phonon Bottleneck Effect for the Absorber of Hot Carrier Solar Cell in III-V Multiple Quantum Wells”. In: *Materials Science and Engineering* (2020), p. 9.

[48] *Advanced Concepts in Photovoltaics.* July 21, 2014. ISBN: 978-1-84973-591-9. DOI: `10.1039/9781849739955`.

[49] H. Esmaielpour et al. “Suppression of Phonon-Mediated Hot Carrier Relaxation in Type-II InAs/$AlAs_xSb_{1-x}$ Quantum Wells: A Practical Route to Hot Carrier Solar Cells”. In: *Prog. Photovolt: Res. Appl.* 24.5 (May 2016). Comment: 7 pages, 6 figures, submitted to ”Progress in Photovoltaics: Research and Applications”, pp. 591–599. ISSN: 10627995. DOI: `10.1002/pip.2763`. arXiv: `1511.00042`.

[50] Hamidreza Esmaielpour et al. “Enhanced Hot Electron Lifetimes in Quantum Wells with Inhibited Phonon Coupling”. In: *Scientific Reports* 8.1 (Aug. 2018), p. 12473. ISSN: 2045-2322. DOI: `10.1038/s41598-018-30894-9`.

[51] Peter Würfel. “Solar Energy Conversion with Hot Electrons from Impact Ionisation”. In: *Solar Energy Materials and Solar Cells* 1.46 (1997), pp. 43–52. ISSN: 0927-0248.

[52] James A. R. Dimmock et al. “Optoelectronic Characterization of Carrier Extraction in a Hot Carrier Photovoltaic Cell Structure”. In: *J. Opt.* 18.7 (May 2016), p. 074003. ISSN: 2040-8986. DOI: `10.1088/2040-8978/18/7/074003`.

[53] A. Luque and Steven Hegedus, eds. *Handbook of Photovoltaic Science and Engineering*. Hoboken, NJ: Wiley, 2003. 1138 pp. ISBN: 978-0-471-49196-5.

[54] D. König, Y. Takeda, and B. Puthen-Veettil. “Technology-Compatible Hot Carrier Solar Cell with Energy Selective Hot Carrier Absorber and Carrier-Selective Contacts”. In: *Appl. Phys. Lett.* 101.15 (Oct. 8, 2012), p. 153901. ISSN: 0003-6951. DOI: `10.1063/1.4757979`.

[55] Gavin Conibeer et al. “Progress on Hot Carrier Cells”. In: *Solar Energy Materials and Solar Cells*. 17th International Photovoltaic Science and Engineering Conference 93.6 (June 1, 2009), pp. 713–719. ISSN: 0927-0248. DOI: `10.1016/j.solmat.2008.09.034`.

[56] Santosh K. Shrestha, Pasquale Aliberti, and Gavin J. Conibeer. “Energy Selective Contacts for Hot Carrier Solar Cells”. In: *Solar Energy Materials and Solar Cells*. PVSEC 18 94.9 (Sept. 1, 2010), pp. 1546–1550. ISSN: 0927-0248. DOI: `10.1016/j.solmat.2009.11.029`.

[57] P. Würfel et al. “Particle Conservation in the Hot-Carrier Solar Cell”. In: *Progress in Photovoltaics: Research and Applications* 13.4 (2005), pp. 277–285. ISSN: 1099-159X. DOI: `10.1002/pip.584`.

[58] Shanhe Su et al. “Hot-Carrier Solar Cells With Quantum Well and Dot Energy Selective Contacts”. In: *IEEE Journal of Quantum Electronics* 51.9 (Sept. 2015). Conference Name: IEEE Journal of Quantum Electronics, pp. 1–8. ISSN: 1558-1713. DOI: `10.1109/JQE.2015.2469152`.

[59] Gavin Conibeer et al. “Hot Carrier Solar Cell Absorbers: Materials, Mechanisms and Nanostructures”. In: SPIE Solar Energy + Technology. Ed. by Oleg V. Sulima and Gavin Conibeer. San Diego, California, United States, Oct. 17, 2014, p. 917802. DOI: `10.1117/12.2067926`.

[60] L. C. Hirst et al. “Experimental Demonstration of Hot-Carrier Photo-Current in an InGaAs Quantum Well Solar Cell”. In: *Appl. Phys. Lett.* 104.23 (June 2014), p. 231115. ISSN: 0003-6951. DOI: `10.1063/1.4883648`.

[61] Xiang Yang et al. “Biomedical Applications of Terahertz Spectroscopy and Imaging”. English. In: *Trends in Biotechnology* 34.10 (Oct. 2016), pp. 810–824. ISSN: 0167-7799, 1879-3096. DOI: `10.1016/j.tibtech.2016.04.008`.

[62] H. A. Hafez et al. “Intense Terahertz Radiation and Their Applications”. en. In: *J. Opt.* 18.9 (2016), p. 093004. ISSN: 2040-8986. DOI: `10.1088/2040-8978/18/9/093004`.

[63] Chihun In and Hyunyong Choi. “Terahertz Investigation of Dirac Materials: Graphene and Topological Insulators”. In: *J. Korean Phys. Soc.* 72.12 (June 2018), pp. 1484–1490. ISSN: 1976-8524. DOI: `10.3938/jkps.72.1484`.

[64] Wentao Zhang et al. “Ultrafast terahertz magnetometry”. In: *Nat Commun* 11.1 (Dec. 2020), p. 4247. ISSN: 2041-1723. DOI: `10.1038/s41467-020-17935-6`.

[65] Arnab Bera et al. “Review of recent progress on THz spectroscopy of quantum materials: superconductors, magnetic and topological materials”. In: *Eur. Phys. J. Spec. Top.* 230.23 (Dec. 2021), pp. 4113–4139. ISSN: 1951-6401. DOI: `10.1140/epjs/s11734-021-00216-8`.

[66] Mohamed Abdellatif-Youssef et al. “Extended properties of magnetic spins of zinc ferrite nanoparticles in the THz frequency range”. In: *Journal of Magnetism and*

Magnetic Materials 525 (May 2021), p. 167574. ISSN: 0304-8853. DOI: `10.1016/j.jmmm.2020.167574`.

[67] Xiaojian Fu et al. "Ultralow temperature terahertz magnetic thermodynamics of perovskite-like SmFeO3 ceramic". In: *Sci Rep* 5.1 (Oct. 2015). Number: 1 Publisher: Nature Publishing Group, p. 14777. ISSN: 2045-2322. DOI: `10.1038/srep14777`.

[68] Ruth M. Woodward et al. "Terahertz Pulse Imaging in Reflection Geometry of Human Skin Cancer and Skin Tissue". In: *Phys. Med. Biol.* 47.21 (Oct. 2002), pp. 3853–3863. ISSN: 0031-9155. DOI: `10.1088/0031-9155/47/21/325`.

[69] A. Hirata et al. "120-GHz-band Millimeter-Wave Photonic Wireless Link for 10-Gb/s Data Transmission". In: *IEEE Transactions on Microwave Theory and Techniques* 54.5 (May 2006), pp. 1937–1944. ISSN: 1557-9670. DOI: `10.1109/TMTT.2006.872798`.

[70] Masayoshi Tonouchi. "Cutting-Edge Terahertz Technology". en. In: *Nature Photonics* 1.2 (Feb. 2007), pp. 97–105. ISSN: 1749-4885, 1749-4893. DOI: `10.1038/nphoton.2007.3`.

[71] Herath P. Piyathilaka et al. "Terahertz Generation by Optical Rectification in Chalcopyrite Crystals $ZnGeP_2$, $CdGeP_2$ and $CdSiP_2$". In: *Opt. Express, OE* 27.12 (June 2019), pp. 16958–16965. ISSN: 1094-4087. DOI: `10.1364/OE.27.016958`.

[72] J. D. Rowley et al. "Broadband Terahertz Pulse Emission from $ZnGeP_2$". EN. In: *Opt. Lett., OL* 37.5 (Mar. 2012), pp. 788–790. ISSN: 1539-4794. DOI: `10.1364/OL.37.000788`.

[73] Joseph D Rowley. "Chalcopyrite Semiconductors as Sources for Terahertz Spectroscopy". In: (), p. 102.

[74] T. Bartel et al. "Generation of Single-Cycle THz Transients with High Electric-Field Amplitudes". EN. In: *Opt. Lett., OL* 30.20 (Oct. 2005), pp. 2805–2807. ISSN: 1539-4794. DOI: `10.1364/OL.30.002805`.

[75] Katsuyoshi Aoki, Janne Savolainen, and Martina Havenith. "Broadband Terahertz Pulse Generation by Optical Rectification in GaP Crystals". In: *Appl. Phys. Lett.* 110.20 (May 2017), p. 201103. ISSN: 0003-6951. DOI: `10.1063/1.4983371`.

[76] J. Kroll, J. Darmo, and K. Unterrainer. "High-Performance Terahertz Electro-Optic Detector". In: *Electronics Letters* 40.12 (June 2004), pp. 763–764. ISSN: 0013-5194. DOI: `10.1049/el:20040492`.

[77] Q. Wu and X.-C. Zhang. "Free-space Electro-optic Sampling of Terahertz Beams". en. In: *Applied Physics Letters* 67.24 (Dec. 1995), pp. 3523–3525. ISSN: 0003-6951, 1077-3118. DOI: `10.1063/1.114909`.

[78] C. Winnewisser et al. "Electro-Optic Detection of THz Radiation in LiTaO3, LiNbO3 and ZnTe". en. In: *Applied Physics Letters* 70.23 (June 1997), pp. 3069–3071. ISSN: 0003-6951, 1077-3118. DOI: `10.1063/1.119093`.

[79] Q. Wu, M. Litz, and X.-C. Zhang. "Broadband Detection Capability of ZnTe Electro-optic Field Detectors". en. In: *Applied Physics Letters* 68.21 (May 1996), pp. 2924–2926. ISSN: 0003-6951, 1077-3118. DOI: `10.1063/1.116356`.

[80] I. H. Choi et al. "Optical and Vibrational Properties of the Chalcopyrite $CdGeP_2$". English. In: *Journal of the Korean Physical Society* 44.2 (2004), pp. 403–407. ISSN: ISSN 0374-4884.

[81] Lionel Duvillaret, Frédéric Garet, and Jean-Louis Coutaz. "Highly Precise Determination of Optical Constants and Sample Thickness in Terahertz Time-Domain

Spectroscopy”. EN. In: *Appl. Opt., AO* 38.2 (Jan. 1999), pp. 409–415. ISSN: 1539-4522. DOI: `10.1364/AO.38.000409`.

[82] Sesha Bamini N et al. “Time-Resolved Terahertz Spectroscopy Reveals the Influence of Charged Sensitizing Quantum Dots on the Electron Dynamics in ZnO”. en. In: *Physical Chemistry Chemical Physics* 19.8 (2017), pp. 6006–6012. DOI: `10.1039/C6CP07509F`.

[83] Matthew C. Beard, Gordon M. Turner, and Charles A. Schmuttenmaer. “Transient Photoconductivity in GaAs as Measured by Time-Resolved Terahertz Spectroscopy”. en. In: *Phys. Rev. B* 62.23 (Dec. 2000), pp. 15764–15777. ISSN: 0163-1829, 1095-3795. DOI: `10.1103/PhysRevB.62.15764`.

[84] Matthew C. Beard, Gordon M. Turner, and Charles A. Schmuttenmaer. “Size-Dependent Photoconductivity in CdSe Nanoparticles as Measured by Time-Resolved Terahertz Spectroscopy”. In: *Nano Lett.* 2.9 (Sept. 2002), pp. 983–987. ISSN: 1530-6984. DOI: `10.1021/nl0256210`.

[85] Xin Ai et al. “Photoinduced Charge Carrier Generation in a Poly(3-Hexylthiophene) and Methanofullerene Bulk Heterojunction Investigated by Time-Resolved Terahertz Spectroscopy †”. en. In: *The Journal of Physical Chemistry B* 110.50 (Dec. 2006), pp. 25462–25471. ISSN: 1520-6106, 1520-5207. DOI: `10.1021/jp065212i`.

[86] D. Grischkowsky et al. “Far-Infrared Time-Domain Spectroscopy with Terahertz Beams of Dielectrics and Semiconductors”. EN. In: *J. Opt. Soc. Am. B, JOSAB* 7.10 (Oct. 1990), pp. 2006–2015. ISSN: 1520-8540. DOI: `10.1364/JOSAB.7.002006`.

[87] R. Huber et al. “How Many-Particle Interactions Develop after Ultrafast Excitation of an Electron-Hole Plasma”. eng. In: *Nature* 414.6861 (Nov. 2001), pp. 286–289. ISSN: 0028-0836. DOI: `10.1038/35104522`.

[88] Dzmitry A. Yarotski et al. "Ultrafast Carrier-Relaxation Dynamics in Self-Assembled InAs/GaAs Quantum Dots". EN. In: *J. Opt. Soc. Am. B, JOSAB* 19.6 (June 2002), pp. 1480–1484. ISSN: 1520-8540. DOI: `10.1364/JOSAB.19.001480`.

[89] Matthew C. Beard, Gordon M. Turner, and Charles A. Schmuttenmaer. "Terahertz Spectroscopy". In: *J. Phys. Chem. B* 106.29 (July 2002), pp. 7146–7159. ISSN: 1520-6106. DOI: `10.1021/jp020579i`.

[90] Charles A. Schmuttenmaer. "Exploring Dynamics in the Far-Infrared with Terahertz Spectroscopy". In: *Chem. Rev.* 104.4 (Apr. 1, 2004), pp. 1759–1780. ISSN: 0009-2665, 1520-6890. DOI: `10.1021/cr020685g`.

[91] Takeshi Suzuki and Ryo Shimano. "Exciton Mott Transition in Si Revealed by Terahertz Spectroscopy". en. In: *Phys. Rev. Lett.* 109.4 (July 2012), p. 046402. ISSN: 0031-9007, 1079-7114. DOI: `10.1103/PhysRevLett.109.046402`.

[92] Jürgen Raab et al. "Ultrafast Terahertz Saturable Absorbers Using Tailored Intersubband Polaritons". In: *Nat Commun* 11.1 (1 Aug. 27, 2020), p. 4290. ISSN: 2041-1723. DOI: `10.1038/s41467-020-18004-8`.

[93] Xu Xie, Jianming Dai, and X.-C. Zhang. "Coherent Control of THz Wave Generation in Ambient Air". In: *Phys. Rev. Lett.* 96.7 (Feb. 2006), p. 075005. DOI: `10.1103/PhysRevLett.96.075005`.

[94] Yun-Shik Lee. "Generation and Detection of Broadband Terahertz Pulses". en. In: *Principles of Terahertz Science and Technology.* Springer, Boston, MA, 2009, pp. 1–66. ISBN: 978-0-387-09539-4 978-0-387-09540-0. DOI: `10.1007/978-0-387-09540-0_3`.

[95] J. D. Rowley et al. "Terahertz Generation by Optical Rectification in Uniaxial Birefringent Crystals". In: *Optics Express* 20.15 (July 2012). Comment: 6 pages, 3 figure,

online journal article, p. 16968. ISSN: 1094-4087. DOI: `10.1364/OE.20.016968`. arXiv: `1205.1044`.

[96] Yun-Shik Lee. *Principles of Terahertz Science and Technology.* en. Springer, Boston, MA, 2009. ISBN: 978-0-387-09539-4.

[97] Yoshitomo Okawachi et al. "Bandwidth Shaping of Microresonator-Based Frequency Combs via Dispersion Engineering". EN. In: *Opt. Lett., OL* 39.12 (June 2014), pp. 3535–3538. ISSN: 1539-4794. DOI: `10.1364/OL.39.003535`.

[98] Xiaoxia Yin, Brian Ng, and Derek Abbott. *Terahertz Imaging for Biomedical Applications: Pattern Recognition and Tomographic Reconstruction.* en. New York: Springer-Verlag, 2012. ISBN: 978-1-4614-1820-7.

[99] F. Blanchard et al. "Terahertz Pulse Generation from Bulk GaAs by a Tilted-Pulse-Front Excitation at 1.8 Mm". In: *Appl. Phys. Lett.* 105.24 (Dec. 2014), p. 241106. ISSN: 0003-6951. DOI: `10.1063/1.4904005`.

[100] Yun-Shik Lee et al. "Generation of Multicycle Terahertz Pulses via Optical Rectification in Periodically Inverted GaAs Structures". In: *Appl. Phys. Lett.* 89.18 (Oct. 2006), p. 181104. ISSN: 0003-6951. DOI: `10.1063/1.2367661`.

[101] K.l. Vodopyanov. "Optical THz-Wave Generation with Periodically-Inverted GaAs". en. In: *Laser & Photon. Rev.* 2.1-2 (Apr. 2008), pp. 11–25. ISSN: 1863-8899. DOI: `10.1002/lpor.200710028`.

[102] Matthias C. Hoffmann et al. "Efficient Terahertz Generation by Optical Rectification at 1035 Nm". en. In: *Optics Express* 15.18 (2007), p. 11706. ISSN: 1094-4087. DOI: `10.1364/OE.15.011706`.

[103] J.-P. Negel et al. "Compact and Cost-Effective Scheme for THz Generation via Optical Rectification in GaP and GaAs Using Novel Fs Laser Oscillators". en. In: *Appl.*

Phys. B 103.1 (Apr. 2011), pp. 45–50. ISSN: 1432-0649. DOI: `10.1007/s00340-011-4385-7`.

[104] Georgi L. Dakovski, Brian Kubera, and Jie Shan. "Localized Terahertz Generation via Optical Rectification in ZnTe". EN. In: *J. Opt. Soc. Am. B, JOSAB* 22.8 (Aug. 2005), pp. 1667–1670. ISSN: 1520-8540. DOI: `10.1364/JOSAB.22.001667`.

[105] S. Vidal et al. "Optimized Terahertz Generation via Optical Rectification in ZnTe Crystals". EN. In: *J. Opt. Soc. Am. B, JOSAB* 31.1 (Jan. 2014), pp. 149–153. ISSN: 1520-8540. DOI: `10.1364/JOSAB.31.000149`.

[106] F. Blanchard et al. "Generation of 1.5 μJ Single-Cycle Terahertz Pulses by Optical Rectification from a Large Aperture ZnTe Crystal". EN. In: *Opt. Express, OE* 15.20 (Oct. 2007), pp. 13212–13220. ISSN: 1094-4087. DOI: `10.1364/OE.15.013212`.

[107] Sen-Cheng Zhong et al. "Generation of 0.19-mJ THz Pulses in $\mathrm{LiNbO_3}$ Driven by 800-Nm Femtosecond Laser". en. In: (2016), p. 8.

[108] Sen-Cheng Zhong et al. "Optimization of Terahertz Generation from $\mathrm{LiNbO_3}$ under Intense Laser Excitation with the Effect of Three-Photon Absorption". en. In: (2015), p. 11.

[109] H. Hirori et al. "Single-Cycle Terahertz Pulses with Amplitudes Exceeding 1 MV/Cm Generated by Optical Rectification in LiNbO3". en. In: *Applied Physics Letters* 98.9 (Feb. 2011), p. 091106. ISSN: 0003-6951, 1077-3118. DOI: `10.1063/1.3560062`.

[110] S. A. Bereznaya et al. "Broadband and Narrowband Terahertz Generation and Detection in GaSe 1- x S x Crystals". en. In: *J. Opt.* 19.11 (2017), p. 115503. ISSN: 2040-8986. DOI: `10.1088/2040-8986/aa8e5a`.

[111] Joseph D. Rowley et al. "Terahertz Emission from ZnGeP_2: Phase-Matching, Intensity, and Length Scalability". en. In: *Journal of the Optical Society of America*

B 30.11 (Nov. 2013), p. 2882. ISSN: 0740-3224, 1520-8540. DOI: `10.1364/JOSAB.30.002882`.

[112] M. Bache, H. Guo, and B. Zhou. "Generating Mid-IR Octave-Spanning Supercontinua and Few-Cycle Pulses with Solitons in Phase-Mismatched Quadratic Nonlinear Crystals". In: *Optical Materials Express* 3.10 (Oct. 2013). Comment: submitted to Optics Materials Express special issue on mid-IR photonics, p. 1647. ISSN: 2159-3930. DOI: `10.1364/OME.3.001647`. arXiv: `1306.4097`.

[113] V. Petrov et al. "Femtosecond Parametric Generation in $ZnGeP_2$". EN. In: *Opt. Lett., OL* 24.6 (Mar. 1999), pp. 414–416. ISSN: 1539-4794. DOI: `10.1364/OL.24.000414`.

[114] Hamza Bennacer et al. "First Principles Investigation of Optoelectronic Properties of $ZnXP_2$ (X = Si, Ge) Lattice Matched with Silicon for Tandem Solar Cells Applications Using the mBJ Exchange Potential". In: *Optik* 159 (Apr. 2018), pp. 229–244. ISSN: 0030-4026. DOI: `10.1016/j.ijleo.2018.01.079`.

[115] A. S. Verma et al. "Investigation of Fundamental Physical Properties of $CdSiP_2$ and Its Application in Solar Cell Devices by Using (ZnX; X=Se, Te) Buffer Layers". In: *Materials Science and Engineering: B* 205 (Mar. 2016), pp. 18–27. ISSN: 0921-5107. DOI: `10.1016/j.mseb.2015.11.010`.

[116] Gennadiy A. Medvedkin and Valeriy G. Voevodin. "Magnetic and Optical Phenomena in Nonlinear Optical Crystals $ZnGeP_2$ and $CdGeP_2$". en. In: *Journal of the Optical Society of America B* 22.9 (Sept. 2005), p. 1884. ISSN: 0740-3224, 1520-8540. DOI: `10.1364/JOSAB.22.001884`.

[117] B. N. Carnio et al. "Generation of Broadband Terahertz Pulses via Optical Rectification in a Chalcopyrite $CdSiP_2$ Crystal". EN. In: *Opt. Lett., OL* 42.19 (Oct. 2017), pp. 3920–3923. ISSN: 1539-4794. DOI: `10.1364/OL.42.003920`.

[118] Kevin T. Zawilski et al. “Growth and Characterization of Large $CdSiP_2$ Single Crystals”. In: *Journal of Crystal Growth.* The 17th American Conference on Crystal Growth and Epitaxy/The 14th US Biennial Workshop on Organometallic Vapor Phase Epitaxy/The 6th International Workshop on Modeling in Crystal Growth 312.8 (Apr. 2010), pp. 1127–1132. ISSN: 0022-0248. DOI: `10.1016/j.jcrysgro.2009.10.034`.

[119] Kevin T. Zawilski et al. “Large Aperture Single Crystal $ZnGeP_2$ for High-Energy Applications”. In: *Journal of Crystal Growth.* The Proceedings of the 15th International Conference on Crystal Growth (ICCG-15) in Conjunction with the International Conference on Vapor Growth and Epitaxy and the US Biennial Workshop on Organometallic Vapor Phase Epitaxy 310.7 (Apr. 2008), pp. 1891–1896. ISSN: 0022-0248. DOI: `10.1016/j.jcrysgro.2007.11.151`.

[120] O. Chalus et al. “Optical Parametric Generation in $CdSiP_2$”. eng. In: *Opt Lett* 35.24 (Dec. 2010), pp. 4142–4144. ISSN: 1539-4794.

[121] Georgi Marchev et al. “Optical Parametric Generation in $CdSiP_2$ at 6.125 Mm Pumped by 8 Ns Long Pulses at 1064 Nm”. EN. In: *Opt. Lett., OL* 37.4 (Feb. 2012), pp. 740–742. ISSN: 1539-4794. DOI: `10.1364/OL.37.000740`.

[122] Peter G. Schunemann et al. “Advances in Nonlinear Optical Crystals for Mid-Infrared Coherent Sources”. en. In: *Journal of the Optical Society of America B* 33.11 (Nov. 2016), p. D36. ISSN: 0740-3224, 1520-8540. DOI: `10.1364/JOSAB.33.000D36`.

[123] B. N. Carnio et al. “Terahertz Birefringence and Absorption of a Chalcopyrite $CdSiP_2$ Crystal”. In: *Appl. Phys. Lett.* 111.22 (Nov. 2017), p. 221103. ISSN: 0003-6951. DOI: `10.1063/1.5006660`.

[124] D. T. F. Marple. “Refractive Index of ZnSe, ZnTe, and CdTe”. In: *Journal of Applied Physics* 35.3 (Mar. 1964), pp. 539–542. ISSN: 0021-8979. DOI: `10.1063/1.1713411`.

[125] D. Côté, J. E. Sipe, and H. M. van Driel. "Simple Method for Calculating the Propagation of Terahertz Radiation in Experimental Geometries". EN. In: *J. Opt. Soc. Am. B, JOSAB* 20.6 (June 2003), pp. 1374–1385. ISSN: 1520-8540. DOI: `10.1364/JOSAB.20.001374`.

[126] G C Bhar. "Refractive Index Dispersion of Chalcopyrite Crystals". en. In: *Journal of Physics D: Applied Physics* 13.3 (Mar. 1980), pp. 455–460. ISSN: 0022-3727, 1361-6463. DOI: `10.1088/0022-3727/13/3/018`.

[127] Marvin J. Weber. *Handbook of Optical Materials.* en. CRC Press, Sept. 2002. ISBN: 978-0-8493-3512-9.

[128] Edward D. Palik. *Handbook of Optical Constants of Solids.* en. Elsevier, Dec. 2012. ISBN: 978-0-08-054721-3.

[129] Brett N. Carnio et al. "Birefringence, Absorption, and Optical Rectification of a Chalcopyrite CdSiP2 Crystal in the Terahertz Frequency Regime". In: *Terahertz, RF, Millimeter, and Submillimeter-Wave Technology and Applications XI.* Ed. by Laurence P. Sadwick and Tianxin Yang. San Francisco, United States: SPIE, Feb. 2018, p. 63. ISBN: 978-1-5106-1547-2 978-1-5106-1548-9. DOI: `10.1117/12.2290739`.

[130] Vincent Kemlin et al. "Nonlinear, Dispersive, and Phase-Matching Properties of the New Chalcopyrite $\mathrm{CdSiP_2}$ [Invited]". EN. In: *Opt. Mater. Express, OME* 1.7 (Nov. 2011), pp. 1292–1300. ISSN: 2159-3930. DOI: `10.1364/OME.1.001292`.

[131] B. S. Wherrett. "Scaling Rules for Multiphoton Interband Absorption in Semiconductors". EN. In: *J. Opt. Soc. Am. B, JOSAB* 1.1 (Mar. 1984), pp. 67–72. ISSN: 1520-8540. DOI: `10.1364/JOSAB.1.000067`.

[132] G. Boyd et al. “Linear and Nonlinear Optical Properties of Ternary $A^{II}B^{IV}C_2{}^V$ Chalcopyrite Semiconductors”. In: *IEEE Journal of Quantum Electronics* 8.4 (Apr. 1972), pp. 419–426. ISSN: 0018-9197. DOI: `10.1109/JQE.1972.1076982`.

[133] Valentin Petrov et al. “The Nonlinear Coefficient D_{36} of $CdSiP_2$”. In: *Nonlinear Frequency Generation and Conversion: Materials, Devices, and Applications VIII.* Vol. 7197. International Society for Optics and Photonics, Feb. 2009, p. 71970M. DOI: `10.1117/12.809586`.

[134] Kevin T. Zawilski et al. “Increasing the Laser-Induced Damage Threshold of Single-Crystal $ZnGeP_2$”. In: *J. Opt. Soc. Am. B, JOSAB* 23.11 (Nov. 1, 2006), pp. 2310–2316. ISSN: 1520-8540. DOI: `10.1364/JOSAB.23.002310`.

[135] Anne Hildenbrand-Dhollande et al. “Laser-Induced Damage Study at 1.064 and 2.09 μm of High Optical Quality $CdSiP_2$ Crystal”. In: *Advanced Solid State Lasers (2015), Paper AM2A.8.* Advanced Solid State Lasers. Optica Publishing Group, Oct. 4, 2015, AM2A.8. DOI: `10.1364/ASSL.2015.AM2A.8`.

[136] Ronald Ulbricht et al. “Carrier Dynamics in Semiconductors Studied with Time-Resolved Terahertz Spectroscopy”. In: *Rev. Mod. Phys.* 83.2 (June 2011), pp. 543–586. DOI: `10.1103/RevModPhys.83.543`.

[137] I-Chen Ho and Xi-Cheng Zhang. “Application of Broadband Terahertz Spectroscopy in Semiconductor Nonlinear Dynamics”. en. In: *Front. Optoelectron.* 7.2 (June 2014), pp. 220–242. ISSN: 2095-2759, 2095-2767. DOI: `10.1007/s12200-014-0398-2`.

[138] James Lloyd-Hughes and Tae-In Jeon. “A Review of the Terahertz Conductivity of Bulk and Nano-Materials”. en. In: *J Infrared Milli Terahz Waves* 33.9 (Sept. 2012), pp. 871–925. ISSN: 1866-6906. DOI: `10.1007/s10762-012-9905-y`.

[139] Timothy J. Magnanelli and Edwin J. Heilweil. "Carrier Mobility of Silicon by Sub-Bandgap Time-Resolved Terahertz Spectroscopy". en. In: *Opt. Express* 28.5 (Mar. 2020), p. 7221. ISSN: 1094-4087. DOI: `10.1364/OE.382840`.

[140] Xiao Xing et al. "Role of Photoinduced Exciton in the Transient Terahertz Conductivity of Few-Layer WS $_2$ Laminate". en. In: *J. Phys. Chem. C* 121.37 (Sept. 2017), pp. 20451–20457. ISSN: 1932-7447, 1932-7455. DOI: `10.1021/acs.jpcc.7b05345`.

[141] Matthew C. Beard, Gordon M. Turner, and Charles A. Schmuttenmaer. "Transient Photoconductivity in GaAs as Measured by Time-Resolved Terahertz Spectroscopy". In: *Physical Review B* 62 (), pp. 15764–15777.

[142] Herath P. Piyathilaka et al. "Hot-Carrier Dynamics in InAs/AlAsSb Multiple-Quantum Wells". In: *Scientific Reports* 11.1 (May 2021), p. 10483. ISSN: 2045-2322. DOI: `10.1038/s41598-021-89815-y`.

[143] Herath P. Piyathilaka et al. "Hot-Carrier Dynamics of Type-II InAs/AlAs1-xSbx Quantum Wells". en. In: *Frontiers in Optics / Laser Science*. Washington, DC: OSA, 2020, FW4B.3. ISBN: 978-1-943580-80-4. DOI: `10.1364/FIO.2020.FW4B.3`.

[144] Rishmali Sooriyagoda et al. "Ultrafast Carrier Dynamics and Photoconductivity of the Chalcopyrite Crystals". en. In: *Frontiers in Optics / Laser Science*. Washington, DC: OSA, 2020, JW6B.11. ISBN: 978-1-943580-80-4. DOI: `10.1364/FIO.2020.JW6B.11`.

[145] Patrick Parkinson et al. "Transient Terahertz Conductivity of GaAs Nanowires". en. In: *Nano Letters* 7.7 (July 2007), pp. 2162–2165. ISSN: 1530-6984, 1530-6992. DOI: `10.1021/nl071162x`.

[146] A. F. Oliveira et al. "Main Scattering Mechanisms in InAs/GaAs Multi-Quantum-Well: A New Approach by the Global Optimization Method". en. In: *J Mater Sci* 51.3 (Feb. 2016), pp. 1333–1343. ISSN: 1573-4803. DOI: `10.1007/s10853-015-9451-9`.

[147] Yanbo Li, Yang Zhang, and Yiping Zeng. "Electron Mobility in Modulation-Doped AlSb/InAs Quantum Wells". In: *Journal of Applied Physics* 109.7 (Apr. 2011), p. 073703. ISSN: 0021-8979. DOI: `10.1063/1.3552417`.

[148] Herbert Kroemer. "The Family (InAs, GaSb, AlSb) and Its Heterostructures: A Selective Review". In: *Physica E: Low-dimensional Systems and Nanostructures* 20.3-4 (Jan. 2004), pp. 196–203. ISSN: 13869477. DOI: `10.1016/j.physe.2003.08.003`.

[149] I. Vurgaftman, J. R. Meyer, and L. R. Ram-Mohan. "Band Parameters for III–V Compound Semiconductors and Their Alloys". In: *Journal of Applied Physics* 89.11 (June 2001), pp. 5815–5875. ISSN: 0021-8979. DOI: `10.1063/1.1368156`.

[150] J. Tang et al. "Effects of Localization on Hot Carriers in InAs/AlAsxSb1–x Quantum Wells". In: *Appl. Phys. Lett.* 106.6 (Feb. 2015), p. 061902. ISSN: 0003-6951. DOI: `10.1063/1.4907630`.

[151] V. R. Whiteside et al. "Valence Band States in an InAs/AlAsSb Multi-Quantum Well Hot Carrier Absorber". In: *Semicond. Sci. Technol.* 34.2 (2019), p. 025005. ISSN: 0268-1242. DOI: `10.1088/1361-6641/aae4c3`.

[152] Matthew P. Lumb et al. "Quantum Wells and Superlattices for III-V Photovoltaics and Photodetectors". In: *Next Generation (Nano) Photonic and Cell Technologies for Solar Energy Conversion III*. Vol. 8471. International Society for Optics and Photonics, Oct. 2012, 84710A. DOI: `10.1117/12.964654`.

[153] V R Whiteside et al. "The Role of Intervalley Phonons in Hot Carrier Transfer and Extraction in Type-II InAs/AlAsSb Quantum-Well Solar Cells". In: *Semicond. Sci.*

Technol. 34.9 (Sept. 2019), p. 094001. ISSN: 0268-1242, 1361-6641. DOI: `10.1088/1361-6641/ab312b`.

[154] Hannah J Joyce et al. "A Review of the Electrical Properties of Semiconductor Nanowires: Insights Gained from Terahertz Conductivity Spectroscopy". en. In: *Semiconductor Science and Technology* 31.10 (Oct. 2016), p. 103003. ISSN: 0268-1242, 1361-6641. DOI: `10.1088/0268-1242/31/10/103003`.

[155] Marius Grundmann. *The Physics of Semiconductors.* 1st. Springer. ISBN: 3-540-25370-X.

[156] J. Lloyd-Hughes. "Generalized Conductivity Model for Polar Semiconductors at Terahertz Frequencies". en. In: *Appl. Phys. Lett.* 100.12 (Mar. 2012), p. 122103. ISSN: 0003-6951, 1077-3118. DOI: `10.1063/1.3695161`.

[157] N. Smith. "Classical Generalization of the Drude Formula for the Optical Conductivity". en. In: *Phys. Rev. B* 64.15 (Sept. 2001), p. 155106. ISSN: 0163-1829, 1095-3795. DOI: `10.1103/PhysRevB.64.155106`.

[158] T. L. Cocker et al. "Microscopic Origin of the Drude-Smith Model". en. In: *Physical Review B* 96.20 (Nov. 2017). Comment: 18 pages, 8 figures, accepted to PRB, various changes and clarifications. ISSN: 2469-9950, 2469-9969. DOI: `10.1103/PhysRevB.96.205439`. arXiv: `1705.10350`.

[159] David R. Rhiger and Edward P. Smith. "Infrared Absorption near the Bandgap in the InAs/InAsSb Superlattice". In: *Infrared Sensors, Devices, and Applications X.* Vol. 11503. International Society for Optics and Photonics, Sept. 2020, p. 1150305. DOI: `10.1117/12.2569820`.

[160] Shin-ichiro Gozu et al. "Interface States of AlSb/InAs Heterointerface with AlAs-Like Interface". In: *Jpn. J. Appl. Phys.* 45.4S (Apr. 2006), p. 3544. ISSN: 1347-4065. DOI: `10.1143/JJAP.45.3544`.

[161] Jun Shen et al. "Tamm States and Donors at InAs/AlSb Interfaces". In: *Journal of Applied Physics* 77.4 (Feb. 1995), pp. 1576–1581. ISSN: 0021-8979. DOI: `10.1063/1.358910`.

[162] Rishmali Sooriyagoda et al. "Carrier Transport and Electron–Lattice Interactions of Nonlinear Optical Crystals CdGeP $_2$, ZnGeP $_2$, and CdSiP $_2$". In: *J. Opt. Soc. Am. B* 38.3 (Mar. 2021), p. 769. ISSN: 0740-3224, 1520-8540. DOI: `10.1364/JOSAB.410454`.

[163] Sadao Adachi. "III-V Ternary and Quaternary Compounds". en. In: *Springer Handbook of Electronic and Photonic Materials*. Ed. by Safa Kasap and Peter Capper. Cham: Springer International Publishing, 2017, pp. 1–1. ISBN: 978-3-319-48931-5 978-3-319-48933-9. DOI: `10.1007/978-3-319-48933-9_30`.

[164] Yan-Feng Lao et al. "Tunable Hot-Carrier Photodetection beyond the Bandgap Spectral Limit". In: *Nature Photon* 8.5 (5 May 2014), pp. 412–418. ISSN: 1749-4893. DOI: `10.1038/nphoton.2014.80`.

[165] Larousse Khosravi Khorashad et al. "Localization of Excess Temperature Using Plasmonic Hot Spots in Metal Nanostructures: Combining Nano-Optical Antennas with the Fano Effect". In: *J. Phys. Chem. C* 120.24 (June 23, 2016), pp. 13215–13226. ISSN: 1932-7447. DOI: `10.1021/acs.jpcc.6b03644`.

[166] Gavin Conibeer et al. "Modelling of Hot Carrier Solar Cell Absorbers". In: *Solar Energy Materials and Solar Cells*. PVSEC 18 94.9 (Sept. 1, 2010), pp. 1516–1521. ISSN: 0927-0248. DOI: `10.1016/j.solmat.2010.01.018`.

[167] Jivtesh Garg and Ian R. Sellers. “Phonon Linewidths in InAs/AlSb Superlattices Derived from First-Principles—Application towards Quantum Well Hot Carrier Solar Cells”. In: *Semicond. Sci. Technol.* 35.4 (Mar. 2020), p. 044001. ISSN: 0268-1242. DOI: `10.1088/1361-6641/ab73f0`.

[168] L. C. Hirst et al. “Hot Carriers in Quantum Wells for Photovoltaic Efficiency Enhancement”. In: *IEEE Journal of Photovoltaics* 4.1 (Jan. 2014), pp. 244–252. ISSN: 2156-3381. DOI: `10.1109/JPHOTOV.2013.2289321`.

[169] P. G. Klemens. “Anharmonic Decay of Optical Phonons”. In: *Phys. Rev.* 148.2 (Aug. 1966), pp. 845–848. DOI: `10.1103/PhysRev.148.845`.

[170] B K Ridley. “The LO Phonon Lifetime in GaN”. In: *J. Phys.: Condens. Matter* 8.37 (Sept. 1996), pp. L511–L513. ISSN: 0953-8984, 1361-648X. DOI: `10.1088/0953-8984/8/37/001`.

[171] Yao Yao and Dirk König. “Comparison of Bulk Material Candidates for Hot Carrier Absorber”. In: *Solar Energy Materials and Solar Cells* 140 (Sept. 2015), pp. 422–427. ISSN: 09270248. DOI: `10.1016/j.solmat.2015.05.002`.

[172] P. Aliberti et al. “Investigation of Theoretical Efficiency Limit of Hot Carriers Solar Cells with a Bulk Indium Nitride Absorber”. In: *Journal of Applied Physics* 108.9 (Nov. 1, 2010), p. 094507. ISSN: 0021-8979. DOI: `10.1063/1.3494047`.

[173] Yao Yao, Dirk König, and Martin Green. “Investigation of Boron Antimonide as Hot Carrier Absorber Material”. In: *Solar Energy Materials and Solar Cells* 111 (Apr. 1, 2013), pp. 123–126. ISSN: 0927-0248. DOI: `10.1016/j.solmat.2012.12.029`.

[174] null Rosenwaks et al. “Hot-Carrier Cooling in GaAs: Quantum Wells versus Bulk”. In: *Phys Rev B Condens Matter* 48.19 (Nov. 15, 1993), pp. 14675–14678. ISSN: 0163-1829. DOI: `10.1103/physrevb.48.14675`. pmid: `10007896`.

[175] L. Lindsay, D. A. Broido, and T. L. Reinecke. "*Ab Initio* Thermal Transport in Compound Semiconductors". en. In: *Phys. Rev. B* 87.16 (Apr. 2013), p. 165201. ISSN: 1098-0121, 1550-235X. DOI: `10.1103/PhysRevB.87.165201`.

[176] L. Esaki and R. Tsu. "Superlattice and Negative Differential Conductivity in Semiconductors". In: *IBM Journal of Research and Development* 14.1 (Jan. 1970), pp. 61–65. ISSN: 0018-8646. DOI: `10.1147/rd.141.0061`.

[177] K.-H. Lee et al. "Investigation of Carrier Recombination Dynamics of InGaP/InGaAsP Multiple Quantum Wells for Solar Cells via Photoluminescence". In: *arXiv:1611.01923 [cond-mat]* (Jan. 2017). Comment: 6 pages, 5 figures, 2 tables. arXiv: `1611.01923 [cond-mat]`.

[178] W. Z. Shen and S. C. Shen. "Exciton-Longitudinal-Optical Phonon Coupling in Quantum Wells". In: *Infrared Physics & Technology* 37.6 (Oct. 1996), pp. 655–657. ISSN: 1350-4495. DOI: `10.1016/S1350-4495(96)00014-X`.

[179] Yi Zhang et al. "Explore the Intervalley Scattering on Phonon Bottleneck Effect and Its Application on Hot Carrier Solar Cells". In: *2020 12th IEEE PES Asia-Pacific Power and Energy Engineering Conference (APPEEC)*. Sept. 2020, pp. 1–4. DOI: `10.1109/APPEEC48164.2020.9220617`.

[180] P. T. Landsberg. "Trap-Auger Recombination in Silicon of Low Carrier Densities". In: *Appl. Phys. Lett.* 50.12 (Mar. 23, 1987), pp. 745–747. ISSN: 0003-6951. DOI: `10.1063/1.98086`.

[181] Jan Linnros. "Carrier Lifetime Measurements Using Free Carrier Absorption Transients. I. Principle and Injection Dependence". In: *Journal of Applied Physics* 84.1 (June 1998), pp. 275–283. ISSN: 0021-8979. DOI: `10.1063/1.368024`.

[182] Brian L. Wilmer et al. “Role of Strain on the Coherent Properties of GaAs Excitons and Biexcitons”. In: *Phys. Rev. B* 94.7 (Aug. 2016), p. 075207. ISSN: 2469-9950, 2469-9969. DOI: `10.1103/PhysRevB.94.075207`.

[183] A David and B Miller. “Optical Physics of Quantum Wells”. In: *Quantum Dynamics of Simple Systems*. Ed. by G-L Oppo et al. First. CRC Press, Dec. 2020, pp. 239–266. ISBN: 978-1-00-307297-3. DOI: `10.1201/9781003072973-9`.

[184] Bhavtosh Bansal et al. “Alloying Induced Degradation of the Absorption Edge of InAsxSb1-x”. In: *Appl. Phys. Lett.* 90.10 (Mar. 2007), p. 101905. ISSN: 0003-6951. DOI: `10.1063/1.2711388`.

[185] Alan D. Bristow, Nir Rotenberg, and Henry M. van Driel. “Two-Photon Absorption and Kerr Coefficients of Silicon for 850–2200nm”. In: *Applied Physics Letters* 90.19 (May 2007), p. 191104. ISSN: 0003-6951, 1077-3118. DOI: `10.1063/1.2737359`.

[186] Franz Urbach. “The Long-Wavelength Edge of Photographic Sensitivity and of the Electronic Absorption of Solids”. In: *Phys. Rev.* 92.5 (Dec. 1953), pp. 1324–1324. DOI: `10.1103/PhysRev.92.1324`.

[187] Wasim Raja Mondal et al. “Localization of Phonons in Mass Disordered Alloys - A Typical Medium Dynamical Cluster Approach”. In: *Phys. Rev. B* 96.1 (July 2017). Comment: 14 pages, 10 figures, p. 014203. ISSN: 2469-9950, 2469-9969. DOI: `10.1103/PhysRevB.96.014203`. arXiv: `1806.00282`.

[188] Hamid Reza Seyf et al. “Rethinking Phonons: The Issue of Disorder”. In: *npj Computational Materials* 3.1 (Nov. 2017), pp. 1–8. ISSN: 2057-3960. DOI: `10.1038/s41524-017-0052-9`.

[189] G. D. Cody et al. “Disorder and the Optical-Absorption Edge of Hydrogenated Amorphous Silicon”. In: *Phys. Rev. Lett.* 47.20 (Nov. 1981), pp. 1480–1483. ISSN: 0031-9007. DOI: `10.1103/PhysRevLett.47.1480`.

[190] Tess R. Senty et al. “Inverting Transient Absorption Data to Determine Transfer Rates in Quantum Dot–TiO $_2$ Heterostructures”. In: *J. Phys. Chem. C* 119.11 (Mar. 2015), pp. 6337–6343. ISSN: 1932-7447, 1932-7455. DOI: `10.1021/jp512500g`.

[191] Masumi Takeshima. “Auger Recombination in InAs, GaSb, InP, and GaAs”. In: *Journal of Applied Physics* 43.10 (Oct. 1972), pp. 4114–4119. ISSN: 0021-8979, 1089-7550. DOI: `10.1063/1.1660882`.

[192] W. K. Metzger et al. “Auger Recombination in Low-Band-Gap n -Type InGaAs”. In: *Appl. Phys. Lett.* 79.20 (Nov. 2001), pp. 3272–3274. ISSN: 0003-6951, 1077-3118. DOI: `10.1063/1.1418032`.

[193] I.P. Marko et al. “The Role of Auger Recombination in Inas 1.3-Mm Quantum-Dot Lasers Investigated Using High Hydrostatic Pressure”. In: *IEEE J. Select. Topics Quantum Electron.* 9.5 (Sept. 2003), pp. 1300–1307. ISSN: 1077-260X. DOI: `10.1109/JSTQE.2003.819504`.

[194] Michael A. Cavicchia, Wubao Wang, and R. R. Alfano. “Intervalley Scattering as a Function of Temperature in Gaas Using Time-Resolved Visible Pump - IR Probe Absorption Spectroscopy”. In: *Hot Carriers in Semiconductors.* Ed. by Karl Hess, Jean-Pierre Leburton, and Umberto Ravaioli. Boston, MA: Springer US, 1996, pp. 365–368. ISBN: 978-1-4613-8035-1 978-1-4613-0401-2. DOI: `10.1007/978-1-4613-0401-2_83`.

[195] Herbert Kroemer. “The 6.1Å Family (InAs, GaSb, AlSb) and Its Heterostructures: A Selective Review”. In: *Physica E: Low-dimensional Systems and Nanostructures.* Proceedings of the 11th International Conference on Narrow Gap Semiconductors

20.3 (Jan. 2004), pp. 196–203. ISSN: 1386-9477. DOI: `10.1016/j.physe.2003.08.003`.

[196] Jaroslaw Dabrowski and Matthias Scheffler. “Isolated Arsenic-Antisite Defect in GaAs and the Properties of *EL* 2”. In: *Phys. Rev. B* 40.15 (Nov. 1989), pp. 10391–10401. ISSN: 0163-1829. DOI: `10.1103/PhysRevB.40.10391`.

[197] Jun Shen et al. “Remote n -type Modulation Doping of InAs Quantum Wells by “Deep Acceptors” in AlSb”. In: *Journal of Applied Physics* 73.12 (June 1993), pp. 8313–8318. ISSN: 0021-8979, 1089-7550. DOI: `10.1063/1.353450`.

[198] Valentina Cesari, Wolfgang Langbein, and Paola Borri. “The Role of P-Doping in the Gain Dynamics of InAs/GaAs Quantum Dots at Low Temperature”. In: *Appl. Phys. Lett.* 94.4 (Jan. 2009), p. 041110. ISSN: 0003-6951, 1077-3118. DOI: `10.1063/1.3075855`.

[199] Jiangtian Li et al. “Solar Hydrogen Generation by a CdS-Au-TiO2 Sandwich Nanorod Array Enhanced with Au Nanoparticle as Electron Relay and Plasmonic Photosensitizer”. In: *J. Am. Chem. Soc.* 136.23 (June 11, 2014), pp. 8438–8449. ISSN: 0002-7863. DOI: `10.1021/ja503508g`.

[200] Yitao Dai et al. “Boosting Photocatalytic Hydrogen Production by Modulating Recombination Modes and Proton Adsorption Energy”. In: *J. Phys. Chem. Lett.* 10.18 (Sept. 19, 2019), pp. 5381–5386. DOI: `10.1021/acs.jpclett.9b01460`.

[201] Han-Kwang Nienhuys and Villy Sundström. “Influence of Plasmons on Terahertz Conductivity Measurements”. In: *Appl. Phys. Lett.* 87.1 (June 2005), p. 012101. ISSN: 0003-6951. DOI: `10.1063/1.1977213`.

[202] Jeppe C. Dyre. “Universal Low-Temperature Ac Conductivity of Macroscopically Disordered Nonmetals”. en. In: *Phys. Rev. B* 48.17 (Nov. 1993), pp. 12511–12526. ISSN: 0163-1829, 1095-3795. DOI: `10.1103/PhysRevB.48.12511`.

[203] H P Piyathilaka et al. “Non-Equilibrium Hot-Carrier Transport in Type-II Multiple-Quantum Wells for Solar-Cell Applications”. In: (), p. 7.

[204] D.M. Caughey and R.E. Thomas. “Carrier Mobilities in Silicon Empirically Related to Doping and Field”. In: *Proceedings of the IEEE* 55.12 (Dec. 1967), pp. 2192–2193. ISSN: 1558-2256. DOI: `10.1109/PROC.1967.6123`.

[205] V. G. Mokerov et al. “Drift Velocity of Electrons in Quantum Wells in High Electric Fields”. In: *Semiconductors* 43.4 (Apr. 2009), pp. 458–462. ISSN: 1063-7826, 1090-6479. DOI: `10.1134/S1063782609040095`.

[206] A. Guen-Bouazza et al. “Steady-State and Transient Electron Transport within Bulk InAs, InP and GaAs: An Updated Semiclassical Three-Valley Monte Carlo Simulation Analysis”. In: *JMP* 04.05 (2013), pp. 616–621. ISSN: 2153-1196, 2153-120X. DOI: `10.4236/jmp.2013.45089`.

[207] J. S. Blakemore. “Semiconducting and Other Major Properties of Gallium Arsenide”. In: *Journal of Applied Physics* 53.10 (Oct. 1982), R123–R181. ISSN: 0021-8979, 1089-7550. DOI: `10.1063/1.331665`.

[208] A. Šilenas et al. “Maximum Drift Velocity of Electrons in Selectively Doped InAlAs/InGaAs/InAlAs Heterostructures with InAs Inserts”. In: *Semiconductors* 47.3 (Mar. 2013), pp. 372–375. ISSN: 1063-7826. DOI: `10.1134/S1063782613030263`.

[209] Shudong Wu, Liwen Cheng, and Qiang Wang. “Excitonic Effects and Related Properties in Semiconductor Nanostructures: Roles of Size and Dimensionality”. In: *Mater.*

Res. Express 4.8 (Aug. 10, 2017), p. 085017. ISSN: 2053-1591. DOI: `10.1088/2053-1591/aa81da`.

[210] Bin Jiang et al. "Effects of Reduced Exciton Diffusion in InGaN/GaN Multiple Quantum Well Nanorods". In: *Opt. Express* 20.12 (June 4, 2012), p. 13478. ISSN: 1094-4087. DOI: `10.1364/OE.20.013478`.

[211] Andreas Hangleiter et al. "Efficient Formation of Excitons in a Dense Electron-Hole Plasma at Room Temperature". en. In: *Phys. Rev. B* 92.24 (Dec. 2015), p. 241305. ISSN: 1098-0121, 1550-235X. DOI: `10.1103/PhysRevB.92.241305`.

[212] B. Gerlach et al. "Exciton Binding Energy in a Quantum Well". In: *Phys. Rev. B* 58.16 (Oct. 15, 1998), pp. 10568–10577. ISSN: 0163-1829, 1095-3795. DOI: `10.1103/PhysRevB.58.10568`.

[213] N. F. Mott. "Metal-Insulator Transition". In: *Rev. Mod. Phys.* 40.4 (Oct. 1, 1968), pp. 677–683. ISSN: 0034-6861. DOI: `10.1103/RevModPhys.40.677`.

[214] Hannes Hempel et al. "Minority and Majority Charge Carrier Mobility in Cu2ZnSnSe4 Revealed by Terahertz Spectroscopy". en. In: *Scientific Reports* 8.1 (Dec. 2018). ISSN: 2045-2322. DOI: `10.1038/s41598-018-32695-6`.

[215] A. Fiore et al. "Carrier Diffusion in Low-Dimensional Semiconductors: A Comparison of Quantum Wells, Disordered Quantum Wells, and Quantum Dots". In: *Phys. Rev. B* 70.20 (Nov. 9, 2004), p. 205311. ISSN: 1098-0121, 1550-235X. DOI: `10.1103/PhysRevB.70.205311`.

[216] Cheng-Hao Chu et al. "A New Fitting Method for Ambipolar Diffusion Length Extraction in Thin Film Structures Using Photoluminescence Measurement with Scanning Excitation". In: *Sci Rep* 10 (Mar. 23, 2020), p. 5200. ISSN: 2045-2322. DOI: `10.1038/s41598-020-62093-w`. pmid: `32251350`.

[217] Kikuo Makita et al. “III-V//Si multijunction solar cells with 30% efficiency using smart stack technology with Pd nanoparticle array”. In: *Progress in Photovoltaics: Research and Applications* 28.1 (2020), pp. 16–24. ISSN: 1099-159X. DOI: `10.1002/pip.3200`.

[218] J. Li et al. “A Brief Review of High Efficiency III-V Solar Cells for Space Application”. In: *Frontiers in Physics* 8 (2021). ISSN: 2296-424X.

[219] Armantas Melianas et al. “Photogenerated Carrier Mobility Significantly Exceeds Injected Carrier Mobility in Organic Solar Cells”. In: *Advanced Energy Materials* 7.9 (2017), p. 1602143. ISSN: 1614-6840. DOI: `10.1002/aenm.201602143`.

[220] Jiaying Wu et al. “A Comparison of Charge Carrier Dynamics in Organic and Perovskite Solar Cells”. In: *Advanced Materials* 34.2 (2022), p. 2101833. ISSN: 1521-4095. DOI: `10.1002/adma.202101833`.